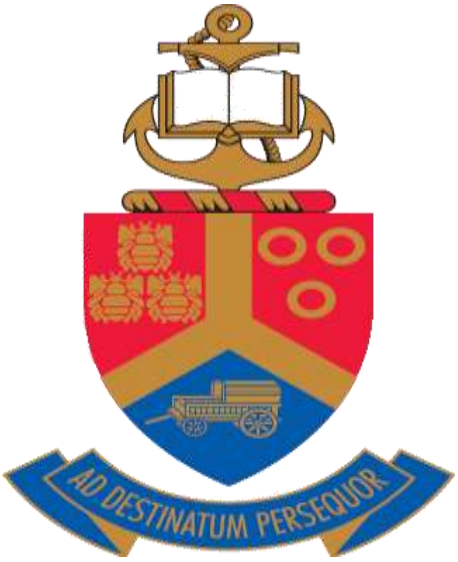

Development and Characterization of 9%Cr Shielded Metal Arc Welding Electrodes

Kawulani Patrick Ngwenya

Student number: 13379110

Supervisor: Prof. PGH Pistorius

Submitted in partial fullfilment of the requirements for the degree

Master of Science Metallurgy

In the Faculty of Engineering, the Built Environment and Information Technology

University of Pretoria, Pretoria

ABSTRACT

The objective of the current study was to develop SMAW electrodes to American Welding Society (AWS SFA 5.5 E9018-B9) with an A_{c1} temperature above the post weld heat treatment (PWHT) temperature (760ºC). The weld metal microstructure should be tempered martensite with hardness close to that of the P91 base metal after PWHT. About 30 different electrodes were formulated, with 15 of the formulated laboratory electrodes and three commercial electrodes along with the base metal characterised by depositing bead-on-plate welds. The A_{C1} temperatures of the welds were measured on the Bähr 805D dilatometer. Two previous published empirical equations for the A_{C1} temperature were used to verify the results. The measured A_{C1} temperatures of the laboratory developed and commercial electrodes weld metals were found to be above the PWHT temperature. A predictive equation for the A_1 temperature equation was developed in this study. The microstructure was predominant martensite in as-welded and after PWHT. However, delta (δ) and alpha (α) ferrite was observed in the microstructure of some weld metals in both these conditions. Zhang et al. and Merchant ferrite factor prediction in some of the weld metal microstructures were found to be contradictory to the findings in the present study. The Vickers hardnesses of the weld metals after PWHT were below 265HV with soft spot (hardnesses below 200 HV) shown in some of the weld metals.

TABLE OF CONTENTS

LIST OF TABLES

LIST OF FIGURES

LIST OF ABBREVIATIONS

SMAW	Shielded metal arc welding
A_{c1}	Lower critical austenite transformation temperature
A_{c3}	Upper critical austenite complete temperature
A_{c2}	Temperature at which material state change from ferromagnetic to paramagnetic
M_s	Martensite start temperature
M_f	Martensite complete temperature
Wt%	Weight percent
AW	As-welded
RT	Room temperature
PWHT	Post weld heat treatment temperature
ASTM	American Society for Testing Materials
ASME	American Society for Mechanical Engineers
SEM	Scanning electron microscope
α-ferrite	Alpha ferrite
δ-ferrite	Delta ferrite
γ	Austenite
α'	Martensite
M and X (for precipitates)	Metallic element and carbon and/or nitrogen, respectively
HV	Vickers hardness
BOP	Bead-on- plate
Cr_{eq}	Chromium equivalent
Ni_{eq}	Nickel equivalent
FF	Ferrite factor
C	Carbon
Si	Silicon
Mn	Manganese
Cr	Chromium
Mo	Molybdenum
V	Vanadium
N	Nitrogen
Cu	Copper

Nb	Niobium
S	Sulphur
P	Phosphorus

ACKNOWLEDGEMENTS

I would like to take this opportunity to express my gratitude to my supervisor, Professor Pieter Pistorius for his expertise, continued support and valuable advice during my MSc study. I wish to thank the technical team at Afrox Welding Consumable Factory (WCF); Paul Magano, Thomas Khumalo and Chris Muleya for the contribution during the electrode's development process. To the Industrial Metals and Minerals Research Institute (IMMRI) at the University of Pretoria, thank you for your assistance with your facilities during my study. I would also like to thank Mintek, especially Joseph Moema for the valuable support on my project.

I would also like to express my special thanks to my family, my wife Martha Ngwenya and my three children (Nyiko, Nhlamulo and Lethabo) for their love and support during my study. To my late parents Zephania Ngwenya and Martha Ngwenya, thank you for encouraging me, to see the value of education. Lastly and most importantly, I would like to thank GOD for giving me the strength and wisdom throughout my study.

CHAPTER 1: BACKGROUND AND OUTLINE OF STUDY

1.1 BACKGROUND

Creep resistant steels have been developed since 1912 to improve the efficiency of power generation and petrochemical plants. The major challenge facing power generation and petrochemical industries is to increase efficiencies brought by stringent environmental regulations, whilst ensuring that reliability, availability, and maintainability are not compromised. Increasing the thermal efficiencies of the generating plants results in fuel conservation (less fuel for a given output) and a reduction in emissions (lower fuel consumption means lower emissions of environmentally damaging gases such as CO_2) [1].

P91 are 9%Cr steels with alloying elements such as V, Nb, Ni, Mo, N to enhance high temperature mechanical strength, weldability and oxidation resistance. P91 steels are used in the fossil power plants operating in the temperature range between 500-600ºC. The P91 creep resistant steels are high strength alloys that normally transform completely to martensite during air cooling [2]. The P91 alloy steel has high thermal conductivity, resistance to stress corrosion cracking, a low thermal expansion coefficient and high resistance to thermal fatigue. The microstructure of these steels in the normalized and tempered (N&T) condition consists of tempered lath martensite with precipitates on martensite lath boundaries [3]. Typical applications for these industries are boilers, heat exchangers, heaters, reactors, hydrocrackers, and heavy wall pressure vessels. The shift to higher operating temperatures requires the use of material with appropriate high temperature strength, creep properties, physical properties, and metallurgical stability at the operating temperature of the plant to prevent catastrophic failures by several long-term mechanisms, including leakage due to creep-induced dimensional changes, bursting due to stress rupture or thermal fatigue due to thermal-induced cyclic stresses.

Development of the P91 welding consumables must follow that of the base metals with the assurance of meeting similar stringent requirements as for the base materials. As a result, in P91 and P92 welding consumables with additions of vanadium (V), tungsten (W), titanium (Ti), niobium (Nb), boron (B) and/or nitrogen have been

developed and are still under development [4]. Depending upon the concentration levels of various elements, especially nickel (Ni) and manganese (Mn), the critical temperature (where austenite begins to re-form) can fall to below 815ºC [5]. High concentration levels of ferrite formers, notable chromium, may increase the formation of delta ferrite. If adequate temperature controls are not utilized during the tempering heat treatment, austenite and, at high temperatures, delta ferrite may form. Upon cooling, the fresh austenite will transform into untempered martensite. The presence of either delta ferrite or untempered martensite will be detrimental to the toughness and high temperature properties of the material.

.

1.2 MOTIVATION OF THE RESEARCH

The power generation and petrochemical industries in South Africa are currently replacing the low chromium-molybdenum creep resistant steels (such as 1Cr 0.5 Mo and 2.25 Cr-1 Mo) with high chromium P91 creep resistant steels. The P91 welding consumable is currently not manufactured in South Africa. The development of this high chromium creep resistant welding consumable in South African will increase the market share of local welding consumable manufacturers.

1.3 RESEARCH OBJECTIVES

The objective was to develop a SMAW welding consumable meeting the ASME SFA 5.5 E9018-B9 specification with the lower critical temperature (A_{c1}) higher than the post weld heat treatment (PWHT) temperature after welding. The effect of alloying elements such as nickel, manganese, and carbon to the A_{c1} temperature was also investigated. The specific objectives of this dissertation are outlined below:

- Development of a standard P91 welding consumable meeting ASME SFA 5.5 E9018-B9 in terms of flux formulation and weld metal chemical composition.
- Determining the lower critical temperature (A_{c1}) of the weld metal using dilatometry.
- Simulation of the post weld heat treatment (PWHT) at the temperature defined in AWS SFA 5.5 9018-B9 using dilatometry and heat treatment in a batch furnace.
- Evaluation of the microstructures of the base material and weld metal in the as-welded condition and after post-weld heat treatment using optical and scanning electron microscopy (SEM).
- Determination of the hardness of the base material and weld metal in the as-welded condition and after post-weld heat treatment.

CHAPTER 2: LITERATURE REVIEW

2.1 PRINCIPLES OF THE SHIELDING METAL ARC WELDING PROCESS

The shielding metal arc welding (SMAW) process occurs when the arc is established between the flux coated electrode and the base material. The heat from the electric arc decomposes the flux components and melts the core wire. The molten metal and the slag are transferred through the arc (Figure 2.1). The flux covering forms slag. Due to the low density of the slag, it floats on the pool surface, solidifies and protects the weld metal. SMAW can operate with both a direct current (DC) power supply, with electrode positive (DCEP) or negative (DCEN) or alternating current (AC) power supplies, depending on the coating design.

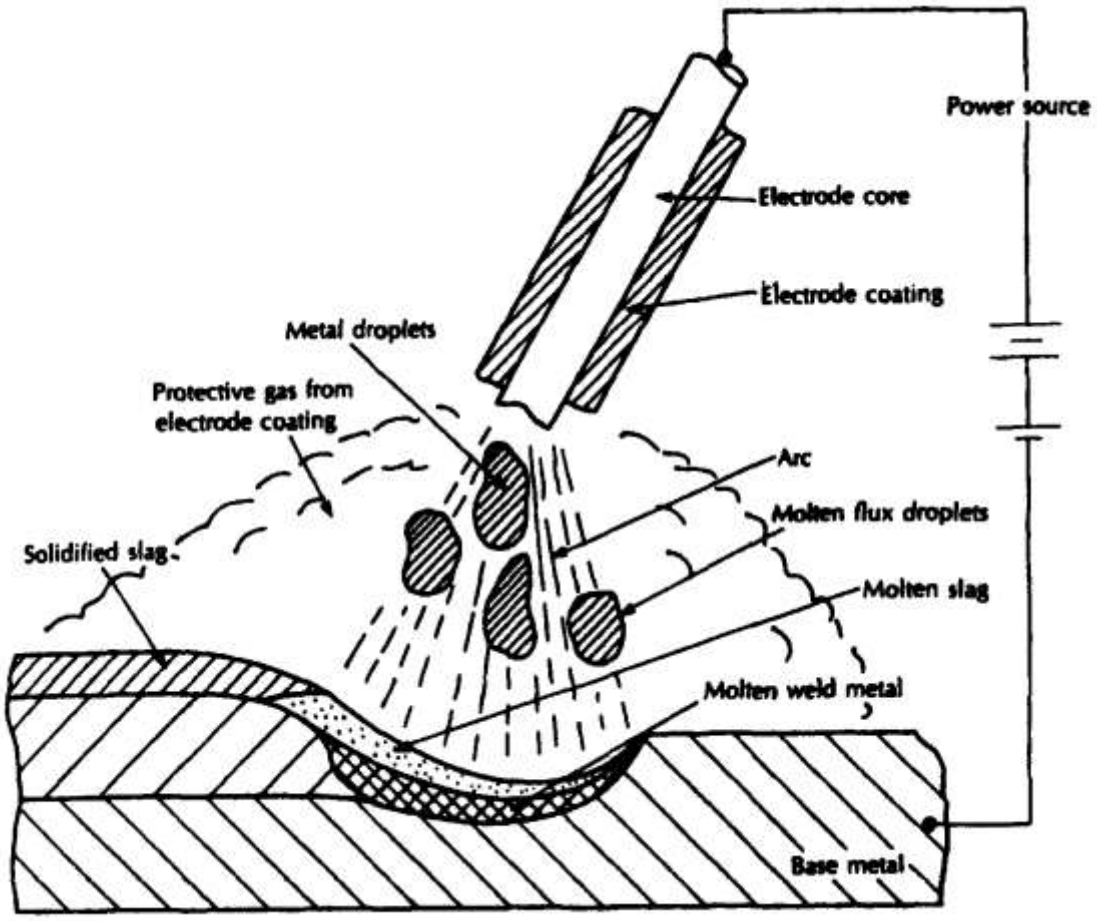

Figure 2.1: Principles of the manual metal arc welding process [6].

2.2 SMAW ELECTRODE DEVELOPMENT

SMAW covered electrodes are developed mainly based on the chemical composition of the weld metal because there is a reliable correlation between the weld metal chemistry and all weld metal mechanical properties.

SMAW covered electrodes for low alloy steels generally consist of a low carbon steel core wire (typical composition: 0.08 wt% carbon; 0.5 % manganese; 0.02 wt% silicon) and a flux covering with different types of raw materials. The surface of the core wire should be clean from wire drawing soap and rust for proper bonding with flux coating during extrusion. Raw materials typically used for the manufacturing of coatings for low alloy steel electrodes are grouped in Table 2.1, according to their primary and secondary functions. The constituents of flux coverings for manual electrodes carry out several functions. Some functions are essential to the welding operation while others contribute to variation in welding characteristics or weld metal properties (see Table 2.2). When designing an electrode to meet a specific purpose, the designer needs to select raw materials which give optimum balance for good extrusion and green bond strength (during manufacturing operation), efficient welding characteristics and good weld metal properties. The low alloy electrodes are hydrogen controlled thus the use of organic material (such as cellulose) to the coating is prohibited because of its high affinity for absorption of moisture.

Table 2.1: Raw materials commonly used in the formulation of fluxes for low alloy SMAW electrodes and their functions [7].

Raw material(s) description	Chemical formula	The function of raw material	
		Primary function	Secondary function
Calcium carbonate (Calcite)	$CaCO_3$	Shielding gas	Oxidizing agent, slag former, arc stabilizer (high quantity)
Fluorspar	CaF_2	Slag former	Fluxing agent
Potassium feldspar	$K_2O.Al_2O_3.6SiO_2$	Slag former	Arc stabilizer
Mica	$K_2O.Al_2O_3.SiO_2$	Extrusion agent	Slag former
Sodium, potassium and calcium alginates	$(C_6H_7O_6Na)_n$, $KC_6H_7O_6$, $(C_6H_7O_6)_2Ca$	Extrusion agent	
Iron powder	Fe	Slag former	Arc stabilizer
Titanium dioxide	TiO_2	Slag former	
Sodium and potassium silicates	$NaSiO_3$[(1)], K_2O_3Si[(1)]	Binder	Arc stabilizer
Ferrosilicon	FeSi	Deoxidizer	Alloying
Ferromanganese	FeMn	Alloying	Deoxidizer

Table 2.1: Continued

Raw material(s) description	Chemical formula	Function of raw material	
		Primary function	**Secondary function**
Ferrochromium	FeCr	Alloying	Deoxidizer
Ferromolybdenum	FeMo	Alloying	Deoxidizer
Ferrovanadium	FeV	Alloying	Deoxidizer
Ferro-niobium	FeNb	Alloying	Deoxidizer
Electrolytic Nickel	Ni	Alloying	

(1) mean raw material is added as a liquid in the formulation

Table 2.2: Characteristic features of different types of coating [8].

Coating type	Cellulose	Acid	Rutile	Basic
Composition (wt%)				
Cellulose	40	-	-	-
Magnetite Fe_2O_3	-	50	10	-
Rutile (TiO_2)	20	-	45	-
Fluorspar (CaF_2)	-	-	-	45
Fe-Mn	15	20	-	5
Quartz (SiO_2)	25	20	20	10
Calcite ($CaCO_3$)	-	10	10	40
Potassium water glass (K_2SiO_3 / Na_2SiO_3)	yes	yes	yes	yes
Droplet transfer	medium-sized droplets	fine droplets	medium-sized to fine droplets	medium-sized to big droplets
Toughness value	good	normal	good	very good
Current type/ polarity	~ / +	~ / +	~ / +	= / +
Gap bridging ability	very good	moderate	good	good
Welding positions	PG, (PA, PB, PC, PE, PF)	PA, PB, PC, PE, PF, PG	PA, PB, PC, PE, PF, (PG)	PA, PB, PC, PE, PF, PG
Sensitivity to hydrogen cracking	low	high	low	very low
Weld appearance	moderate	good	good	moderate
Slag properties	almost no slag	slag solidification time long	slag solidification time medium	slag solidification time short
Slag detachability	good	very good	very good	moderate
Characteristic features	spatter, little slag, intensive fume formation	Low melting efficiency	universal application	low burn-out loses hygroscopic pre-drying

2.3 FLUX FORMULATION DESIGN

The SMAW electrode consists of different types of flux covering, namely rutile, cellulosic, basic and acid, depending on the properties required. High rutile type (TiO_2) flux offers improved arc properties and self-lifting slag, while a basic flux provides cleaner weld metal with lower inclusion content and better mechanical properties than the rutile type. The cellulosic type flux provides deep penetration to the joint. Such electrodes are used to weld high strength pipe steel butt joints in the vertical up and down direction. Acid flux has a high iron oxide content and is suitable for out-position welding. Some quantitative guidelines into the formulation design of these fluxes with some characteristic features are given in Table 2.2.

The flux covering for SMAW electrodes should generally fulfill the following functions [9, 10]:

- The flux covering should form an electrical insulation and mechanical barrier to prevent core wire fusing on to the base metal due to accidental touch.
- It should provide a stable arc because of the presence of readily ionisable compounds such as sodium and potassium silicates in the flux covering.
- The flux covering should make it easier for constituents such as calcium carbonate and potassium feldspar to decompose in the heat of the arc and provide gases from the electrode tip to minimise the effect of oxygen and nitrogen from the atmosphere.
- The flux coating should control the rate of metal deposition and penetration.
- Slag should be easy to remove, with self-lifting characteristics and low spatter volumes.
- It should provide resistance to moisture pickup to prevent hydrogen embrittlement in the weld metal.
- The flux covering should provide metal transfer from the melting core wire tip in the form of small droplets.
- It should provide deoxidisers added in the form of ferrosilicon and ferromanganese to deoxidise the weld metal and improve the mechanical properties.

- The flux covering should provide alloying elements such as chromium, vanadium, molybdenum, and niobium to the weld metal, added in the form of ferro-alloys to improve the mechanical properties.
- It should provide proper viscosity during welding for out-of-position welding.
- The flux covering should produce a smooth weld contour with good wetting action during welding.

The formulation design according to AWS 5.5 E9018-B9 low hydrogen potassium iron powder SMAW electrode has a flux covering which is highly basic, consisting mostly of calcium carbonate–fluorspar (see Table 2.2). It provides a basic type of slag and promotes the transfer of alloying elements from the covering to the weld across the arc.

2.3.1 Extrusion and binding agents

Soluble extrusion agents such as gums, alginates (such as calcium, potassium, and sodium), starches and carbohydrates provide slip during extrusion and contribute to the toughness of the wet flux by improving the mechanical strength of the coating and deformability after it has been extruded.

Binding agents such as sodium and potassium silicate solutions are added to the dry mix to provide coating strength and to improve adhesion to the core wire. The extruded paste should be strong when wet (i.e. have good “green” strength) for the electrodes to hold its shape well and withstand various pressures exerted on it during the buffing process. The binder should also result in enough dry strength on the electrode to be able to withstand rough handling after the baking process. These silicates can be used together or separately, depending on the flux formulation. However, it is critical to note that when these silicates are added together in the formulation that potassium is kept to a minimum in low hydrogen-controlled electrodes. The potassium silicate is hygroscopic thus when added in a large quantity in the low hydrogen flux formulation absorbs moisture which is difficult to remove during baking.

2.3.2 Arc stabilisation and shielding

A welding arc is defined as a sustained electrical discharge through a high-temperature conducting plasma producing sufficient thermal energy useful for joining of metals by fusion [11]. Arc stabilizers are compounds that decompose readily into ions in the arc, such as potassium oxalate, potassium silicate, sodium silicate, potassium carbonate, calcium carbonate, potassium titanate, and lithium carbonate. These compounds increase the electrical conductivity of the arc. The arc stability relies on the ionisation potential of the atoms within the arc plasma. A low value for the ionisation potential of the atom means only a low voltage is required to remove an electron from an atom to generate an ion. The arc stability which is related to the distance the arc can be lengthened before the arc is extinguished. Arc stability has an influence on the weld bead morphology [11]. Poor arc stability may affect the electrode melt rate, the composition of the deposited weld metal and cause defects (such as porosity, blow holes and slag entrapment.).

Gaseous shielding is provided by the decomposition of calcium carbonate ($CaCO_3$) at a temperature around 500ºC from the flux constituents to produce calcium oxide, calcium dioxide ($C0_2$) and carbon monoxide (CO) gases around the arc as shown by the equations 2.1 and 2.2 below [10];

$$\mathbf{CaCO_3 \longrightarrow CaO + C0_2} \qquad \mathbf{(2.1)}$$

$$\mathbf{2CO_2 \longrightarrow 2CO + O_2} \qquad \mathbf{(2.2)}$$

The CO_2 dissociates into CO and O_2, providing a gas shield to protect the weld pool. The gaseous oxygen which enters the weld pool is de-oxidised to keep it as low possible in the weld metal by deoxidisers such ferrosilicon. The shielding provided allows for a low hydrogen content, and a clean weld metal with good mechanical properties.

2.3.3 Slag formers and detachability

Calcium carbonate, calcium fluoride, silica and titanium dioxide are used as a slag forming system in the flux of basic electrodes. It is reported by Brown [9] that calcium fluoride must be controlled because of the fluorine that is evolved as welding fumes which may give problems of arc stability and poor slag removal. The slag must melt

below the melting of the temperature of the steel (approximately1450ºC) with a density lower than that of the steel to reduce slag entrapment in the weld deposit. In addition, the slag must have the proper viscosity in the temperature range of 1450 to 1550ºC and detach easily from the weld deposit [9].

Slag detachability is critical during welding because the presence of slag on the weld surface will influence the integrity of the weld during multi-pass welds and increase downtime during fabrication. It is reported that slags containing spinel ($MgAl_2O_4$) and cordierite ($Mg_2Al_4Si_5O_{18}$) are very difficult to remove [12, 13]. It has also been reported that the presence of $(CaO)_2SiO_2$, Cr_2TiO_5 and $FeTiO_5$ ease the detachability of slag from the weld deposit. Residual slag on the weld deposit promotes slag inclusions which are detrimental to the integrity of the welded joint. It has been documented that the ease of slag detachability is influenced by the coefficient of thermal expansion of the slag which should be different from that of the weld metal [11].

2.3.4 Viscosity of slag

Viscosity is defined as the property of the fluid to resist flow or internal flow [11]. The viscosity of slag may be expressed in qualitative terms; creamy or watery, thick or thin. The viscosity controls the ability of the molten flux (slag) to cover and protect the molten weld metal. The flux viscosity also determines the removal of contaminants between slag and weld metal resulting in alloy additions to the weld metal. If slag has a high viscosity at the temperatures of welding, it will be sticky and flow slowly. Heavy coatings of slag, whether of high or low viscosity, are difficult to manipulate in vertical or overhead welding positions, hence they are mainly used in flat position (for example AWS 5.1 E 7024, iron powder electrode). A too low viscosity slag is very undesirable for the vertical and overhead welding positions because the slag will drip. A slag of high viscosity is desirable in the flat position [14]. The viscosity of the slag may be controlled by varying the composition or temperature of the flux, by varying the amperage during welding.

2.3.5 Deoxidation and alloying ability

Deoxidation is performed by using FeSi and FeMn. Nickel, molybdenum, chromium, vanadium, and niobium are added to the flux covering as metallic or ferro-alloy powders. The recovery of the alloying elements from the electrode covering will not be greatly different from the recovery of the same elements in the electrode core wire. When elements added to the electrode covering are oxidizable, complete transfer to the weld pool may not occur. The shape and particle size of FeSi and FeMn in the covering also have an influence on the efficiency of transfer. Very fine powdered oxidizable metals and alloys will have a lower recovery than coarse particles [15]. Table 2.3 shows the approximate recovery of elements from the electrode covering.

Table 2.3: Recovery of elements from electrode covering [16].

Alloying element	Form of material in electrode covering	Approximately recovery of element, %
Carbon	Graphite	75
Manganese	Ferromanganese	75
Phosphorus	Ferrophosphorus	100
Sulphur	Iron Sulphide	15
Silicon	Ferrosilicon	45
Chromium	Ferrochromium	95
Nickel	Electrolytic Nickel	100
Copper	Copper metal	100
Niobium	Ferroniobium	70
Titanium	Ferrotitanium and /or Titanium dioxide	5
Molybdenum	Ferromolybdenum	97
Vanadium	Ferrovanadium	80
Berylium	Copper-beryllium alloy	0
Boron	Ferroboron	2
Nitrogen	Nitrided manganese	50
Tungsten	Ferrotungsten	80
Aluminium	Ferroaluminum	20
Zirconium	Nickel-zirconium alloy	5

2.3.6 The Delta Quantity

The delta quantity is defined by Kin-Ling [11] as the amount of specific elements that are gained or lost during the welding process. It is represented mathematically using the equation below;

$$\Delta\text{elta Quantity} = \text{Analytical content} - \text{Estimated content} \qquad (2.3)$$

The analytical content is determined by the analysis of the weld metal. The estimated content is the sum of the potential contributions from the core rod and the base metal. A negative delta quantity indicates that a loss of specific elements to the slag or as a gaseous loss, form. The delta quantity plays a pivotal role in electrode development by understanding the role of flux ingredient in the contribution to the final weld composition. Figures 2.2 and 2.3 show a transfer of manganese and titanium for welds made with SiO_2 – TiO_2 – CaO -1Na_2O flux at a constant Si_2O content in the flux and varying heat input [13]. According to the data in Figure 2.2, the manganese is lost to the slag with changes in titanium dioxide in the flux. Manganese is an important element increasing both the hardenability and the toughness of the weld metal. A proper balance of the flux composition should be maintained to control the manganese content in the final composition of the weld. Figure 2.3 shows a constant increase in delta titanium with increasing titanium dioxide content of the flux. TiO_2 should be controlled in the flux to prevent high titanium content in the weld metal which is detrimental to the toughness.

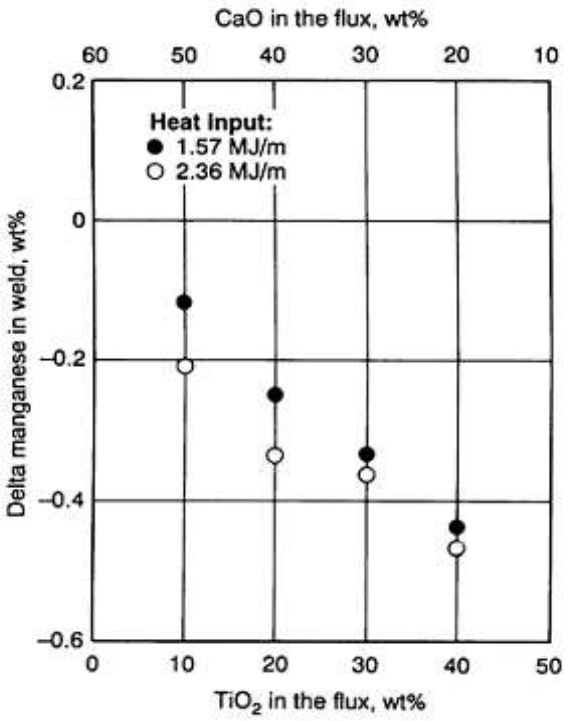

Figure 2.2: Changes in manganese content (analytical content minus the estimated content) in the weld versus the variation in flux composition as a function of heat input [13].

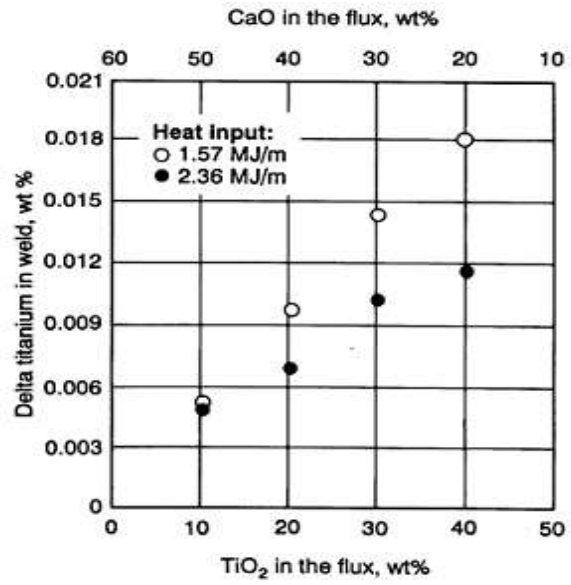

Figure 2.3: Changes titanium content (analytical content minus the estimated content) in the weld versus the variation in flux composition as a function of heat input [13].

2.3.7 Flux basicity

Basic fluxes remove the sulphur and phosphorus from the weld metal. In general, the higher the basicity, the lower the non-metallic inclusion content of the weld metal. It has also been reported that the oxygen content of the weld metal decreases as the flux basicity increases (Figure 2.4). There are a number of mathematical expressions for slag basicity, of which the International Institute of Welding's (IIW) index BI (original by Tuliani, Boniszewski, and Eaton) and the Mori index BL are commonly used [10];

$$BI = \frac{\%CaO + \%\,CaF_2 + \%MgO + K_2O + Na_2O + \tfrac{1}{2}(\%MnO + \%FeO)}{\%SiO_2 + \tfrac{1}{2}(\%Al_2O_3 + \%TiO_2 + \%ZrO_2)} \quad (2.4)$$

$$BL = 6.05*CaO+4.8*MnO+4.0*MgO+3.5*FeO-(6.31*SiO_2+4{,}97*TiO_2+0.2*Al_2O_3) \quad (2.5)$$

According to the IIW index, the flux is acidic when the BI is less than 1, neutral when is 1.0 to 1.5, semi-basic when is between 1.5 and 2.5 and basic when greater than 2.5. When using the Mori index, the slag is basic when BL is positive, acidic when it is negative and neutral when the value of BL closer to zero. The influence of slag basicity on notch toughness has been reported by Easterling [17]. Figure 2.5 shows that a considerable difference exists in the impact strength of the weld between basic and rutile electrodes. The basic weld metal exhibits a steeper transition curve and a wider scatter band with high upper shelf values. The rutile weld metal gives less scatter and since the upper shelf values are low, the transition temperature range is less well defined. The reason for these differences is found in the distribution and form of slag inclusions, with the rutile weld metal having a high volume of inclusions [17].

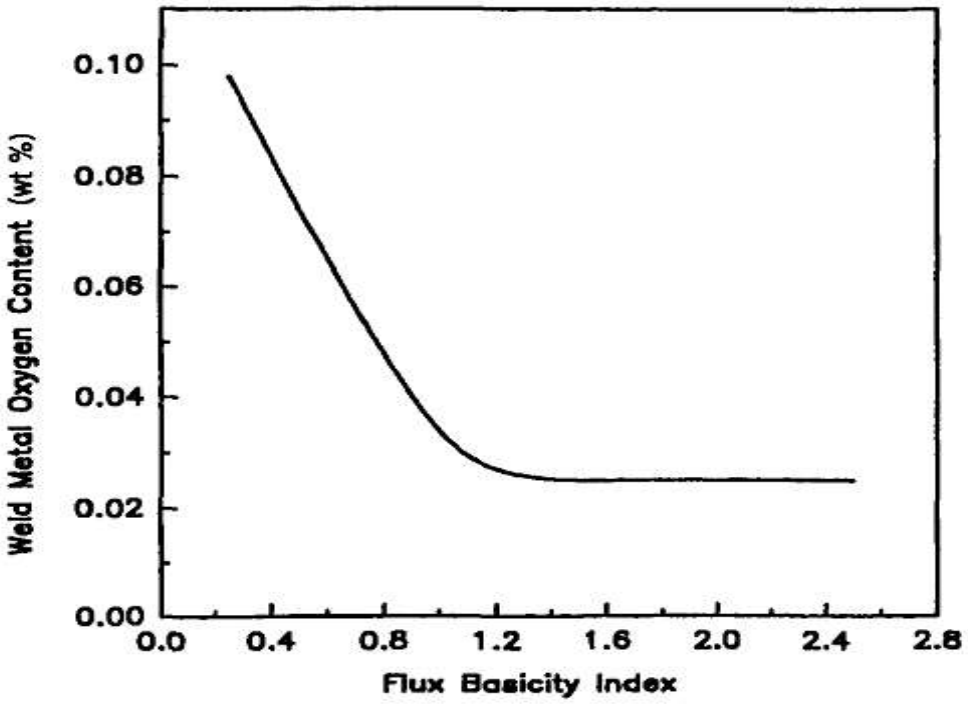

Figure 2.4: Correlation between the toughness of weld metal and its residual oxygen content as influenced by the basicity index [6].

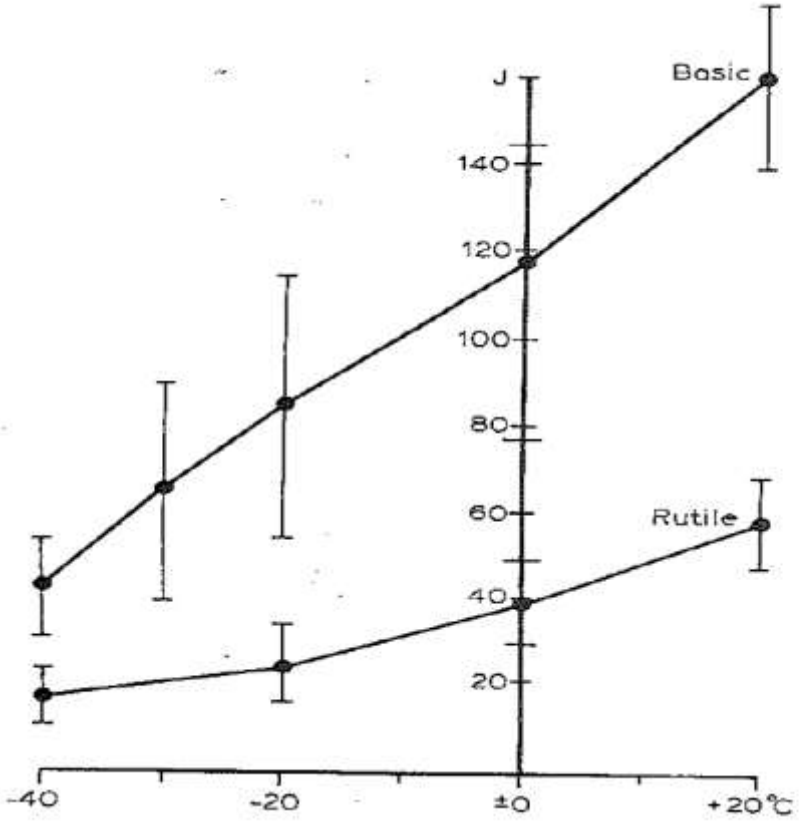

Figure 2.5: Influence of the type of electrode coating on the Charpy V impact energies of the weld metal [17].

2.4 The Welding Electrode Manufacturing Process

The welding electrode manufacturing process consists of the following stages (Figure 2.6):

1. Processing of mild steel wire, including wire drawing, straightening and cutting;
2. Weighing, drying, and blending of flux constituents;
3. Wet mixing of flux;
4. Extrusion;
5. Baking and
6. Packaging.

Quality checks such as testing of raw materials, in-process materials, and final products are performed as quality control measures during the manufacturing process.

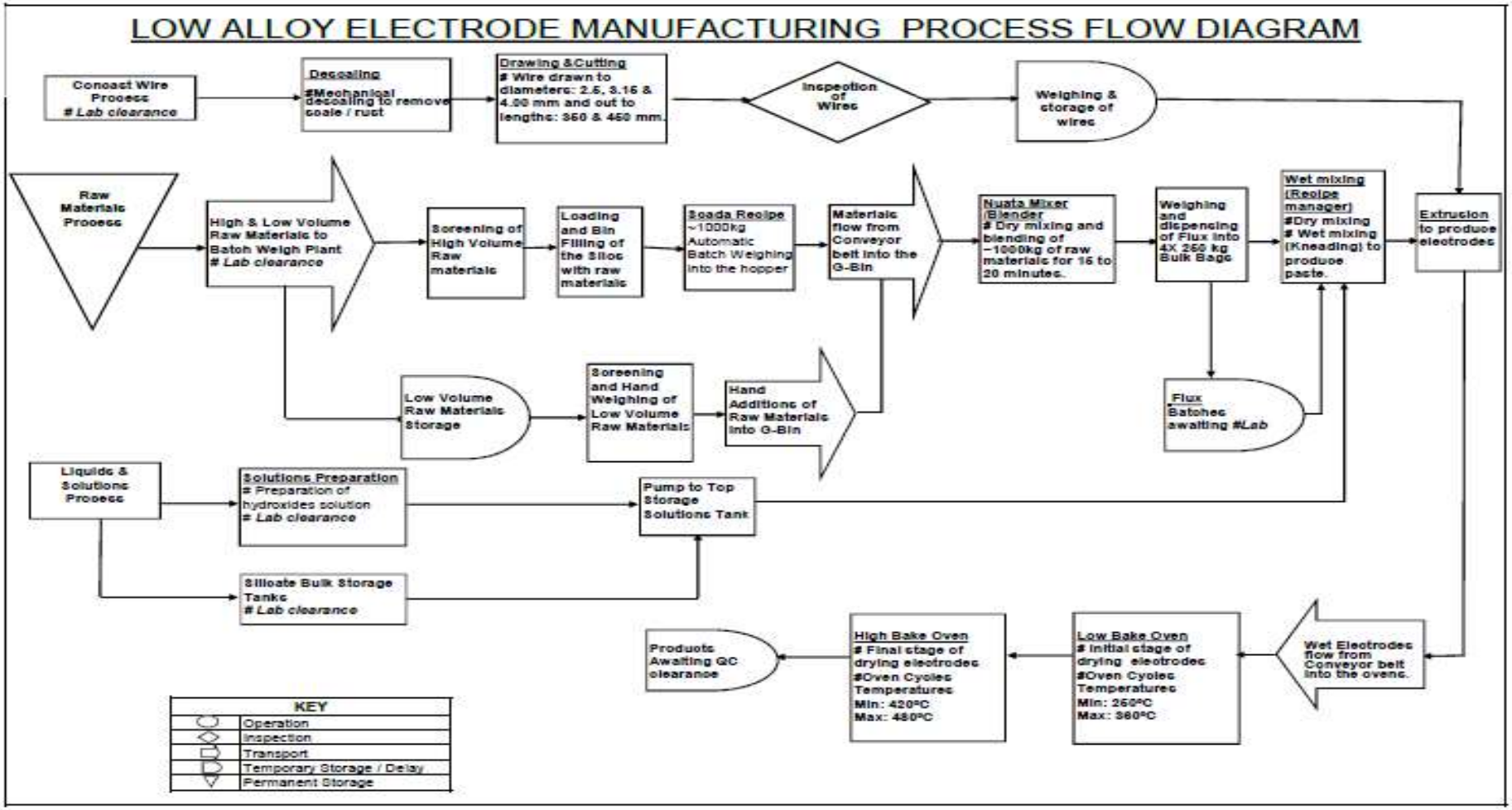

Figure 2.6: The Low Alloy Electrode Manufacturing Process Flow Diagram [18].

2.5 Creep resistant steels

Creep is defined as the progressive deformation at a constant stress and temperature [19]. It is a time-dependent mechanism by which a material plastically deforms when subjected to a constant stress either below or above that of the yield strength at temperature.

The development of 9-12Cr ferritic/martensitic creep resistant steels is shown in Figure 2.7 [1]; the engineering design of a power plant is based on the ability of these steels to support a stress of 100MPa for 10^5h at the service temperature. The first high chromium ferritic steel was developed in the 1960s in Europe, with a 9Cr-2Mo (named, EM 12) steel developed in France for tubing applications [20]. This steel had a duplex microstructure containing δ-ferrite with a low impact toughness. X20CrMoV12-1 (12Cr-1Mo) was developed in Germany around the same time as EM12; this steel was used mainly for tube and pipe applications. The X20CrMoV12-1 exhibited a fully martensitic microstructure, however, it had poor weldability and inferior creep strength when compared to the EM 12 above 520ºC. Later in the 1970s, a modified 9Cr-1Mo was developed by Oak Ridge National Laboratory (USA) for tubes (T91) and pipes (P91).

The modified 9Cr-1Mo alloy superseded both X20CrMoV12-1 and EM 12 and had superior mechanical properties owing to a tempered martensite microstructure stabilised by $M_{23}C_6$ carbides, solution strengthening by molybdenum and a fine distribution of vanadium/niobium rich carbonitride (MX, where M=V, Nb and X=C, N) precipitates. Further development resulted in an improvement in creep strength in steels such as NF616 and HCM 12A (see Figure 2.7 and Tables 2.4). Table 2.4 shows the history of the development of 9-12Cr steels for 10^5 hours creep rupture strength at 600ºC for different generations and years of development [21].

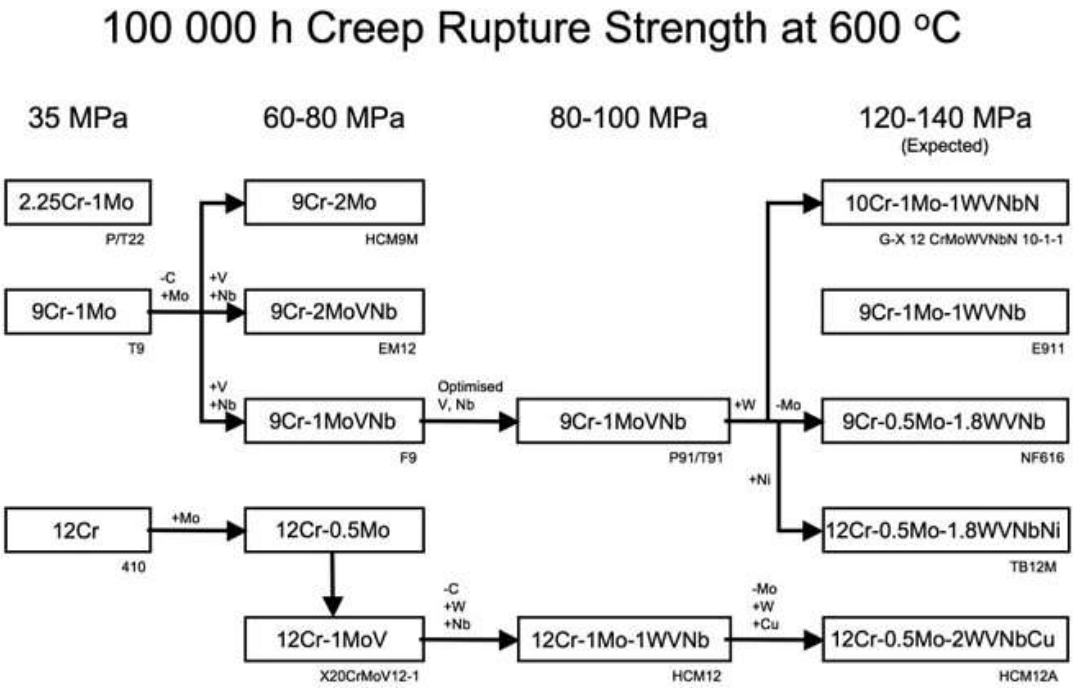

Figure 2.7 Generations in the development of 9-12Cr ferritic/martensitic steels [21].

Table 2.4: History in the development of ferritic/martensitic 9-12Cr steels [21].

Generation (Years)	Alloy steel modification	10^5 hr creep rupture Strength (MPa) @ 600ºC	Maximum temperature used (ºC)	Steel type	Typical chemical composition, wt.%										
					C	N	Si	Mn	Cr	Mo	V	Nb	W	Co	Cu
1 (1960-70)	Additions of Mo or Nb, V to 12Cr and 9CrMo steels	60	565	ASME T9	0.12	-	0.6	0.45	9.0	1.0	-	-	-	-	-
				HCM9M	0.12	-	0.3	0.45	9.0	2.0	-	-	-	-	-
				EM12	0.10	-	0.4	0.10	9.0	2.0	0.30	0.40	-	-	-
2 (1970-85)	Optimization of C, Nb, and V	100	593	X20CrMoV-12-1	0.20	-	0.4	0.60	12.0	1.0	0.25	-	-	-	-
				ASME P/T91	0.10	0.05	0.4	0.45	9.0	1.0	0.20	0.08	-	-	-
				HCM 12	0.10	0.03	0.3	0.55	12.0	1.0	0.25	0.05	1.0	-	-
3 (1985-95)	Partially substitution of W for Mo	140	620	GX12CrMoWVNbN-10-1-1	0.13	0.05	0.3	0.6	10.5	1.0	0.23	0.08	1.0	-	-
				NF616 (ASME P/T 92	0.07	0.06	0.1	0.45	9.0	0.5	0.2	0.05	1.8	-	-
				HCM 12A (ASME P/T 122	0.11	0.06	0.1	0.60	12.0	0.4	0.2	0.05	2.0	-	1.0
4 (Future)	Increase of W and addition of Co	180	650	SAVE 12	0.10	0.04	0.3	0.2	11.0	-	0.2	0.07	3.0	3.0	-

2.6 Strengthening mechanisms in creep resistant steels

The 9-12Cr ferritic/martensitic creep resistant steels are strengthened by the following four mechanisms; (i) Solid solution hardening, (ii) Precipitation hardening, (iii) Dislocation hardening and (iv) Subgrain boundary hardening [22].

Precipitation hardening is one of the most important strengthening mechanisms in these high Cr creep resistant steels. A dispersion of fine precipitates is responsible for stabilising the free dislocations in the matrix and sub-grain structures, which improve the dislocation hardening and sub-boundary hardening (see, Figure 2.8) [22, 23].

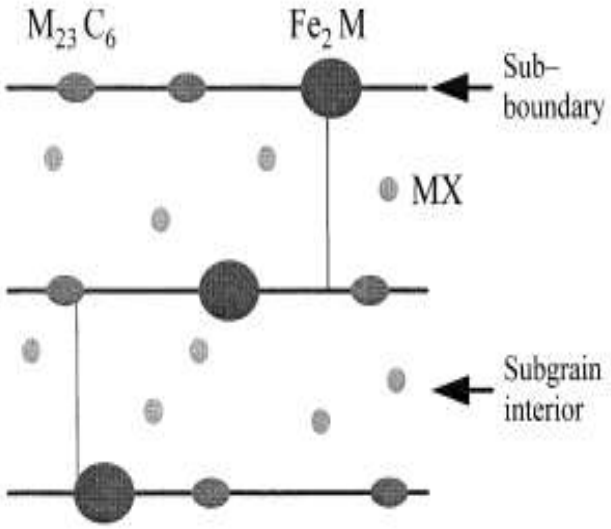

Figure 2.8: Schematic diagram of precipitates in high Cr ferritic steel [23].

The development of the modified P91 steel containing niobium and a controlled amount of nitrogen has led to worldwide usage in the superheated tubing, header, and piping [24]. The superior mechanical properties of this 9Cr-Mo-V-Nb-N steel is derived from its strong carbide and carbonitride formers such vanadium and niobium, leading to precipitation of various particles such as $M_{23}C_6$ and MX type precipitates, vanadium nitride (VN) and vanadium-niobium carbonitrides (V,Nb)(N,C) in addition to solid solution strengthening by Mo. The $M_{23}C_6$ precipitates predominate along the prior austenite grain boundaries (PAGBs) as well as on the lath boundaries [24, 25, 26]. It is reported that the MX precipitates are comparatively smaller than $M_{23}C_6$ carbides and that they are distributed on the boundaries of the laths, blocks and packets as well

as on the prior austenite grain boundaries (see Figure 2.9). The stability of the precipitates obstructs and pins the movement of dislocations, refines grains during normalizing and delays plastic deformation [27, 28]. However, it is reported that the strength of P91 steel can be lost due to precipitation of the Z-phase and laves phase after exposure to elevated temperatures for longer periods during service [29].

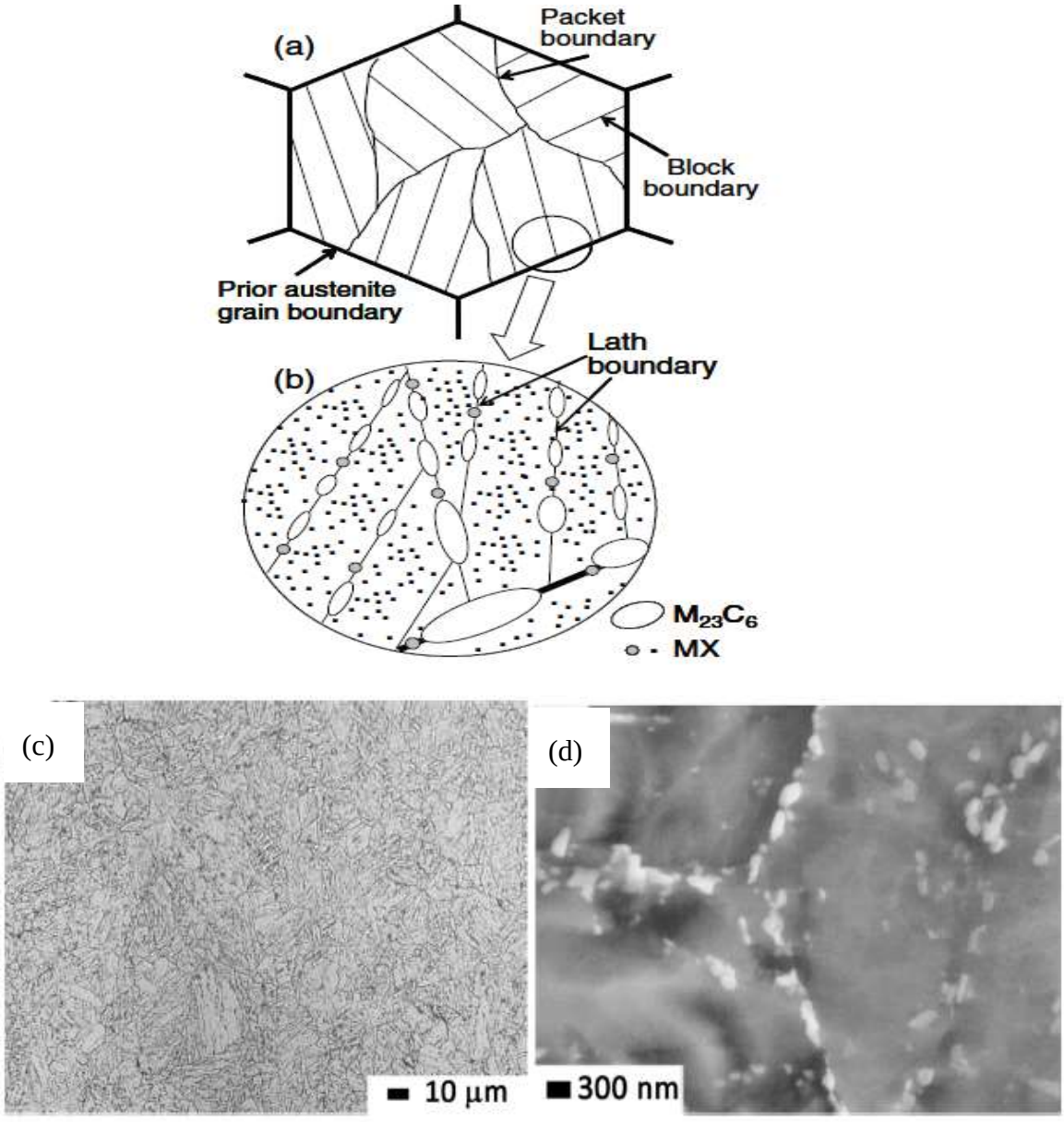

Figure 2.9: (a) and (b) Schematic diagram illustrating the role of tempered martensite in 9-12Cr steels [26]. A typical microstructure of as-received grade P91 steels (c) optical micrograph showing tempered martensite and (d) SEM micrograph showing the distribution of precipitates [28].

2.7 Effect of alloying elements in creep resistant steels

2.7.1 Carbon (C)

Carbon is an austenite stabilising element and has a greater solubility in FCC than in the BCC iron (Fe) structure. In sufficient amounts, carbon combines with other carbide-forming alloying elements (such as chromium, molybdenum, vanadium, and niobium) and forms carbides which provide precipitation strengthening. These carbides improve the high-temperature creep strength and increase the microstructural stability under prolonged exposure at elevated temperatures. However, the carbon content should not be very high because it may reduce the weldability of the alloy. Normally the carbon content of the P91 alloy steel is restricted within the range of 0.05-0.15 wt% to obtain a balance between weldability and creep strength [30].

2.7.2 Chromium (Cr)

Chromium is a ferrite stabiliser and provides a stable oxide scale which offers protection against high temperature oxidation. The phase diagram of the Fe-Cr system shows that a two-phase narrow temperature range exists between austenite and ferrite (Figure 2.10). With a composition near 9%Cr, there is an austenite region between 820 to 1200ºC [1]. However, with a chromium content over 12.0 wt.%, the risk of forming δ-ferrite increases which then compromises the strength and toughness of the steel. Therefore, for a better balance of good mechanical and oxidation properties, the chromium content should be maintained within the range of 9.0 to 12.0wt.% [25]. Chromium is a strong carbide former; forming the $M_{23}C_6$ carbide which is predominantly Cr-rich but also contains other elements such as iron (Fe), molybdenum (Mo) and tungsten (W).

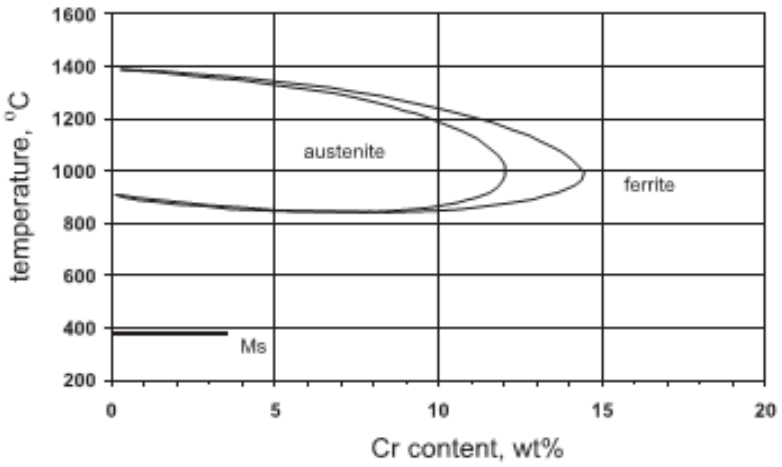

Figure 2.10: Fe-Cr constitutional diagram [1].

2.7.3 Molybdenum (Mo)

Molybdenum provides strength to the P91 alloy steels in the form of solid solution strengthening. It is also one of the strong carbide formers. By forming coherent Mo_2C precipitates it also improves the creep strength of the alloy. Below 0.5wt%, the desired effect cannot be obtained. Molybdenum content higher than 1.5wt% degrades the P91 steels by the formation of laves phase (Fe_2Mo) precipitates which reduce the impact toughness significantly during service at high temperatures [25].

2.7.4 Manganese (Mn)

Manganese is added as a deoxidiser and austenite stabiliser. Studies show that manganese plus nickel reduce the A_{c1} temperature in P91 as both additions are austenite stabilisers and this will result in lowering of the $\alpha \leftrightarrow \gamma$ transformation temperature, which narrows the window for post weld heat treatment (PWHT) [31]. According to the ASME Boiler and Pressure Vessel Code the specified maximum allowable PWHT temperatures in P91 steel welds as a function of Ni + Mn content of the weld metal are specifies as [32]:

- 800ºC if Mn +Ni is below 1 wt.%;
- 790^0C if Mn + Ni is between 1.0 and 1.5 wt%; and
- 775^0C if the Mn + Ni content is unknown.

2.7.5 Nickel (Ni)

Nickel is a strong austenite stabilizer and its addition to the P91 steels prevents the formation of δ-ferrite, resulting in an improvement in the fracture toughness [32]. Nickel also increases the hardenability, resulting in the formation of martensite at a wider range of cooling rates. As already mentioned in section 2.7.4, nickel has a strong effect in lowering the A_{c1} temperature in P91 steel and its content should be maintained below 0.8 wt.%. The addition of nickel to the filler metal is to counteract the negative impact of ferrite formers such as niobium, vanadium, molybdenum on the toughness of the weld metal for the A_{c1} temperature to be in the correct range for proper PWHT heat treatment [33].

2.7.6 Silicon (Si)

Silicon is a deoxidising agent and ferrite stabiliser. It is reported that silicon decreased the toughness and creep strength of the P91 steel by promoting laves phase precipitation when added in a large quantity. However, it is important to ensure that sufficient Si is added (usually approximately 0.3wt%) to achieve adequate deoxidation and weldability [31].

2.7.7 Vanadium (V)

The addition of vanadium is beneficial when it comes to precipitation strengthening. Vanadium combines with carbon and nitrogen to form precipitates such as vanadium nitride (VN) and vanadium carbonitride V (C, N) that are more stable than chromium and molybdenum carbonitrides. The precipitates have a low coarsening rate at high temperatures and are therefore effective in improving the creep strength of P91 steels.

2.7.8 Niobium (Nb)

Niobium is a strong carbide former and it is believed that the niobium-rich carbides are stable to such an extent that the temperature should exceed the austenitizing temperature for these carbides to dissolve [22]. In the presence of carbon and nitrogen, niobium forms niobium nitrides (NbN) and niobium carbonitrides Nb(C, N) which contribute towards precipitation strengthening by improving the creep strength

of the P91 steel. Niobium should be limited within the range of 0.02-0.2wt% for effective precipitation strengthening.

2.7.9 Nitrogen (N)

Nitrogen is an austenite stabiliser and has a low solubility in ferrite. As already mentioned above, it forms stable MX carbonitride precipitates in combination with vanadium and niobium which are effective in improving creep rupture strength in P91 ferritic/martensitic steels. The nitrogen content should be maintained at below 0.05wt%, to avoid degradation of mechanical properties and weldability.

2.8 Determination of A_{c1}, A_{c3} M_s and M_f phase transformation temperatures

2.8.1 Overview

The A_{c1} transformation temperature is defined as the temperature at which the austenite phase starts to form during the heating process. The A_{c3} temperature is the transformation temperature at which the austenite phase has formed completely during heating. Accurate knowledge of the temperatures at the start of austenite formation (A_{c1}), its completion (A_{c3}) during heating as well as the start (M_s) and the completion or finish of martensite formation (M_f) during cooling of grade P91 welds will prevent re-austenitization and ferrite formation during post weld heat treatment (PWHT) which is detrimental to the toughness and creep resistance of the welded joints [5].

Three measuring techniques are used to measure the A_{c1}, A_{c3} and M_s transformation temperatures and structural changes, namely Single Sensor Differential thermal analysis (SS-DTA), Dilatometry Analysis (DA) and Differential Scanning Calorimetry (DSC). These measuring techniques are used in the development of welding consumables, new alloys, construction of continuous cooling transformation (CCT) diagrams, construction of phase diagrams, welding studies and heat treatments. In the present study, the focus is on the use of DA to determine phase transformation temperatures of the P91 steels. Differential scanning calorimetry is a technique used to measure the difference in heat flow between a sample and inert reference as a function of time and temperature. The SS-DTA techniques were developed by

Alexandrov and Lippold [34] for phase transformation analysis that determines the enthalpy in materials during continuous heating and cooling.

2.8.2 Dilatometry Analysis

Dilatometry is a technique to quantitatively measure phase transformations in steels as described in ASTM A1033-04 [35]. This equipment measures the expansion and contraction of the specimen during the temperature change. Dilatometry involves heating a sample in a high vacuum by resistive or induction heating and detecting the change in specimen dimension using a contact measuring system. When there is no phase transformation, the specimen diameter or length change should be proportional to the temperature during continuous heating or cooling. During a phase transformation, the difference in density and linear thermal expansion coefficients of different phases, results in a deviation from linear behaviour, as shown in Figure 2.11.

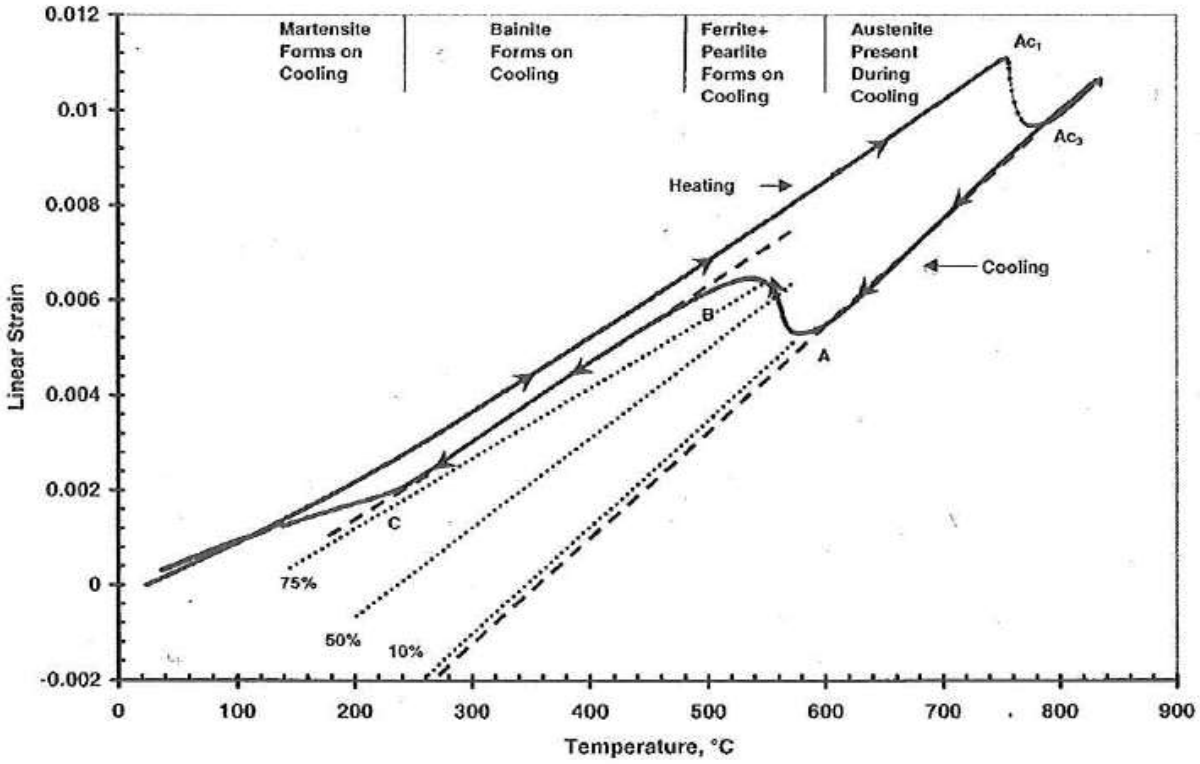

Figure 2.11: Dilatometry curve showing strain versus temperature for continuous cooling [35].

Research work to determine the A_{c1} transformation temperature of the P91 SMAW weld metal using dilatometry has not been published extensively. However, research work has been done by Alexandrov et al [36]. and Santella et al. [37] to determine the A_{c1} and the predictive A_1 transformation temperatures of the welds using dilatometry and predictive formulae.

Alexandrov et al. used SS-DTA and dilatometry (setup with a Gleeble™ 3800 thermo-mechanical simulator) to determine the A_{c1} temperatures of gas metal arc welds (GMAW) and submerged arc welds (SAW) on the weld and base metals on more than seventy P91 grades. They found the A_{c1} temperatures of the P91 weld metals to be in the range 770–801ºC when the Mn + Ni content was between 0.5 and 1.31 wt% (Table 2.5) [36]. The Ac_1 temperatures of the base metal were found to range between 788 to 813ºC in this study (Table 2.5).

Santella et al. used dilatometry (setup with a Gleeble™ 3500 thermo-mechanical simulator) to determine the A_{c1} temperature on two submerged arc weld samples. These samples were heat treated prior to determining the A_{c1} temperature as follows: one weld metal in the PWHT condition (774ºC for 8 hours) and the other after a homogenization heat treatment at 1140ºC for 8 hours [37]. The A_{c1} temperatures were found to be 780 and 800ºC respectively (Table 2.5). The A_{c1} temperature of the homogenized weld sample was 20ºC higher because the sample after this heat treatment closely represented equilibrium. Both these studies revealed that the lower critical temperature was not only controlled by the Mn + Ni content. Other alloying elements have also an influence on the lower critical temperature. In general, it was found that the A_{c1} temperature was influenced by the total balance of austenite and ferrite stabilizers in the weld metals. The effect of heating rate and microsegregation in the weld on the A_{c1} temperature was also reported by Santella et al. The A_{c1} temperature of 21 ºC lower was measured in a slow heating rate sample compared to a fast heating rate. The effect of microsegregation on the microstructure of the weld was found to influence the A_{c1} temperature with those areas showing a high level of Mn+Ni in which the lower critical transformation temperature was suppressed [37].

Twelve different research laboratories were given 9Cr-1Mo steel samples by Nitsche and Mayr [38] to measure the phase transformation temperatures (A_{c1}, A_{c3}, M_s and M_f) and structural changes using single sensor differential thermal analysis and dilatometry analysis. Low A_{c1} values were found under equilibrium conditions and high

values when simulating a welding condition (Table 2.5). Figures 2.12 and 2.13 shows the graphical representation of the results by these participating laboratories. These measurements were performed by simulating equilibrium (slow heating rate) and welding conditions (fast heating rate). The A_{c1} under-equilibrium condition showed less scatter compared to its welding simulation. It is important to note the effect of measuring technique and heating rate on the A_{c1} temperature. The A_{c3} temperatures of the base metal were scattered on both equilibrium and welding conditions (Figures 2.11 and 2.12). From Figure 2.11, the measurements of the A_{c1} temperature were consistent between 10 laboratories. It is noteworthy that two laboratories reported a significantly lower A_{c1} temperature. No reason for this discrepancy was proposed.

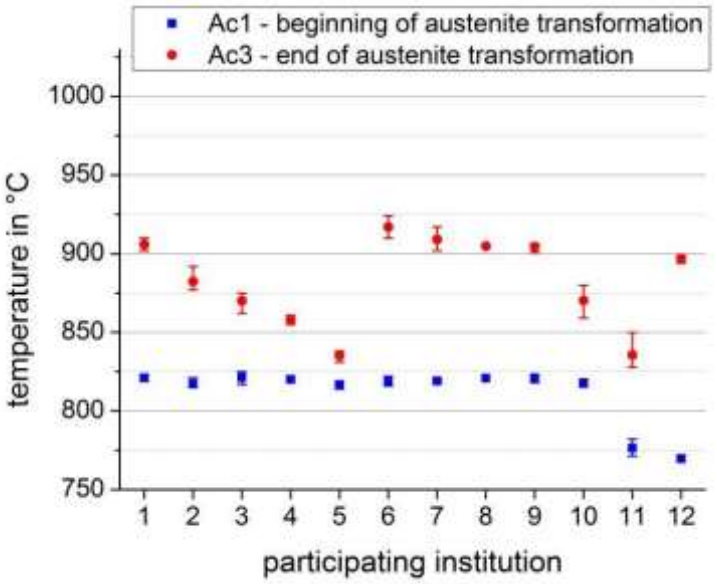

Figure 2.12: A_{c1} and A_{c3} temperatures determined by simulating equilibrium conditions on one P91 base metal [38].

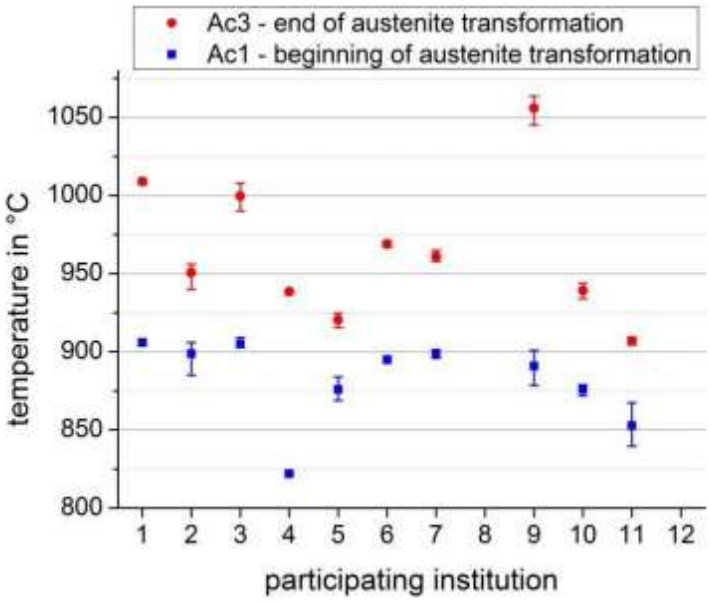

Figure 2.13: A_{c1} and A_{c3} temperatures determined by simulating welding conditions on one P91 base metal [38].

Table 2.5: A_{c1} and A_{c3} temperatures measured during heating and cooling cycles for equilibrium, welding, and fast heating/cooling conditions

No.	Heating /cooling cycle	Nitsche et. al[1] [38]	Nitsche et. al[2] [38]	Alexandrov et. al[1][36]	Santella[3] [37]
1.	Techniques	SS-DTA, DA	SS-DTA, DA	SS-DTA	SS-DTA
2.	Number of samples	Not mentioned	Not mentioned	70	2
3.	Heating rate Temperature (ºC)	10ºC/sec RT to 700	100ºC/sec	10ºC/sec RT to 700ºC	2ºC/min RT to 1050ºC
4.	Heating rate Temperature (ºC)	28ºC/h 700 to 1000	none	28ºC/h 700 to 1000	_
5.	Soaking temperature & time	None	1300ºC for 20 sec	_	_
6.	Cooling rate	10ºC/sec	20ºC/sec	10ºC/sec	6ºC/min
7.	A_{c1} temperature (ºC)	768-825	821-909	770-801 & 788-813	780 & 800
8.	A_{c3} temperature (ºC)	828 - 924	904-1064	Not reported	Not reported

[1]Equilibrium condition, [2]Welding condition & [3]Fast heating / cooling rate

SS-DTA - Single Sensor Differential thermal analysis & DA – Dilatometry analysis

2.8.3 A_1 Predictive formulae

Predictive formulae for calculating the A_1 of the P91 welds were derived by Alexandrov et al and Santella [36, 39].

Alexandrov et al. derived the predictive formula by design of experiments (DoE) and SS-DTA results on more than 70 grades of P91. However, the predictive formula for Alexandrov et al. (equation 2.8) was revised (equation 2.9) in this study based on the findings of Lung Wang [40]. Alexandrov et al. used predictive formulae for P91 steels with copper content between 0.12-0.40 wt% for P91 materials which had a copper content of less than 0.12wt%. The copper content in the current study was less than 0.12wt%, hence equation 2.9 is used as Alexandrov's revised predictive formula. These two equations have differences in the coefficient of the following elements: molybdenum, chromium, vanadium and the constant as shown in equations 2.8 and 2.9 and Table 2.6.

The predictive formula for the A_1 transformation temperature (equation 2.10) was developed by Santella based on computational thermodynamics (Thermocalc^{TM}) and SS-DTA results using three 9%Cr steels. Five reference chemistries were used by Santella, with the ferrite and austenite formers alternatively changed to a minimum, mid and maximum throughout the experiments when deriving the formulae [39]. The predicted A_1 temperatures for grade P91's range were 766 to 856ºC for the base metal and 676 to 862ºC for the weld metal.

Comparison of the revised Alexandrov et al. (equation 2.9) and Santella (equation 2.10) formulae show that the austenite (Ni, Mn, C, N, Cu) and ferrite (Cr, Si, Mo) stabilising elements in the chemical composition of grade P91 are well represented (see Table 2.6). However, copper is not included in the Santella equation. The reference temperature in Alexandrov et al's. equation is also low compared to that of the Santella equation. The influence of the austenite and ferrite stabilisers on the A_1 is exhibited graphically in Figures 2.14 to 2.16. These plots where created using the midrange composition of grade P91. From figures 2.12 to 2.14, a change in the austenite stabilising elements (such as C, N, Ni, and Mn) resulted in a larger increase in the A_1 temperature than the reduction in A_{c1} temperature due to the same incremental change in ferrite stabilising elements (Nb, V, Si, Mo, and Cr).

Alexandrov et al. formula

A_1 (ºC) = 2113 – 243*C -174*N + 87.5*Si – 24.4*Mn + 16.676*Cr^2 – 288.49*Cr – 365.5*Ni^2 + 153.1*Ni + 164*Mo^2 – 299.2*Mo + 1320*V^2 -570*V – 194.3Cu^2 + 83.9*Cu (**2.8**)

Revised Alexandrov et al. formula

A_1 (ºC) = 2122.1 – 243*C -174*N + 87.5*Si – 24.4*Mn + 16.676*Cr^2 – 271.8*Cr – 365.5*Ni^2 + 153.1*Ni + 164*Mo^2 – 306.5*Mo + 1324*V^2 -571.8*V – 194.3Cu^2 + 83.9*Cu (**2.9**)

Santella Formula

A_1 (ºC) = 805 – 67.3C -130.6N + 19.1Si -60.5Mn + 2.5Cr – 72.3 Ni + 18.1Mo + 37.1V (**2.10**)

Table 2.6: Comparison of constant coefficients in the empirical equation for calculating A_1 temperatures for 9Cr-1Mo steels.

Formula	**Alexandrov et al. equation [36]**	**Alexandrov et al. revised equation [40]**	**Santella equation [39]**
Element	**Constant**	**Constant**	**Constant**
Constant	2113	2122,1	805
Carbon (C)	-243	-243	-67,3
Nitrogen (N)	-174	-174	-130,6
Silicon (Si)	87,5	87,5	19,1
Manganese (Mn)	-24,4	-24,4	-60,5
Cr^2	16,676	16,68	
Chromium (Cr)	**-288,49**	**-271,8**	2,5
Ni^2	-365,45	-365,5	
Nickel (Ni)	153,05	153,1	-72,3
Mo^2	164	164	
Molybdenum (Mo)	**-299,2**	**-306,5**	18,1
V^2	1320	1324	
Vanadium (V)	-570	-571,8	37,1
Cu^2	-194,3	-194,3	
Copper (Cu)	83,9	83,9	

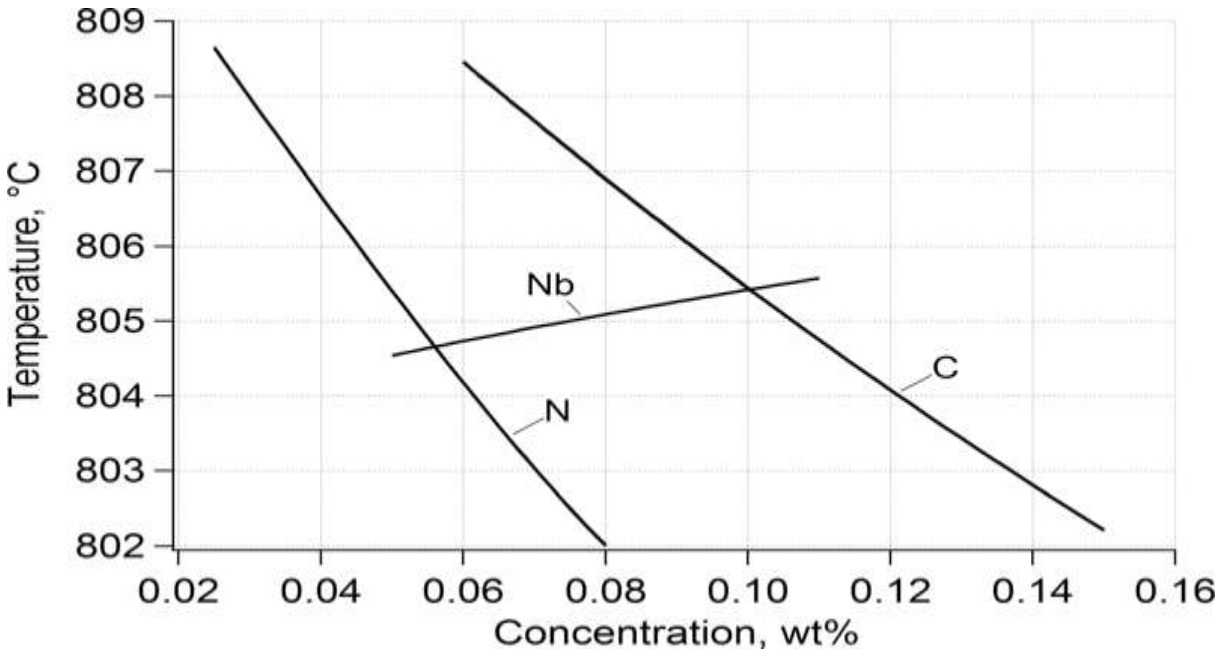

Figure 2.14: Variation in the A_1 of midrange grade 91 compositions of C, N, and Nb [39].

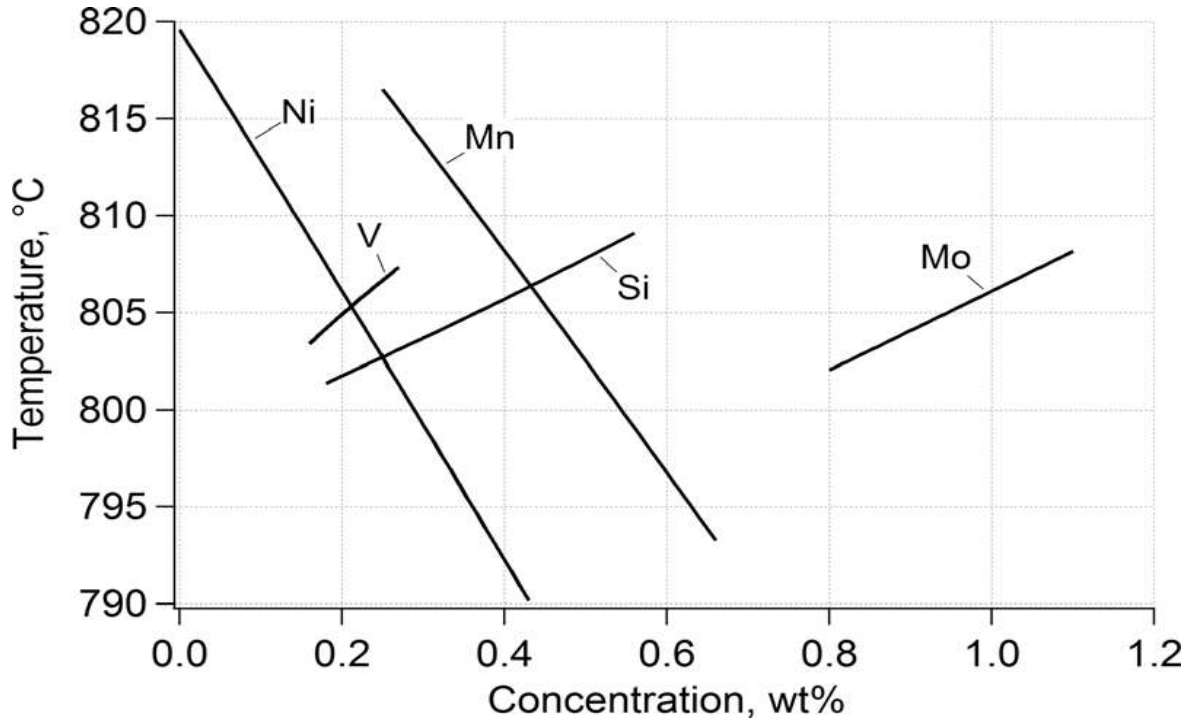

Figure 2.15: Variations of the A_1 of midrange grade 91 compositions of Ni, V, Mn, Si and Mo [39].

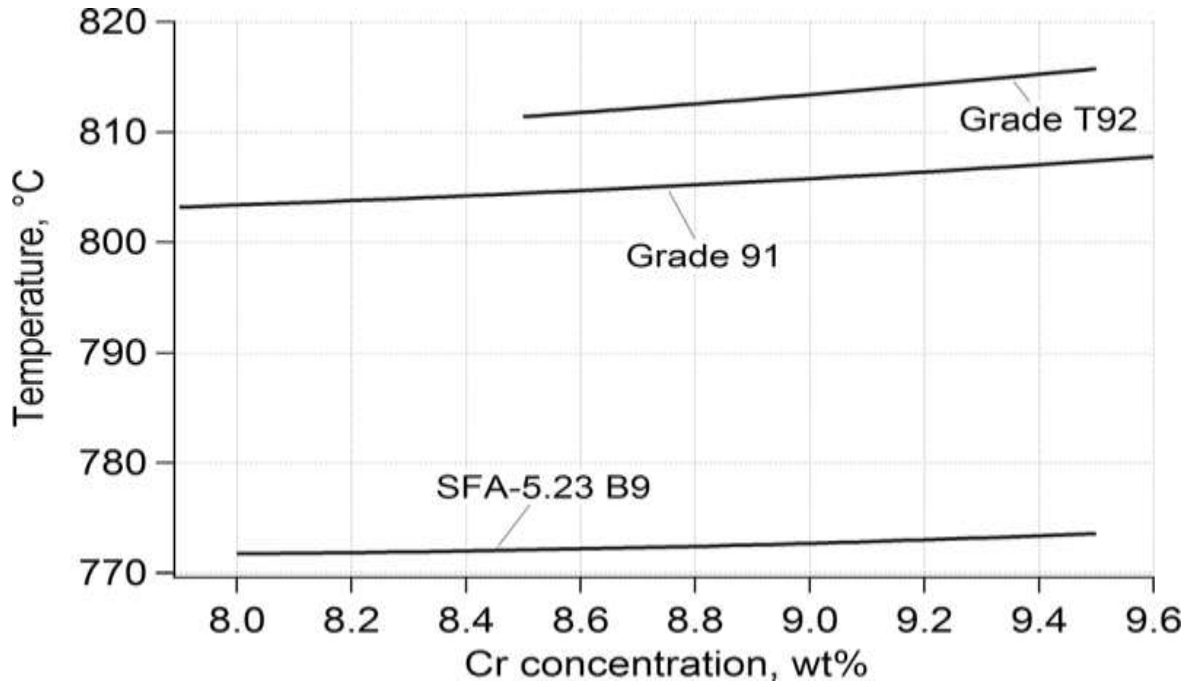

Figure 2.16: Variations of the A_1 with Cr concentrations for midrange compositions of grade 91 [39].

2.8.4 A_{c2} / A_2 temperature

The A_{c2} /A_2 temperature is defined as a change in material state from ferromagnetic to paramagnetic during heating. A transition of two peaks was reported by Lun Wang in P91 steels using single sensor differential analysis and thermodynamics software on the base metal during the heating cycle [40]. The first peak and the second peak were slightly above 750 and 800ºC respectively (Figure 2.17). The first peak represents changes in ferromagnetic to paramagnetic transformation (Curie temperature, A_2) and the second peak is the austenitization process [40]. The austenitization process is represented by the start of austenite transformation (A_1) and the end of austenite transformation (A_3). Shrestha et al. also detected the A_2 Curie temperature during their study and reported it as changes in ferromagnetic properties at 741ºC [24].

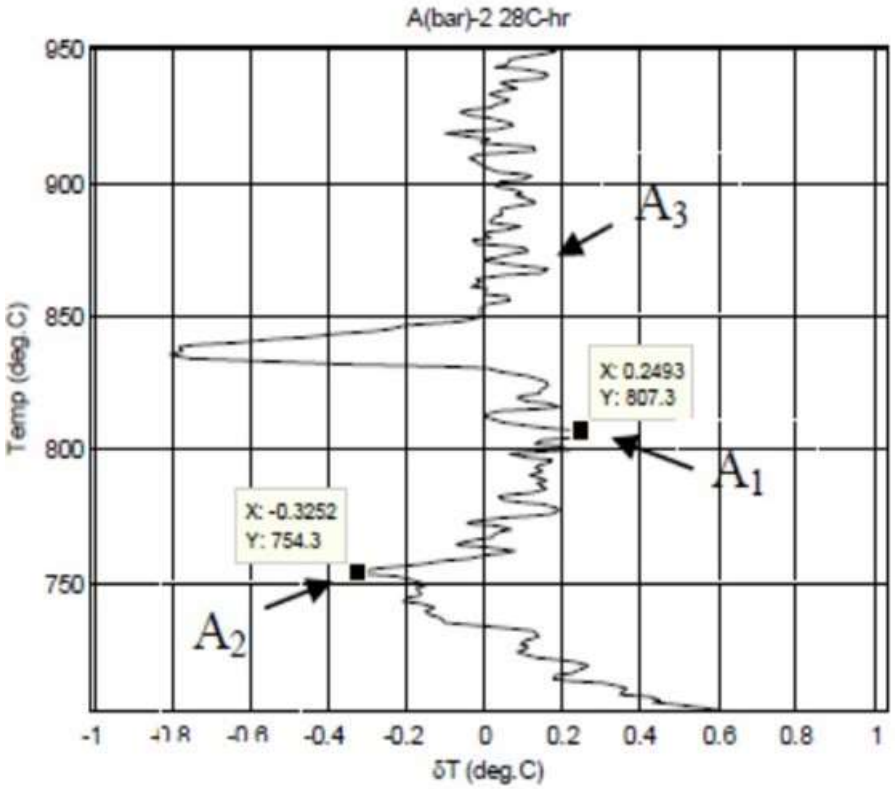

Figure 2.17: A_2, A_1, and A_3 in a laboratory melted heat of P91 steel determine by SS-DTA [40].

2.8.5 M_s and M_f temperatures

When grade P91 is cooled from temperatures where the steel is fully austenitic, it passes through two more critical temperatures, namely martensite start (M_s) and martensite finish (M_f). The martensite start temperature (M_s), is defined as the highest temperature where austenite starts to transform to martensite during cooling. Untempered martensite can also occur when the grade P91 is heated above the A_{c1} temperature and is not cooled low enough to completely transform the austenite to martensite, where some retained austenite could remain in the microstructure. The untempered martensite could be detrimental to material properties. Nitsche and Mayr [38] in their study reported the M_s temperatures as follows: under equilibrium conditions, ranging from 362 to 427ºC and between 349 and 406ºC when simulating welding conditions. They reported the M_f temperatures to be as follows: under equilibrium conditions, from 204 to 311ºC and between 197 to 336ºC when simulating welding conditions. The average M_s temperature under equilibrium and welding

conditions was 385 and 380ºC respectively. The average M_f temperature was 243ºC under equilibrium conditions and 248ºC when simulating welding conditions. Silwal et al. found the M_s temperature of 394ºC on the grade P91 weld sample (welded with GTAW and FCAW) [41]. Several authors have used multiple linear regression equations to summarise the influence of alloying elements on the martensite start temperature as shown by predictive equations in Table 2.7 [40, 42]. Some of the M_s formulae coefficients for certain elements presented by Wang l40] are different to those presented by Cheng et al. [42] as shown in Table 2.7. The applicable composition range of the formulae for M_s in Table 2.7 are shown in Table 2.8 [40]. It should be noted that only the Zhao formula is applicable to P91 steels.

Table 2.7: Predictive formulas for estimating M_s temperatures [40, 42].

No.	Source	Year	Equation
1.	Payson and Savage	1944	M_s (ºC) = 498.9 – 316.7C -33.3Mn -27.8Cr-16.7Ni-11.1Si – 11.1Mo-11.1W (+10Co) [40] M_s (ºC) = 499 – 308C -32.4Mn -27Cr-16.2Ni-10.8Si – 10.8Mo-10.8W [42]
2.	Rowland and Lyle	1946	M_s (ºC) = 498.9 – 333.3C -33.3Mn -27.8Cr-16.7Ni-11.1Si - 11.1Mo-11.1W (+10Co) [40] M_s (ºC) = 499 – 324C -32.4Mn -27Cr-16.2Ni-10.8Si - 10.8Mo-10.8W [42]
3.	Grange and Steward	1946	M_s (ºC) = 537.8 – 361.1C -38.9(Mn+Cr)-19.4Ni-27.8Mo (+10Co) [40] M_s (ºC) = 538 – 350C -37.7(Mn+Cr)-18.9Ni-27Mo [42]
4.	Nehrenberg	1946	M_s (ºC) = 498.9 – 300C -33.3Mn -22.2Cr-16.7Ni-11.1Si - 11.1Mo (+10Co) [40] M_s (ºC) = 499 – 292C -32.4Mn -22Cr-16.2Ni-10.8Si - 10.8Mo [42]
5.	Steven and Haynes	1956	M_s (ºC) = 561.1 – 473.9C -33.3Mn -16.7(Cr+Ni) – 21.1Mo (+10Co) [40] M_s (ºC) = 561 – 474C -33Mn -17Cr-17Ni - 21Mo [42]
6.	Andrew	1965	M_s (ºC) = 539 – 423C -30.4Mn -12.1Cr-17.7Ni- 7.5Mo (+10Co) (linear) [40, 42]
	Andrew	1965	M_s (ºC) = 512 – 453C -16.9Ni -9.5Mo + 217$(C)^2$- 71.5(C)(Mn) +15Cr-67.6(C)(Cr) (+10Co) (nonlinear) [40, 42]

Table 2.7: Continued

7.	Zhao	1992	M_s^{TM} (ºC) = 420 – 208.33C – 72.65N – 43.46N^2- 16.08Ni + 0.7817Ni^2- 0.02464Ni^3 – 2.473Cr-33.428Mn + 1.296Mn^2- 0.02167Mn^3 + 30.00Mo + 12.86Co – 0.2654Co^2 + 0.001547Co^3 – 7.18Cu – 16.28Ru + 1.72Ru^2 – 0.08117Ru^{3a} [40, 42]
8.	Zhao	1992	M_s^{LM} (ºC) = 540 – 356.25C – 260.64N – 24.65Ni + 1.36Ni^2- 0.0384Ni^3 – 17.82Cr + 1.42Cr^2 -47.59Mn + 2.25Mn^2- 0.0415Mn^3 + 17.5Mo + 21.87Co – 0.468Co^2 + 0.00296Co^3 – 16.52Cu – 17.66Ru^b [40, 42]

[a] M_s temperature for twinned martensite (TM)

[b] M_s temperature for Lath martensite (LM)

Table 2.8: Applicable composition range of formulae for M_s [40].

Elements (wt.%)	Payson and Savage (1944)	Rowland and Lyle (1946)	Grange and Steward (1946)	Nehrenberg (1946)	Steven and Haynes (1956)	Andrew (1965)	Zhao (1992)
Carbon	<1.0	<1.0	<0.9	0.17-1.28	0.10-0.55	0.11-0.60	<2.0
Manganese	1.02-4.87	0.45-0.82	<7.0	0.29-1.21	0.20-1.70	0.04-4.87	<27
Silicon	<1.0	0.21-0.31	-	0.15-1.89	-	0.110-1.89	-
Chromium	0.98-4.61	0.02-1.50	<1.50	0.05-8.81	<3.50	<4.61	<10
Nickel	1.16-4.83	0.08-3.99	<14.0	0.10-3.41	<5.0	5.04	<34
Molybdenum	1.05-5.40	0.02-0.28	<1.0	0.03-0.33	<1.00	<5.40	<2.5
Tungsten	1.04	-	-	-	-	-	-
Nitrogen	-	-	-	-	-	-	<3
Cobalt	-	-	-	-	-	-	60
Copper	-	-	-	-	-	-	<7
Ruthenium	-	-	-	-	-	-	<20
Applicable to P91 steels	No	No	No	No	No	No	Yes

2.9 Delta (δ) ferrite phase

Delta (δ) ferrite phase formation in grade P91 weld metals has been observed by Merchant and Zhang et al [43, 31]. It has been reported that δ-ferrite in P91 steel welds forms in areas exposed to peak temperatures above 1200ºC. The presence of a large quantity of δ-ferrite phase has been reported to have an adverse effect on the toughness and creep resistance of P91 steel. The possibility of δ-ferrite formation can be estimated by the Scheider formula using chromium (Cr_{eq}) and nickel equivalents (Ni_{eq}) to calculate the ferrite factor (FF) as shown by the equations below [43]. Merchant reported in his study that a fully martensitic microstructure without δ-ferrite retention is obtained when the Cr_{eq} is more than 13.5 and the difference between the Cr_{eq} and Ni_{eq} is less than 8 (ferrite factor). Zhang et al. reported in their study that no δ-ferrite retention for weld and base metals with compositions giving a ferrite factor less than six.

$$\mathbf{Cr_{eq} = Cr + 2Si + 1.5Mo + 5V + 1.75Nb + 0.75W} \quad \mathbf{(2.11)}$$

$$\mathbf{Ni_{eq} = Ni + 0.5Mn + 30C + 25N + 0.3Cu} \quad \mathbf{(2.12)}$$

$$\mathbf{FF = Cr_{eq} - Ni_{eq}} \quad \mathbf{(2.13)}$$

2.10 Post weld heat treatment (PWHT)

Post weld heat treatment (PWHT) is a stress relieving treatment performed at a temperature below the austenite transformation temperature (A_{c1}). Residual stresses are in order of the yield strength, especially in the welds of thick sections and when combined with the load stresses, may exceed the design stresses which may lead to failure of a component during service [44].

It is important that the lower critical temperature for martensite-to-austenite transformation, A_{c1}, is not exceeded during PWHT. When the A_{c1} temperature is exceeded, the newly formed austenite will partially or completely transform to martensite on cooling from PWHT temperature with the final microstructure comprising

un-tempered martensite or alpha ferrite. Peng et al. in their study reported two factors that significantly change the microstructure of P91 welds [45]:

- When the peak temperature exceeds the A_{c1} temperature during PWHT and
- The slow cooling rate during PWHT, the cooling curve could pass through the ferrite nose and the unstable austenite would transform to α-ferrite and not to martensite. It's important to note that when P91 base material and weld metal are exposed to the temperatures range between 400-500ºC for a very long time there is a risk of temper embrittlement [4]. Temper embrittlement is caused by trace elements such as phosphorus, antimony, tin and arsenic that migrates to the grain boundaries and can reduce ductility in both the base material and weld metal.

Alexandrov et al. reported in their research work the formation of α-ferrite during the PWHT process after exceeding the A_{c1} temperature [36]. Santella et al. in their study showed the effect of homogenization heat treatment on the A_{c1} temperature to indicate that microsegregation exists in the weld metal [37].

Generally, P91 steels are resistant to tempering, with high PWHT temperatures needed to reduce hardness and to develop the required toughness in the weld metal [36]. It is critical that alloy additions in P91 welding consumables should be controlled so that the A_{c1} transition temperature of the weld metal is sufficiently low for optimum tempering, but high enough to avoid re-austenitization and formation of ferrite during PWHT (i.e. elements that lower the A_{c1} temperature, notably Ni and Mn, should be controlled to avoid formation of fresh martensite during PWHT) [31, 37, 41]. The formation of untempered martensite and ferrite is detrimental to the toughness and the creep resistance of the P91 steel. The AWS SFA 5.5 E9018-B9 PWHT requirements together with the Thermanit SMAW consumable PWHT testing parameters, are shown in Table 2.9. The influence of hardness on the PWHT conditions (i.e. temperature and time) for SMAW with Thermanit SMAW consumable, is shown graphically in Figure 2.18 [46]. It is shown that the hardness decreases with an increase in PWHT temperature and time. The ASTM A335 /A335M grade T/P 91 hardness standard requirements after PWHT is 196 to 265 HV. A hardness above 300HV after PWHT indicates the presence of hard brittle untempered martensite and softer ferrite below 190HV.

Table 2.9: Thermanit welding consumable [46] and AWS SFA 5.5 E9018-B9 [47] PWHT requirements.

No.	PWHT cycle	AWS SFA 5.5 E9018-B9	Thermanit Chromo 9V
1.	Heating rate Temperature	85-280ºC/h RT to 760ºC	80-120ºC/h RT to 760ºC
2.	Soaking temperature Soaking time	760ºC 2 hours	760ºC 2-4 hours
3.	Cooling rate Temperature range	<200ºC/h 760ºC to RT	100-150ºC/h 760 -400ºC
4.	Cooling	-	<400ºC Still air

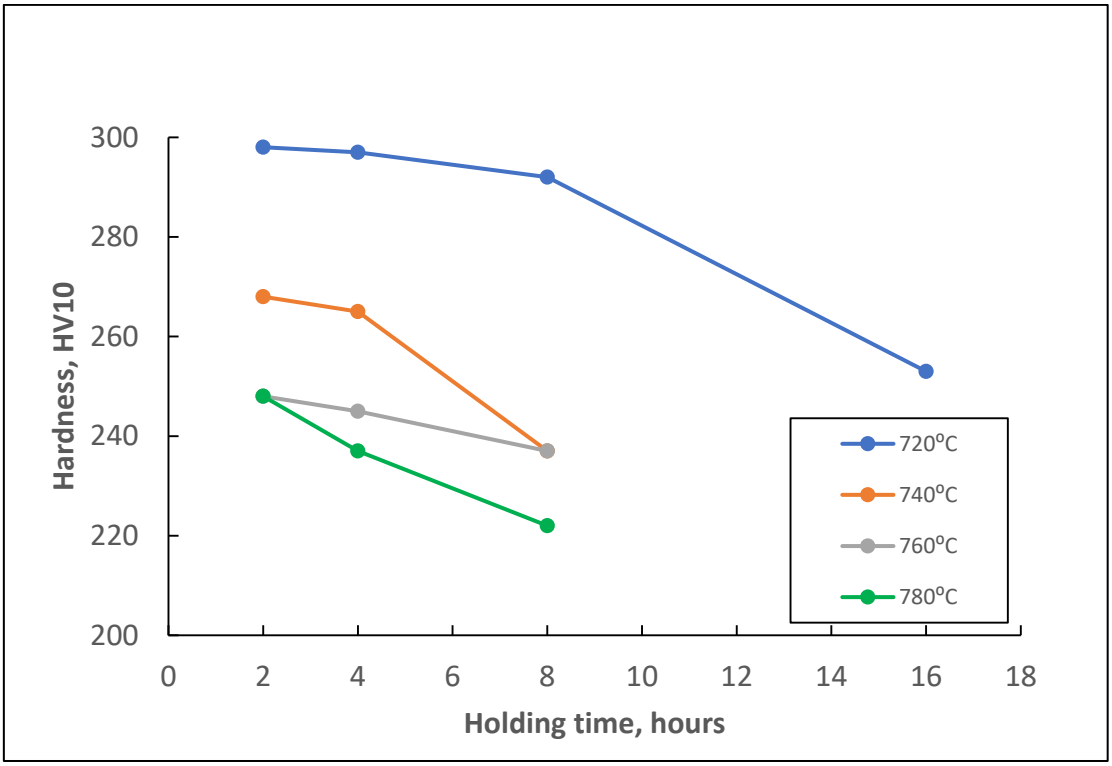

Figure 2.18: Influence of the PWHT conditions (temperature and time) on hardness for 9Cr SMAW metal [46].

2.11 Summary of findings for A_{c1}, A_{c3} and M_s temperature

Alexandrov et al. used single sensor dilatometry SS-DTA and “design of experiment” (DOE) techniques to determine the A_{c1} temperatures of weld metals (GMAW, SAW) and base metals on more than 70 grade P91 samples. This study found the A_{c1} temperatures of the weld metals in the range between 770–801ºC and that of the base metal to be 788 to 813ºC. A predictive equation for the A_1 temperature was developed as shown in equation 2.8. The predictive equation was revised (equation 2.9) in this study with changes in a constant and coefficients of Cr, Mo, and V as shown in Table 2.7. The M_s temperature of the SAW weld metal was found to be 470ºC.

Santella reported the A_{c1} temperatures of the two SAW weld samples to be 780 and 800ºC, determined after homogenising and PWHT of the individual sample. A predictive equation for the A_1 temperature of grade P91 was also developed by Santella using computational thermodynamics (Thermocalc^{TM}) and “design of experiments” techniques. The predicted range for A_1 temperatures grade P91 were 766 to 856ºC for the base metal and 676 to 862ºC for the weld metal.

These predictive equations were different, however in both the revised Alexandrov et al. (equation 2.9) and Santella (equation 2.10) equations that show that the austenite (Ni, Mn, C, N, Cu) and ferrite (Cr, Si, Mo) stabilising elements in the chemical composition of grade P91 are well represented (Table 2.7). Both these studies revealed that the lower critical temperature is not only controlled by the Mn + Ni content, but that other elements also contribute.

Nitsche and Mayr [38] used two different techniques (DTA and SS-DTA) to determine the A_{c1}, A_{c3} and M_s transformation temperatures on grade P91 base metal. The A_{c1} temperatures ranged between 768 to 825ºC at a rate of 28ºC/h (equilibrium condition). Scattered and high A_{c1} temperatures were found when simulating welding conditions compared to an equilibrium condition. The A_{c3} temperature results were scattered in both these conditions; for an equilibrium condition, it ranged between 828 to 924ºC and 904 to 1064ºC for a welding condition. The M_s and M_f temperatures results were scattered in both for equilibrium and welding conditions. The large range in the A_{c1} measured under equilibrium conditions was not explained.

CHAPTER 3: EXPERIMENTAL PROCEDURE

3.1 Overview

This chapter presents the experimental work performed on the P91 welding electrodes and base material. An experimental matrix of the experimental laboratory electrodes, commercial electrodes, and base material are shown in Table 3.1. Laboratory developed experimental electrodes were selected based on their weldability report and electrodes with severe eccentricity could not be characterised. Please take note that the flux formulations of the experimental electrodes are not revealed in the present study. However, these experimental electrodes are developed according to AWS SFA 5.5 9018-B9 Potassium- Iron powder flux formulation, with the following objectives in mind:

- The objective was to develop a welding electrode conforming to the AWS SFA 5.5 9018-B9 chemical composition.
- The deposited weld metals chemical composition should also be close to that of the ASME SA 335 P91 base material (which is equivalent to ASTM A335 P91) requirements (Tables 3.2 and 3.3).
- The target for the A_{c1} transformation temperature of the developed welding electrode was 20ºC above the PWHT temperature for AWS SFA 5.5 9018-B9 specification, that is, 760±15ºC. Therefore, the A_{c1} temperature should be 780ºC as a minimum.
- The hardness of the weld metal was aimed at ASME SA 335 P91's base material requirements after PWHT (see Table 3.4).

The AWS SFA 5.5 9018-B9 chemical composition specification of the welding electrode (weld metal) is usually highly alloyed compared to that of ASME SA335 P91 base metal (Table 3.2). The sum of the nickel and manganese content of the ASME SA335 P91 base metal is below 1 wt.% and that of the AWS 5.5 E9018-B9 electrode between 1 and 1.5 wt.%. As covered in section 2.8.2, these two elements have a major influence on the A_{c1} transformation temperature. Mechanical properties of the AWS SFA 5.5 E9018-B9 electrode and ASME SA335 P91 base metal specifications are shown in Table 3.3, with the strength of the weld metal typically higher than that of the base metal and the minimum specific ductility slightly lower. In the current study,

the experimental electrodes were evaluated against the chemical composition requirements, as noted for AWS SFA 5.5 E 9018-B9. Apart from the hardness, the mechanical properties were not evaluated. The transverse cross-sections of the weld samples and base metal in the as-welded / as-received condition and after post weld heat treatment were characterised. The weld deposit for characterisation of the microstructure, dilatometry, PWHT and hardness were selected based on weldability performance and chemical composition. However, it should be noted that one or more laboratory developed electrodes from each phase was characterised in this study.

Table 3.1: Experimental matrix

Phase	Electrode ID	Weldability	Chemical Composition	Microstructure	Dilatometry	PWHT	Hardness
1	**LAB 74**	1	1	0	0	0	0
	LAB 75	1	1	0	0	0	0
	LAB 76	1	1	1	1	1	1
	LAB 77	1	1	0	0	0	0
	LAB 78	1	1	0	0	0	0
	LAB 79	1	1	0	0	0	0
2	**LAB 99**	1	1	1	1	1	1
	LAB 100	1	1	0	0	0	0
	LAB 101	1	1	1	1	1	1
	LAB 102	1	1	0	0	0	0
	LAB 103	1	1	0	0	0	0
	LAB 104	1	1	0	0	0	0
	LAB 105	1	1	0	0	0	0

Table 3.1: Continued

Phase	Electrode ID	Weldability	Chemical Composition	Microstructure	Dilatometry	PWHT	Hardness
3	**LAB 150**	1	1	1	1	1	1
	LAB 151	1	1	0	0	0	0
	LAB 152	1	1	0	0	0	0
	LAB 153	1	1	1	1	1	1
	LAB 154	1	1	1	1	1	1
	LAB 155	1	1	1	1	1	1
4	**LAB 168**	1	1	0	0	0	0
	LAB 169	1	1	1	1	1	1
	LAB 170	1	1	0	0	0	0
	LAB 171	1	1	1	1	1	1
	LAB 172	1	1	1	1	1	1
	LAB 173	1	1	0	0	0	0
	LAB 174	1	1	0	0	0	0
5	**LAB 19**	1	1	1	1	1	1
	LAB 20	1	1	1	1	1	1
	LAB 21	1	1	1	1	1	1
	LAB 22	1	1	0	0	0	0
	LAB 23	1	1	1	0	1	1
	LAB 24	1	1	1	1	1	1
Commercial	**1**	1	1	1	1	1	1
	2	1	1	1	1	1	1
	3	1	1	1	1	1	1
Base metal	**P91**	0	1	1	1	1	1

1 Test performed

0 Test not performed

Table 3.2: Chemical compositions of the ASME SA335 P91 and AWS SFA 5.5 9018-B9 welding consumable specifications [32,47].

Element (wt%.)	C	Mn	Si	S	P	Ni	Cr
Base metal	0.08 - 0.12	0.3-0.6	0.2-0.5	0.01	0.02	0.40	8.0-9.5
Weld metal	0.08-0.13	1.20	0.30	0.01	0.01	0.80	8.0-10.5

Element (wt%.)	Mo	V	Al	Nb	N	Ti
Base metal	0.85-1.05	0.18-0.25	0.02	0.06-0.10	0.03-0.07	0.01
Weld metal	0.85-1.20	0.15-0.30	0.04	0.02-0.10	0.02-0.07	-

Table 3.3: Mechanical properties, as noted in the ASME A335 P91 and AWS SFA 5.5 9018-B9 specifications [32, 47].

Material	ASME SA335 P91	AWS SFA 5.5 E 9018-B9
Tensile strength (MPa) min	585	620
Yield strength (MPa) min	415	530
Elongation (%) min	20	17
Hardness (HV) max	196 - 265	not specified
Heat Treatment Condition	**Normalised & Tempered**	**PWHT Condition**
Temperature (ºC)	1040 to 1080 & 730 to 800	760 ±15
Heating rate (ºC/h)	not specified	85 to 280
Soaking temperature and time	not specified	760 for 2hrs
Cooling rate (ºC/h)	not specified	<200

3.2 Design of P91 electrodes

3.2.1 Overview

P91 SMAW electrodes are normally designed using a carbon steel / unalloyed core wire with alloying from the flux. The developed SMAW electrodes and three commercial SMAW electrodes used for benchmarking also had a mild steel core wire.

3.2.2 Mild steel core wire

The mild steel core wire used for the electrode development was received from the supplier as a coiled rod with a diameter of 5.5 mm, with the typical composition shown in Table 3.4. The core wire was aged for three weeks to transform the mill scale (magnetite) on the surface to rust (hematite). After aging, the coil was subjected to a drawing, straightening and cutting operation to the diameter of 4.00 mm and cut to 350 mm lengths.

Table 3.4: Typical chemical composition of the mild steel core wire [48].

C	Mn	Si	S	P	Ni	Cr	Mo
0,05-0,09	0,4-0,6	0.10	0.015	0.012	0,06	0,04	0,02

V	Al	Cu	Ti	N
0,08	0,01	0,04	0.005	0,008

Note: single values on the table are maximum

3.2.3 Experimental flux formulation

The flux formulation was prepared manually by weighing raw materials shown in Table 2.1. For consistency, raw materials (including core wire) were selected from one batch of each respective material. The particle size of each raw material was tested and found to conform to the standard requirements with sizes ranging from 300 to 75 microns. After weighing, the raw materials were mixed together with the total quantity of approximately 1.4 kg. The mixed raw materials were then dry blended for 20 minutes in a laboratory mixer (Figure 3.1).

3.2.4 Wet mixing solution

Wet mixing solutions were prepared by adding potassium silicate, sodium silicate, and lithium hydroxide. The temperature of the mixing solution was kept at room temperature. The wet mixing solution was kept the same for the entire project.

3.2.5 Extrusion and drying

The wet mixing solution was added slowly to the dry flux formulation in the laboratory mixer and stirred for 15 minutes. The paste-pressure was adjusted between 6-10 MPa by slowly adding the liquid solution in dry flux before extrusion. The paste pressure was measured on the hydraulic pressure testing machine.

A manually operated laboratory extrusion machine was used. The core wires were placed in the wire feeder unit as indicated by the black arrow in Figure 3.2. Wet flux formulation (paste) was put in the die assembly unit for extrusion. The die size used for manufacturing the electrodes was between 6.50 to 6.55 mm. An eccentricity meter was used to ensure that concentric electrodes were produced. Eccentricity is defined as a maximum difference in radial coating thicknesses of the electrode (Figure 3.3). If the core wire of a flux-coated electrode is displaced excessively (eccentric) from the flux coating, the arc will be unstable during welding, leading to defects such as porosity and slag inclusions. For control purposes, the electrodes were labelled, then air dried for a minimum of 12 hours before baking.

3.2.6 Baking and moisture

Baking of the electrodes was performed in two stages in static ovens, namely low bake (180ºC) and high bake (460ºC) to remove residual water to the requirement of AWS specification (<0.4wt%). Every bake stage was done for two hours. The two-stage baking process allows the slow removal of water from the flux without cracking.

Two hours after baking, the flux coating's moisture content was measured on a Leco RC 612 moisture instrument. This process consists of breaking the coating on the dry electrode and weighing it. Then the flux coating was put inside the RC 612 heating chamber to remove moisture and weighed afterwards. The electrodes were stored in the humidity room to prevent moisture pickup before welding.

3.3 Phases in the development of experimental electrodes

Formulations were designed in five phases. Every phase involved the formulation of six different recipes. For every formulation, the raw materials were adjusted according to the requirements (i.e. extrudability, weldability, chemical composition). For consistency, the most successful development (i.e. good extrusion, green bond strength, and weldability) was used as a standard in the next phase. Individual formulations were identified by a unique number (example, LAB 75).

Phase 1 (LAB 74-79) was an initial development of the P91 flux formulation which was based on trial and error, hence most of the concentrations of alloying materials added were varied (Table 3.5). Most of the additions raw materials were kept constant (i.e. extrusion agent, binders, slag former and shielding agents) with the adjustment made to alloying materials during this phase.

Most of the raw materials were kept the same with the alloying materials such as ferrochrome, ferro-niobium, ferrovanadium and ferro-silicon varied during experiments in phase 2 (Table 3.5). Raw material adjustments in this phase (LAB 99-104) were based on the analyses of the weld metal's chemical composition and the weldability, as reported by the welder for electrodes produced during phase 1.

Phase 3 developments (LAB 150-155) had as the major focus, weldability characteristics such as slag self-lifting ability and alloying (Table 3.5). LAB 101 from phase 2 was used as a standard in these developments.

Changes made to the formulations in phase 4 developments (LAB 168-174) were similar to the previous phase based on alloying and slag characteristics. LAB 151 was used as the standard in phase 4 developments.

The adjustment in phase 5 developments (LAB 19-24) was based on the chemical composition and weldability in Phase 4 developments (Table 3.5). The focus of developments was shielding, slag self-lifting characteristics and to reduce the silicon content of the weld deposit. LAB 168 from phase 4 was used as a standard in the formulations in phase 5 development (Table 3.5).

Table 3.5: Summary of phases in the development of P91 SMAW electrodes.

Phase	Electrode identification	Main objective	Actions	Slag characteristics	Alloy content of weld deposit	Most successful development
1	LAB 74 to 79	Achieve proper balance on the extrusion, binding, shielding, deoxidising, alloying agents in the flux.	Additions made in the fluxes were based on trial and error as a starting point to the developments.	Good slag coverage. Splitting and sticky in some developments.	Good recovery of major elements in the weld but Cr, V, Nb were below specification.	LAB 75 was successful and the formulation (LAB 99) used as a standard in phase 2.
2	LAB 99 to 104.	The objective in phase 2 was to improve slag lifting characteristics and alloying	Increased FeCr, FeV, FeNb and TiO_2 and decreased FeSi. Other raw materials kept constant.	Excellent slag coverage. Slag splitting and sticky in some developments.	Recovery was good but Cr still below minimum specification and Nb, Si and V slightly above.	LAB 101 was the better one and used as standard (Development 150) in phase 3.
3	LAB 150 to 155	Phase 3 developments were aimed at improving the slag lifting characteristic and alloying.	Increased FeCr, FeTi and iron powder. The rest of the raw materials were kept constant.	Splitting slag and still sticky in some developments.	Cr recovery still low in developments 150 to 153). Si high and Nb low in all developments.	LAB 151 was best in this phase and use as standard (LAB 168) in the next developments.

Table 3.5: Continued

Phase	Electrode identification	Main objective	Actions	Slag characteristics	Alloying	Most successful development
4	LAB 168 to 173	Phase 4 developments had a similar objective to phase 3.	Increased FeCr, FeTi and iron powder and Si decreased.	Slag sticky in some developments. Cracking/splitting in development 168 and 171.	Cr and Si recoveries were within the requirements.	LAB 168 was the best and used as standard (LAB 19) in the next phase.
5	LAB 19 to 24	Phase 5 developments objective were threefold, namely, improve shielding, enhance slag characteristics and alloying.	Increased $CaCO_3$, FeTi, TiO_2, potassium feldspar and decrease Si.	The improvement was shown in most developments. Sticky slag was still observed in developments 21 and 22.	The recovery of major elements (Cr, Mo, Mn, Ni) was good. Si recovery was also good in the developments	LAB 24 was better than the standard (LAB 19). This development was used for characterisation in the investigation.

Note; LAB 75 / LAB 99 is the same formulation

LAB 101 / LAB 150 is the same formulation

LAB 151 / LAB 168 is the same formulation

LAB 168 / LAB 19 is the same formulation

Figure 3.1: Laboratory mixer.

Figure 3.2: Laboratory extruder. Arrow indicates a wire feeder unit.

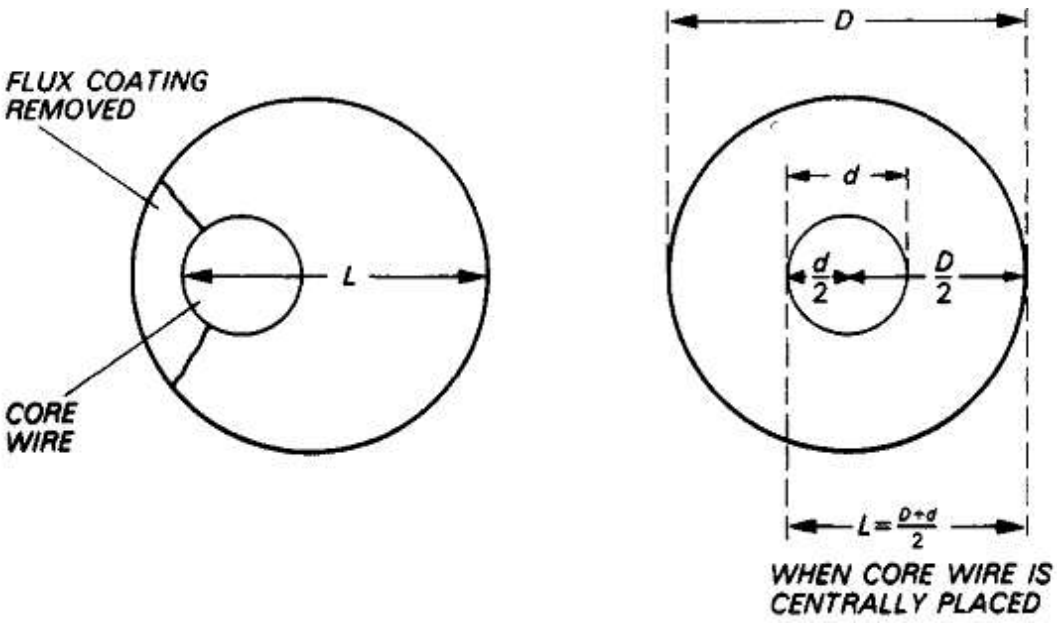

Figure 3.3: Schematic diagram of an eccentric core wire [49].

3.4 Weldability

Weldability is a qualitative test based on the following welding characteristics: electrode strike and re-strike, arc stability, metal transfer, spatter volume, wetting action, metal flow, weld pool explosion, bead appearance, electrode overheating, penetration, weld defects, slag removal, secondary slag, and slag coverage. These welding characteristics are given a rating as follows;

- rated 1 - indicating poor weldability (gross defect)
- rated 2 – indicating moderate weldability (non-conformance defect)
- rated 3 – indicating marginal improvement in weldability required
- rated 4 – indicating satisfactory weldability (full conformity)
- rated 5 – indicating good weldability (optimum performance)

Bead-on-plate weldability tests were performed on a 20X100X130 mm mild steel plate. The deposited weld runs were characterised during and after the welding process. During the weldability tests, fifteen laboratory developed electrodes were compared to three commercially available electrode(s) using the welding characteristics shown in the table below. The parameters used for weldability tests were guided by the AWS SFA 5.5 and the welding manufacturer’s specifications (Table 3.6).

Table 3.6: Welding parameters [47].

Electrode ID	Diameter (mm)	Pre-heat & Interpass temperature (ºC)	Current (amperage)	Polarity
LAB developments	4.0	15 to 150	140 to 200 A	DC+
Commercial 1	3.2	15 to 150	85 to 130 A	DC+
Commercial 2	4.0	15 to 150	130 to 200 A	DC+
Commercial 3	3.2	15 to 150	100-145 A	DC+

3.5 Chemical analyses

Chemical analyses were performed on the undiluted weld metal prepared by depositing a minimum weld thickness of 8 mm (approximately four layers) as required by the AWS SFA 5.5E9018-B9 specification on the 20 mm mild steel plate. The weld pad was deposited using a SMAW Lincoln S350 Power wave machine according to AWS SFA 5.5 specification (see Figure 3.4). The pre-heat temperature was above 15ºC and the inter-pass temperatures were maintained between 15 to 150ºC for all deposited layers. The chemical analysis was performed on the last deposited weld metal using a spark emission spectrometer. Three different areas were analysed: on the ground weld metal surface and an average reading was recorded.

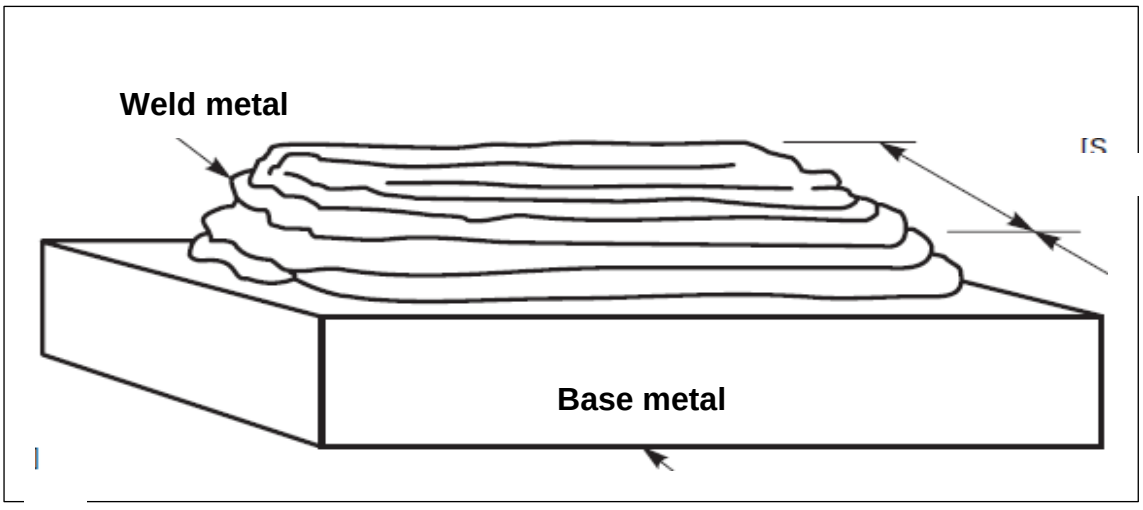

Figure 3.4: Weld metal pad for chemical analysis [47].

3.6 Dilatometry analysis (DA)

3.6.1 Preparation of dilatometry samples

The dilatometry samples were prepared by depositing more layers (approximately 10 layers) on chemically analysed samples for a minimum weld thickness of 20 mm, as shown in Figure 3.5. The pre-heat and interpass temperatures were also maintained between 15 and 150ºC. Cylindrical and rectangular samples with the approximate of 5x10 mm dimensions were sectioned from the undiluted weld metal and base material in the transversal position (perpendicular to the welding direction).

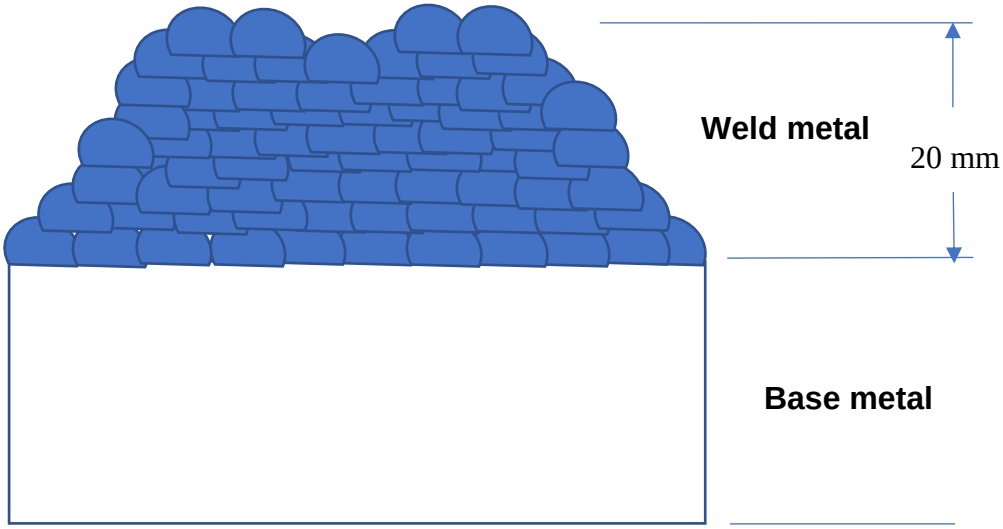

Figure 3.5: Weld metal pad for dilatometry analysis.

3.6.2 Dilatometry simulated tests

The phase transformation temperatures were determined on fifteen laboratory developed electrodes, three commercial electrodes, and the base material. A Bähr dilatometer (DIL805D) was utilized to analyse the A_{c1}, A_{c3} and M_s temperatures during slow heating (simulation of equilibrium conditions), fast heating (simulation of welding conditions) and PWHT simulation (Table 3.7). The A_{c1}, $A_{c3,}$ and M_s transformation temperatures were quantified during dilatometry using the lever rule by drawing the tangents as illustrated in Figure 3.6. The transformation temperature is determined at a point where the measured data deviates from the tangent. A PWHT simulation test was also performed in the Lenton furnace. The standard dilatometry sample was put into the vacuum induction heating chamber during testing. During slow heating, according to ASTM 1033-4 [35], the sample was heated from room temperature to 700ºC at 10ºC/sec followed by 28ºC/h from 700 to 1000ºC. This was then followed by cooling rapidly assisted with helium gas at 10ºC/sec from 1000ºC to room temperature. Fast heating was performed at 100ºC/sec from room temperature to 1300ºC and holding the sample at temperature for 10 seconds before cooling at 20ºC/sec to room temperature. The PWHT simulation test was performed at 180ºC/h from room temperature to 760ºC and holding for two hours at temperature before cooling to room temperature at the same rate.

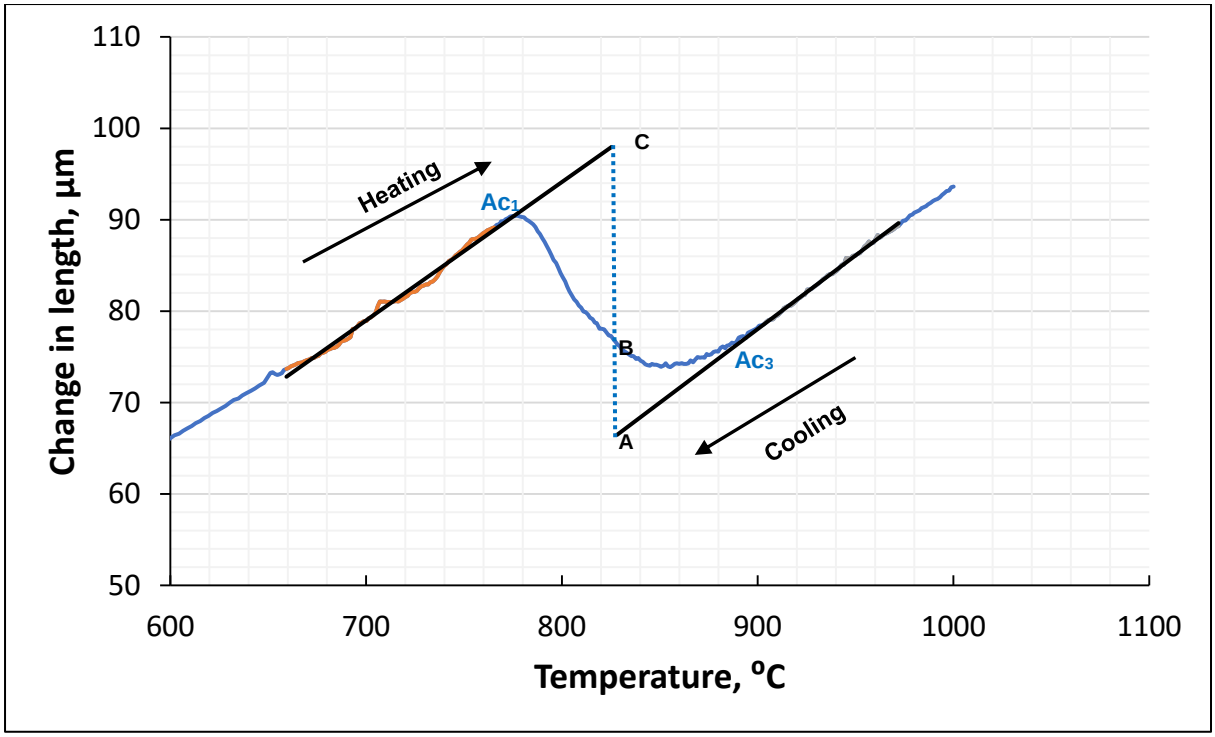

Figure 3.6: Dilatometry curve for Commercial 3 weld metal illustrating the lever rule by drawing tangents when determining the A_{c1} and A_{c3} temperatures.

Table 3.7: Slow heating [35] and PWHT simulated cycles [47].

No.	Cycles	Slow heating	PWHT
1.	Heating rate Temperature (ºC)	10ºC/sec RT to 700	180ºC/h RT to 760
2.	Heating rate Temperature (ºC)	28ºC/h 700 to 1000	-
3.	Soaking temperature (ºC) Soaking time (hrs)	-	760 2
4.	Cooling rate Temperature (ºC)	10ºC/sec 1000 to RT	180ºC/h 760 to RT

3.7 Microstructural analysis

Characterisation of the microstructures of the welds and base metals were performed using optical and scanning electron microscopy.

3.7.1 Optical microscopy

The samples were prepared by standard laboratory methods on transverse sections. The samples were hot mounted in bakelite resin using an Opal 410 mounting press. Grinding was performed manually using silicon carbide from 180 to 1200 grit papers (according to equivalent grit guide 78 to 6.5 µm), followed by fine polishing with 6µm, 3 µm, and 1 µm. Etching of as-welded, base material, dilatometry slow heating and PWHT samples were done using Vilella's (100ml ethanol, 5ml HCl and 1g Picral acid). According to Vandervoort [50], this etchant reveals ferrite and carbides and seldom outlines prior austenite grain boundaries. Etched samples were examined on an Olympus BX 51M optical microscope.

3.7.2 Scanning Electrode Microscopy (SEM)

The etched surfaces in the as-welded, base material, A_{c1} (dilatometry slow heating) and PWHT samples were examined by the Joel JSM IT300LV scanning electrode microscope attached with semi-quantitative Energy Dispersive X-ray spectroscopy (EDX) using the secondary electron image mode.

3.7.3 Ferrite phase analysis

Ferrite phase analysis was performed on weld samples using the Scheider formula and manual analysis.

The Scheider formula was used to calculate the chromium equivalent (Cr_{eq}) and nickel equivalent (Ni_{eq}) to determine the ferrite factor (FF) of the weld samples (see, equation 2.11 to 2.13) [43].

Manual analysis was also conducted on LAB 169 PWHT, LAB 172 PWHT, commercial 1 (as-welded and PWHT) and commercial 2 (as-welded) weld samples by 100 points test grid in the form of a transparency superimposed on the micrograph

randomly to avoid any bias. The volume fraction of ferrite on the manual point counted weld samples was calculated using equations 3.1 to 3.3 [51];

$$\mathbf{P_p(\alpha) = P_\alpha / P_T} \quad \textbf{(3.1)}$$

P_p = Estimated volume fraction α

P_T = total numbers of points counted

P_α = number of points in α

$$\mathbf{\sigma(P_p) = P_p / \sqrt{P_\alpha}} \quad \textbf{(3.2)}$$

$\sigma(P_p)$ = standard deviation

$$\mathbf{95\%\ CI = 1.96\ X\ \sigma(P_p)} \quad \textbf{(3.3)}$$

95% CI = 95 % confidence interval

3.8 Vickers Hardness

Vickers hardness measurements were performed on the transversal samples of the as-welded, base material, dilatometry slow heating and PWHT samples. The hardness measurements were done with a 300g load on the FM-700 micro-hardness tester with the dwell time of 15 seconds. A minimum of 7 indentations were taken across the surface of the sample.

CHAPTER 4: RESULTS

4.1 Overview

This chapter presents the results of the investigation of the laboratory developed electrodes, three commercial electrodes, and base metal. The base and weld metals were characterised using optical and scanning electron microscopy in three conditions, namely as-received, dilatometry slow heating and post weld heat treatment (PWHT). The reason for characterisation of the base material in the as-received and after post weld heat treatment was to ascertain that the base metal microstructure after PWHT was similar to that of the weld metal.

- Weldability evaluation of developed electrodes (section 4.2).
- Chemical analyses (Section 4.3).
- Evaluation of measured (A_{c1}) and predicted (A_1) transformation temperatures of the P91 welds and base material (section 4.4).
- Influence of the sum of Ni + Mn content on the A_{c1} transformation temperatures (section 4.5).
- Martensite start (M_s) temperatures (section 4.5)
- Evaluation of post weld heat treatments (section 4.6)
- Microstructural analyses in the as-welded / as-received and after post weld heat treatment using optical and scanning electron microscopy (section 4.6).
- Delta ferrite content (section 4.8).
- Vickers hardness analyses in the as-welded / as-received conditions and after post weld heat treatment (section 4.9).

4.2 Weldability evaluations of developed electrodes

The qualitative weldability results of the laboratory developed electrodes together with the three commercial electrodes are shown in the weldability report in Appendix A.

4.2.1 Phase 1

Some of the electrodes formulated during phase 1 development had marginal weldability, according to the artisan welders. LAB 74, 76, 77 and 78 electrode formulations displayed poor weldability with a sticky slag formed on the weld metal which was difficult to remove. However, the LAB 75 electrode formulation showed better welding characteristics compared to the other formulations in phase 1 development. The slag was not self-lifting but was splitting and easy to detach from the weld metal.

4.2.2 Phase 2

Improvement was shown in phase 2 developments compared to phase 1. The weldability of LAB 99, 100, 101 and 102 electrode formulations were good with slag cracking/splitting together with a tendency to self-lifting. The discolouration was observed on the weld beads indicating that the slag had cracked/split before the weld metal had cooled down. LAB 103 and 104 electrode formulations showed a combination of sticky and splitting slag in different areas (see, Figure 4.1). Weld bead discolouration was also observed in these electrode formulations.

4.2.3 Phase 3

LAB 150 and 151 electrode formulations showed good weldability characteristics with a uniform weld bead and low spatter volumes. The slag in both of these electrode formulations was splitting and with the tendency to self-lifting. LAB 152, 153, 154 and 155 electrode formulation's weldability characteristics were also good with low spatter and sticky slag formed (see, Figure 4.2). However, the weldability was not as good as in the LAB 150 and 151 electrode formulations in phase 3 developments.

4.2.4 Phase 4

LAB 168 electrode formulation showed good weldability characteristics with an even weld bead and low spatter volume. The slag cracked and was easy to remove. Poor weldability with a sticky slag was displayed by the LAB 169 electrode formulation with an even and fine weld bead. The LAB 170 electrode formulation also showed poor weldability with high spatter volume with a tendency to weld pool explosion. The slag was sticky and difficult to remove. Good weldability characteristics were shown by the LAB 171 electrode formulation with slag tendency to self-lifting displayed. The LAB 172 and 173 electrode formulations showed marginal weldability with sticky slag which was difficult to remove.

4.2.5 Phase 5

The LAB 19 electrode formulation displayed good weldability with a low spatter volume, easy to remove slag which was cracking /splitting throughout the weld bead. Similar weldability characteristics to the LAB 19 electrode formulation was shown by the LAB 20 electrode formulation. However, the slag cracking characteristics in LAB 20 electrode formulation was different but easy to remove. The weldability characteristics shown by LAB 21's electrode formulation was marginal with low spatter volume, an uneven weld bead and slag not cracking fully. However, the slag was easy to remove from the weld metal. The weldability of the LAB 22, LAB 23 and LAB 24 electrode formulations was good with low spatter volumes, uniform weld beads and easy to remove slag. The weldability characteristics of the LAB 24 electrode formulation was superior to the other two electrode formulations and comparable to the three commercial electrodes (see, Appendix A). The three commercial electrode's slags were self-lifting and the slag in the LAB 24 electrode cracked and split (Figure 4.3).

Some of the laboratory developed electrodes and commercial electrodes were eccentric and it was difficult to control the arc during welding characterisation.

Figure 4.1: Photograph of the LAB 104 bead on plate weldability test showing a combination of sticky (beginning) and splitting slag (centre). The discolouration was visible on the weld bead.

Figure 4.2: Photograph of the LAB the153 bead on plate weldability test showing sticky and difficult to remove slag.

Figure 4.3: Photograph of the LAB 24 bead on plate weldability test showing tendency to self-lifting and splitting slag.

4.3 Chemical analyses

The recovery of the metal from the flux coating to the weld metal was not part of the research scope in this investigation because proper mass balance and analytical techniques (such as energy dispersive X-ray spectrometry, inductively coupled plasma, optical emission spectrometer, and atomic absorption) are required for the calculation of the flux constituents. However, most of the elements in the weld metal were within the requirements of AWS SFA 5.5 E9018-B9's chemical composition specification, especially in phase 4 and 5 developments (see Appendix B).

Chemical analyses of the 30 developed electrodes, three commercial electrodes and the P91 base material along with the ASME SFA5.59018-B9 and ASME SA335 P91 specifications are shown in Appendix B. Elements not conforming to the specification(s) are highlighted in yellow in Table B1. All formulations in phase 1 development showed chromium and vanadium (except for LAB 74) contents lower than the minimum specified limit and silicon slightly above the maximum limit. The niobium and nitrogen contents were within the specification except for LAB 76 (low Nb) and LAB 74 (low N).

The chromium content was slightly higher in the phase 2 developments, however still below specification. The vanadium also increased slightly to above the specification in all of the formulations. The niobium contents of LAB 100 to 104 electrode formulations were slightly above the specification except for the LAB 100 formulation (Nb above the maximum side (0.10wt%) of the specified value).

Phase 3 developments showed an increase in silicon contents above the specification and the chromium improved in LAB 154 and 155 electrode formulations to the AWS SFA 5.5 E9018-B9 chemical composition requirements. However, in the LAB 150, 151 and 153 electrode formulations, the chromium contents were below the specification.

Major improvements in chromium and silicon contents were shown in phase 4 developments with both elements within the specification. However, the niobium and vanadium contents were slightly below the specification in all of the formulations in this phase.

Most of the elements were within the requirements of the specification in the phase 5 developments except for the LAB 22 and 23 electrode formulations which showed higher and lower molybdenum contents respectively.

The phosphorus content in all of the phases was higher (0.018 to 0.034 wt%) than the 0.01wt% maximum specification with sulphur content showing inconsistent results (see Appendix B). Three commercially available electrodes nominally conforming to the requirements of AWS SFA 5.5 9018-B9 were included in this study. Commercial 1 resulted in a weld deposit with the nickel content extremely lower than the specified value (0.8wt%) and the chromium content below the specified requirements (Appendix B). Commercial 2 had a chromium content also below the specification (Appendix B). Commercial 3 conformed to the specification. The chemical composition of the P91 base material was within the requirements of ASME SA335 P91 specification (Appendix B).

4.4 Determination of A_{c1} and A_{c3} transformation temperatures

Fifteen laboratory developed electrodes were selected randomly from each phase to determine the A_{c1} phase transformation temperature. The results of the measured A_{c1} and the predicted A_1 austenite phase transformation temperatures of these laboratory-developed electrodes, as well as the three commercial electrodes and P91 base metal, are shown in Table 4.1. The measured A_{c3} austenite temperatures are also reported in Table 4.1.

Typical dilatometry curves for slow heating of laboratory developed electrodes, commercial electrodes and P91 base metal are illustrated in Figures 4.4 to 4.8. The A_{c1} temperature of the laboratory developed electrodes and two commercial electrodes are below 800ºC. The commercial 1 electrode and the base metal's A_{c1} temperatures were above 800ºC. Peaks were detected in the weld samples between 730 to 760ºC during the heating cycle in their respective dilatometry curves. Figure 4.9 is a close-up view of the dilatometry curve of LAB 150 illustrating how these peaks are formed between 747 to 760ºC before the A_{c1} transformation temperature (792ºC) is reached. These peaks could be due to changes in the material's state and occurred in most of the weld samples. A change during dilatometry from a fast heating rate (10ºC/sec) to a slow heating rate (28ºC/h) at 700ºC and inhomogeneity of the weld metal could have also contributed to the deviation from linear behaviour.

Measured A_{c1} transformation temperatures and predicted A_1 temperatures using the Santella (equation 2.8), the Alexandrov et al. revised (equation 2.9) and the Ngwenya equations (equation 4.1) are presented graphically in Figure 4.11. The measured A_{c3} temperature and the predicted Ngwenya A_3 (equation 4.2) temperatures are also presented in Figure 4.11. It is shown by the regression line, that there is a linear relationship (R^2=0.53) between the measured A_{c1} temperature and the Santella predicted A_1 temperature. The regression line shows no linear relationship (R^2= -3.53) between the measured A_{c1} and the revised Alexandrov et al. predictive A_1 temperature. A linear relationship (R^2=0.73) was observed between the measured A_{c1} and Ngwenya A_1 predictive equation. Generally, the measured A_{c1} austenite transformation temperatures were higher than those predicted by the Santella and Alexandrov et al. revised equations, except for the LAB 171 and 172 developments

with high values obtained by the Alexandrov revised equation. The measured A_{c1} temperatures were very close to the A_1 temperatures predicted by the Ngwenya equation. Generally, the measured A_{c1} transformation temperatures were above those of the AWS 5.5 E9018-B9 PWHT temperature specification (760ºC). However, the A_{c1} temperatures for LAB 23 and 76 developments were very close to those of the PWHT temperature specification (760ºC).

Sample calculations of the influence of ferrite and austenite forming elements to the A_{c1} temperature using the Santella, Alexandrov et al. revised and Ngwenya's predictive equations on the LAB 24 and commercial 1 weld metals, are shown in Tables 4.2 and 4.3. Both equations predicted the A_1 temperatures to be very close with minor differences as shown by the calculations below. However, the regression line in Figure 4.10 shows no linear relationship between measured A_{c1} and predicted A_1 temperatures for the Alexandrov et al's. revised equation. The effect of the Ni+Mn content on the A_{c1} temperature is presented in Figure 4.11. There is a negative linear relationship (R^2=0.45) between the Ac_1 temperature and the sum of the Ni+Mn content. It is shown on the graph that the A_{c1} temperature decreases with an increase in the sum of Ni+Mn content. The influence of austenite and ferrite forming elements to the A_{c1} temperature is demonstrated by four outliers in Figure 4.11. The LAB 76 and Commercial 3 weld metals with a stronger austenite influence, showed A_{c1} temperature closer to the PWHT temperature. The LAB 23 and LAB 172 weld metals also showed the A_{c1} temperature to be closer to the PWHT temperature. A low A_{c1} temperature in these two electrodes could be due to both austenite and ferrite forming element's influence.

Ngwenya predictive equations

$$A_1 = 847\text{-}341{,}09*C - 54.77*Si - 48.23Mn + 0.0424*Cr - 78.50Ni + 25.94*Mo + 120.24*V - 12.51Nb + 155.56N \quad \textbf{(4.3)}$$

$$A_3 = 872\text{-}469{,}71*C - 2.95*Si - 16.85*Mn + 1.54*Cr - 14.02*Ni - 3.74*Mo + 218.68*V - 3.02*Nb + 130.25N \quad \textbf{(4.4)}$$

Table 4.1: Measured and predicted phase transformation temperatures (ºC).

Sample identification	Measured Ac_1	Santella equation (A_1) [39]	Revised Alexandrov equation (A_1) [40]	Ngwenya equation (A_1)	Measured Ac_3	Ngwenya equation (A_3)
LAB 76	762	757	750	768	893	879
LAB 99	784	765	761	790	919	908
LAB 101	792	765	761	793	915	915
LAB 150	792	764	769	785	885	892
LAB153	776	766	764	779	880	887
LAB 154	793	772	770	786	891	893
LAB 155	781	770	769	782	892	891
LAB 169	793	778	779	794	893	895
LAB 171	779	773	822	778	886	882
LAB 172	771	774	842	786	893	891
LAB 19	785	757	732	778	877	883
LAB 20	787	768	782	787	884	890

Table 4.1: Continued

Sample identification	Measured Ac_1	Santella equation (A_1) [39]	Revised equation (A_1) [40]	Ngwenya equation (A_1)	Measured Ac_3	Ngwenya equation (A_3)
LAB 21	796	764	756	789	893	890
LAB 23	762	761	759	777	900	877
AB 24	778	761	756	775	863	879
Commercial 1	807	791	789	779	873	883
Commercial 2	784	757	750	813	873	870
Commercial 3	774	755	700	766	868	865
Base metal	814	803	807	809	876	877

Note: Ngwenya's A_1 and A_3 equations were derived in the present study

Table 4.2: Calculation of A_1 temperature (ºC) of LAB 24 using predictive equations.

Element	Content (wt%)	Alexandrov et al revised [36]		Santella [39]		Ngwenya	
		Constant	Contribution	Constant	Contribution	Constant	Contribution
Constant		2122,1	2113	805	805	847	847
Carbon (C)	0,09	-243	-22	-67,3	-6	-341,1	-31
Nitrogen (N)	0,066	-174	-11	-130,6	-9	155,56	10
Silicon (Si)	0,27	87,5	24	19,1	5	-54,77	-15
Manganese (Mn)	0,58	-24,4	-14	-60,5	-35	-48,23	-28
Cr^2		16,68	-	-	-	-	-
Chromium (Cr)	8,62	-271,8	-1104	2,5	22	0,0424	0
Ni^2		-365,5	-	-	-	-	-
Nickel (Ni)	0,58	153,1	-34	-72,3	-42	-78,5	-46
Mo^2		164	-	-	-	-	-
Molybdenum (Mo)	0,85	-306,5	-142	18,1	15	25,94	22
V^2		1324					
Vanadium (V)	0,15	-571,8	-56	37,1	6	120,24	18
Cu^2		-194,3	-	-	-	-	-
Copper (Cu)	0,03	83,9	2	-	-	-	-
Niobium (Nb)	0,1	-	-	-	-	-12,51	-1
Predicted A_1 temperature (ºC)	-	-	756	-	761	-	779

Note: Ngwenya's A_1 equation was derived in the present study

Table 4.3: Calculation of A_1 temperature (ºC) of Commercial 1 using predictive equations.

Element	Content (wt%)	Alexandrov et al revised [40]		Santella [39]		Ngwenya	
		Constant	Contribution	Constant	Contribution	Constant	Contribution
Constant		2122,1	2113	805	805	847	847
Carbon (C)	0,093	-243	-23	-67,3	-6	-341,1	-32
Nitrogen (N)	0,036	-174	-6	-130,6	-5	155,56	6
Silicon (Si)	0,257	87,5	22	19,1	5	-54,77	-14
Manganese (Mn)	0,83	-24,4	-20	-60,5	-50	-48,23	-40
Cr^2		16,68	-	-	-	-	-
Chromium (Cr)	7,82	-271,8	-1105	2,5	20	0,0424	0
Ni^2		-365,5	-	-	-	-	-
Nickel (Ni)	0,058	153,1	8	-72,3	-4	-78,5	-5
Mo^2		164	-	-	-	-	-
Molybdenum (Mo)	1,07	-306,5	-140	18,1	19	25,94	28
V^2		1324	-	-	-	-	-
Vanadium (V)	0,193	-571,8	-61	37,1	7	120,24	23
Cu^2		-194,3	-	-	-	-	-
Copper (Cu)	0,015	83,9	1	-	-	-	-
Niobium (Nb)	0,059	-	-	-	-	-12,51	-1
Predicted A_1 temperature (ºC)			789		791		814

Note: Ngwenya's A_1 equation was derived in the present study

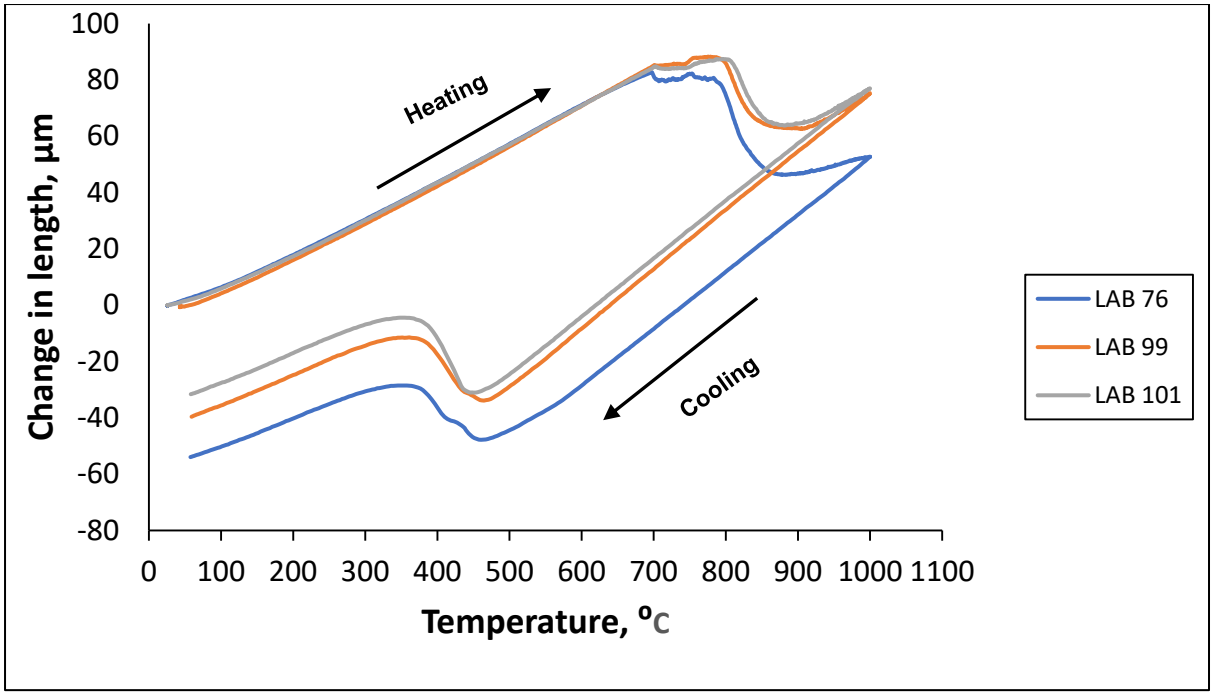

Figure 4.4: Dilatometry curves for the LAB 76, 99 and 101 weld metals.

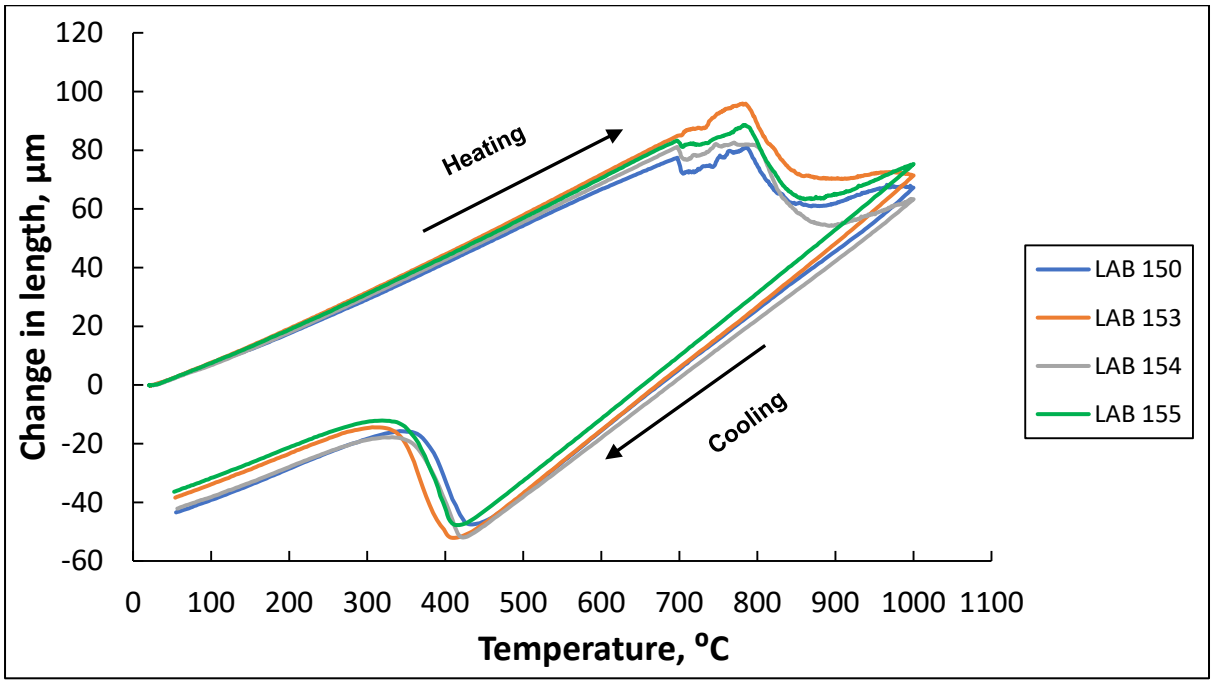

Figure 4.5: Dilatometry curves for the LAB 150, 153, 154 and 155 weld metals.

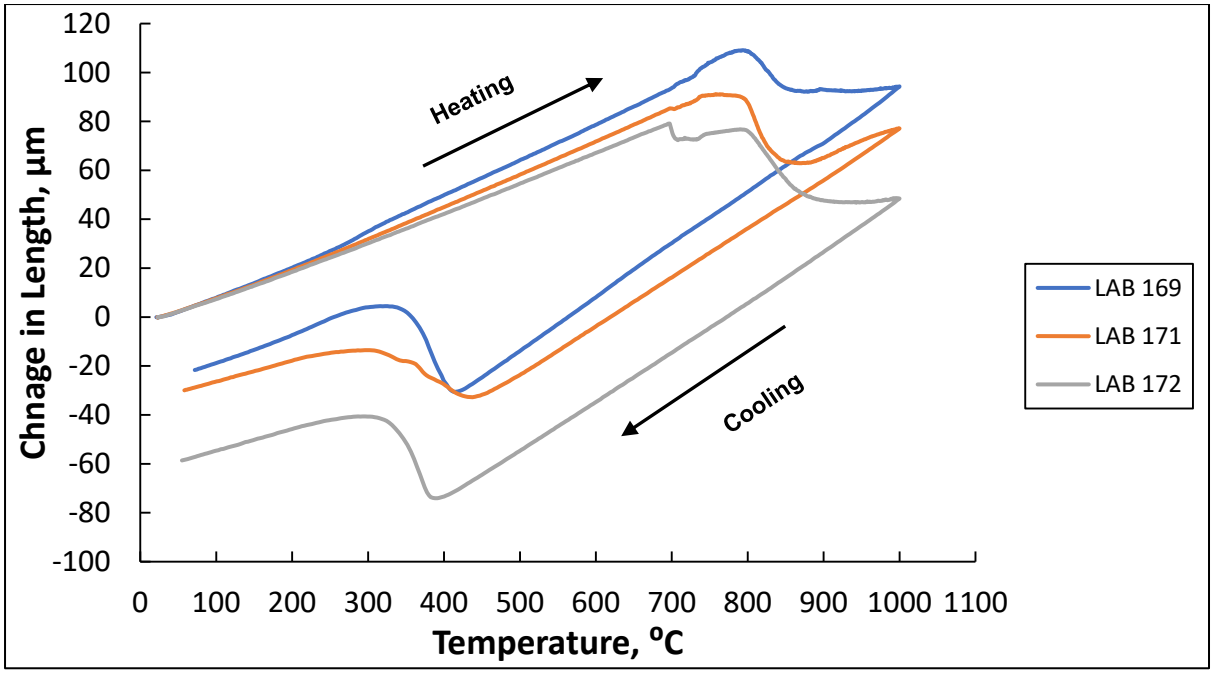

Figure 4.6: Dilatometry slow heating curves for the LAB169, 171, and 172 weld metals.

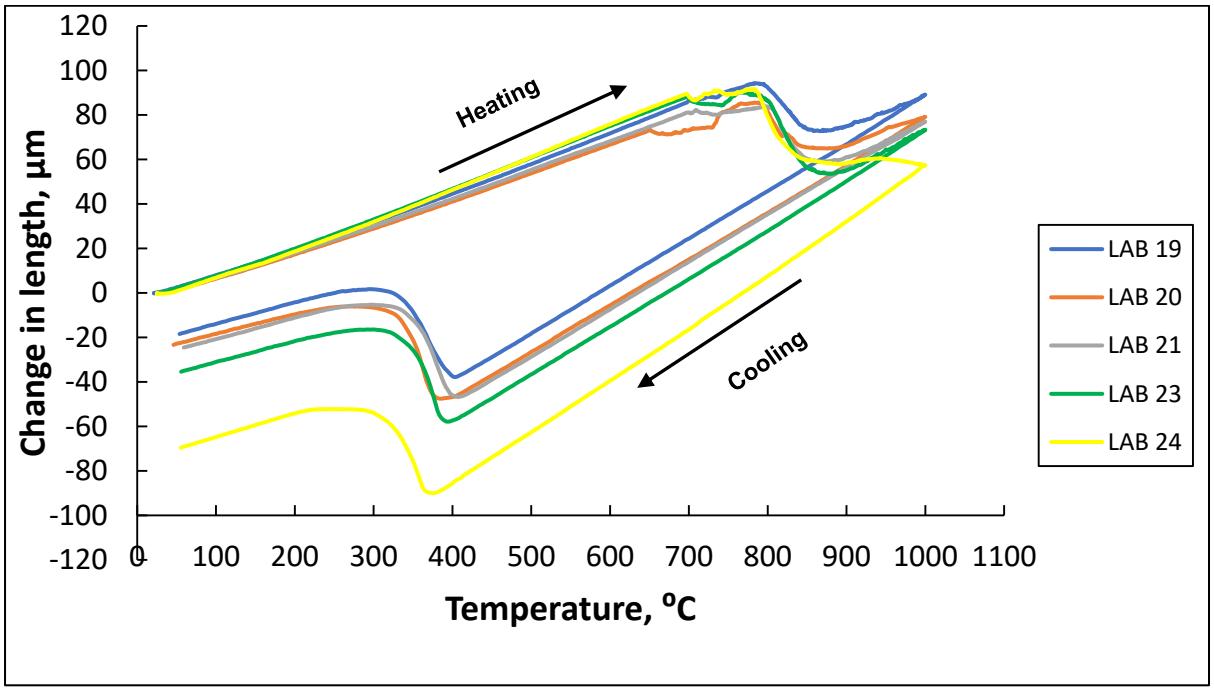

Figure 4.7: Dilatometry curves for the LAB 19, 20, 21, 23 and 24 weld metals.

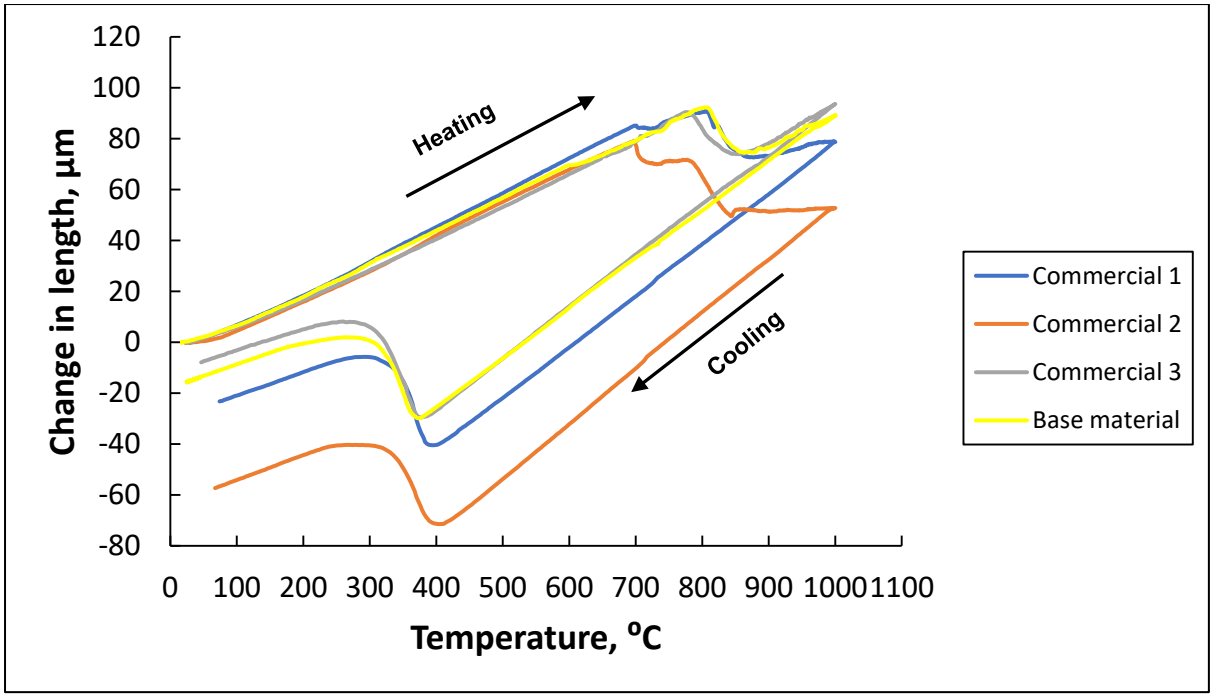

Figure 4.8: Dilatometry curves for the commercial 1, 2 and 3 weld metals and P91 base material.

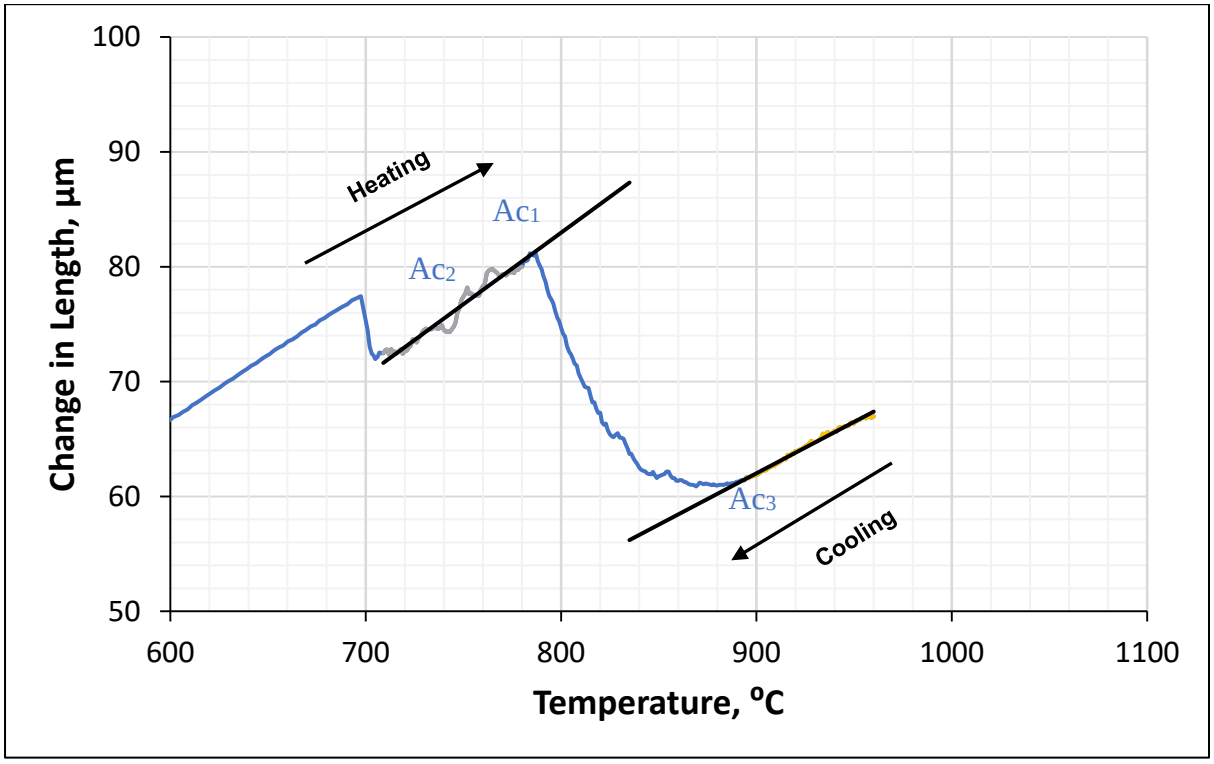

Figure 4.9: Dilatometry curve for the LAB 150 weld metal showing a transition from ferromagnetic to the paramagnetic state between 730 and 760°C (Ac_2 temperature).

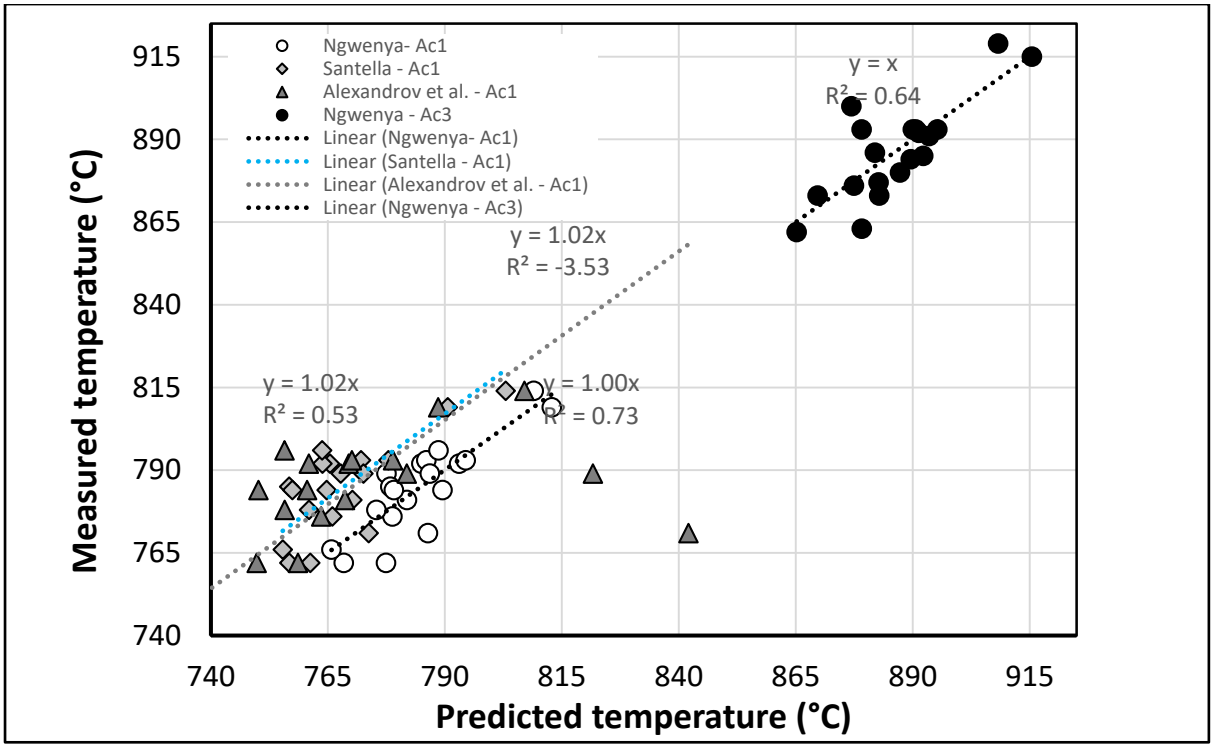

Figure 4.10: Measured against predicted values in 9Cr SMAW weld metals.

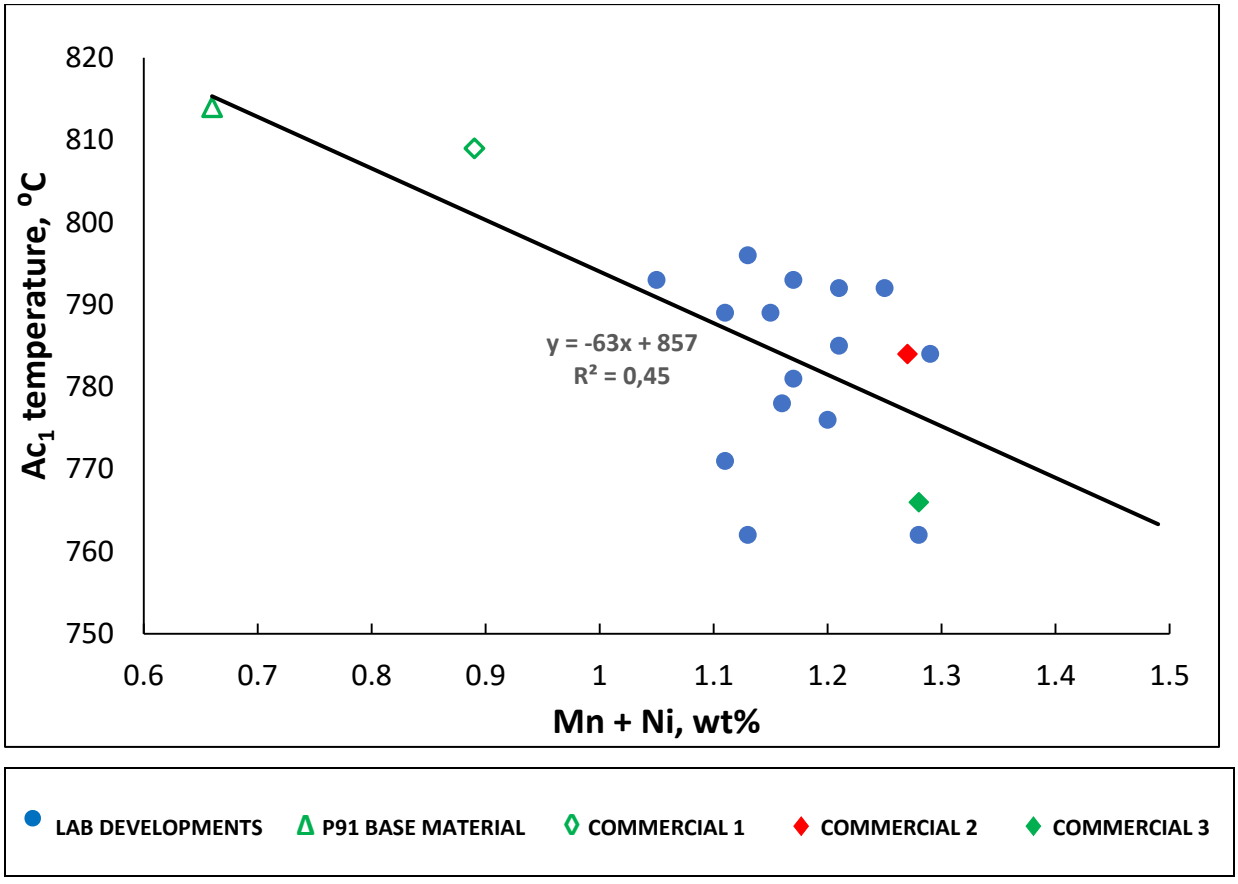

Figure 4.11: Influence of Mn + Ni content on the Ac_1 temperature, as measured during the current study.

Estimates of the A_1 temperature using Ngwenya's predictive equation were performed on chemical compositions selected hypothetically. The chemical composition of the Cr, Si, C, N, Mo and V were kept constant at the midrange of those of the AWS SFA 5.5 9018-B9 specification (Table 4.4). The Manganese and Nickel content were varied as shown in Table 4.4. The estimated A_1 temperatures for the above-mentioned chemical compositions are shown in Table 4.5. It is shown on the table that reducing the Ni+Mn content resulted in an increase in the A_1 temperature.

Table 4.4. Midrange chemical composition of P91 SMAW electrode

Element (wt%)	C	Si	Cr	Mo	V	N
Weld metal	0.11	0.15	9.25	1.03	0.225	0.045

Table 4.5. Estimated A_1 temperature of the hypothetical selected chemical composition

Ni (wt%)	0.4	0.6	0.4	0.6	0.4	0.6	0.4
Mn (wt%)	1.1	0.9	0,8	0,6	0.6	0.4	0.4
A1 (ºC)	778	772	792	786	796	802	812

4.5 The martensite start (Ms) temperature

The martensite start temperature results of laboratory developed electrodes, commercial electrodes and base metal are presented in Figures 4.12 to 4.14. All the regression lines showed no linear correlation between the measured and predicted M_s temperatures, except that of the Ngwenya (Equation 4.5) equations. This equation was developed in the present study from 18 chemical compositions from laboratory experimental and commercial electrodes. The equation regression line shows a positive linear relationship between the measured and predicted M_s temperatures (Figure 4.14). Equation 4.5 shows that an increase in the carbon and nitrogen content results in a significant decrease in the M_s temperature, as expected. The effect of Si, Mn, Cr, V and Ni as shown in equation 4.5, is contrary to what was expected, that is, these elements had a positive coefficient. This factor is considered to be a statistical anomaly, due to the variation in these elements (Appendix B, Table B1). The statistical summary of the predicted and measured M_s temperatures are given in Table 4.6. Most of the predictive equations show an average M_s temperature extremely lower than the

average measured M_s temperature with Andrew 2 [42] exhibiting higher values greater than 500ºC. As shown in Table 4.6, the average measured M_s temperature was closed to the Zhao LM and Ngwenya predictive average M_s temperatures. It is worth mentioning that only Zhao formula was within the composition range of P91 steels. However, no linear relationship existed between the measured and Zhao LM predicted M_s temperatures (Figure 4.15).

$$\mathbf{M_s = 351.4 - 824.3C + 108.7Si + 83.7Mn + 5.88Cr + 290.1V + 67.1Ni - 44.4Mo - 711.9N} \quad \mathbf{(4.5)}$$

Table 4.6: Statistical comparison of measured and predicted M_s temperatures

Identification	Minimum	Maximum	Standard deviation
Measured M_s	379	471	31
Payson & Savage	152	240	24
Rowland & Lyle	151	239	24
Grange & Steward	58	182	34
Nehrenberg	207	277	19
Steven & Haynes	299	356	15
Andrew 1	345	387	12
Andrew 2	482	561	22
Zhao TM	309	331	5
Zhao LM	408	447	11
Ngwenya	387	453	25

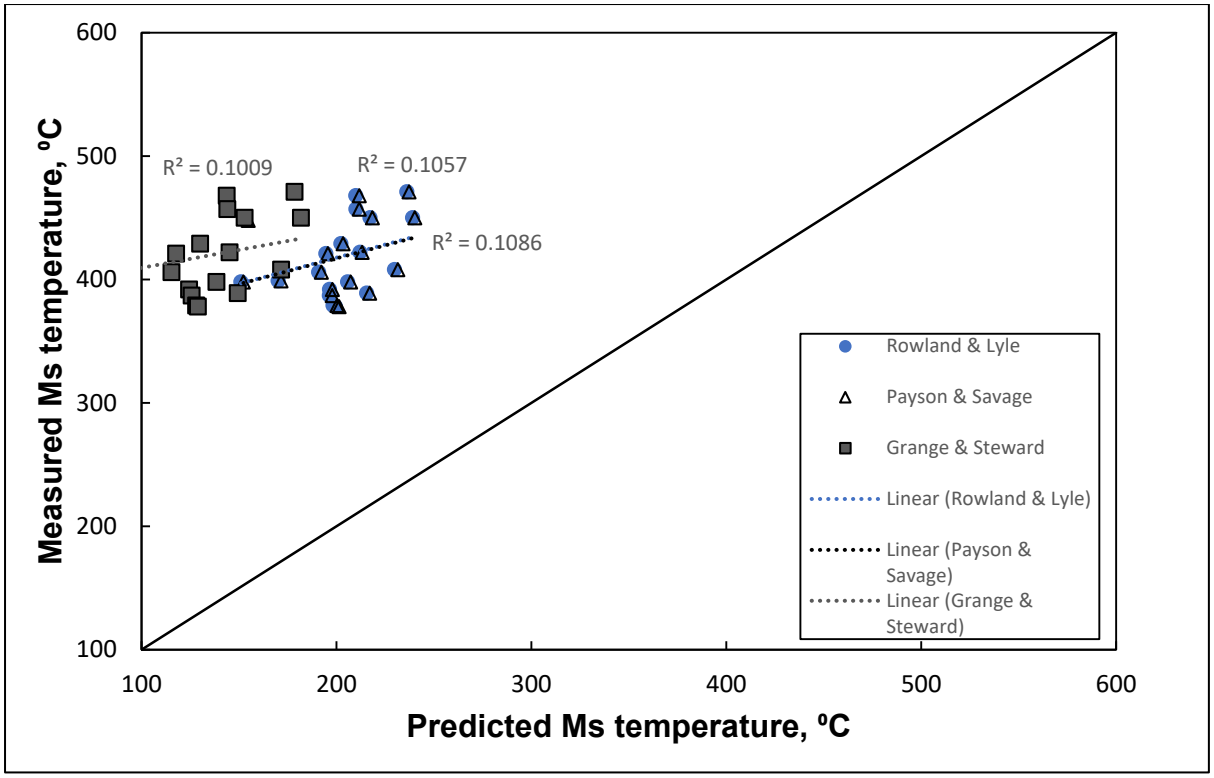

Figure 4.12: Measured against predicted M_s in P91 SMAW welds.

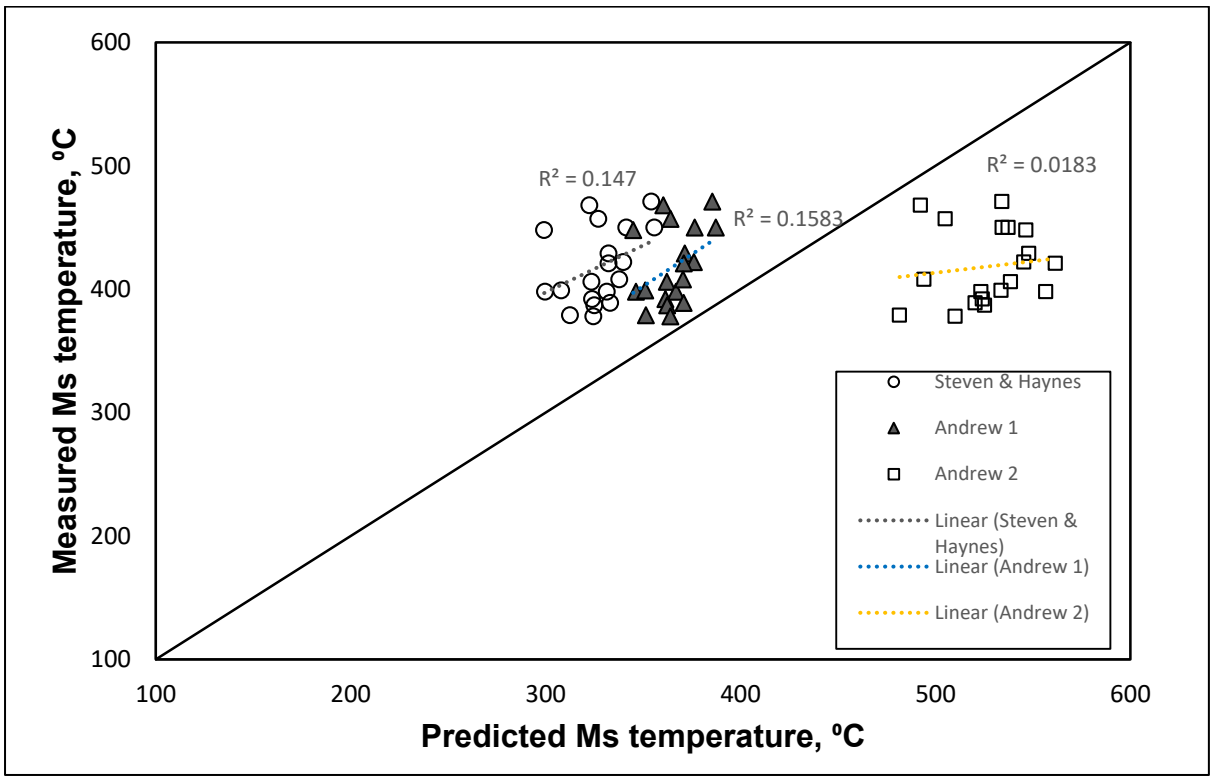

Figure 4.13: Measured against predicted M_s in P91 SMAW welds.

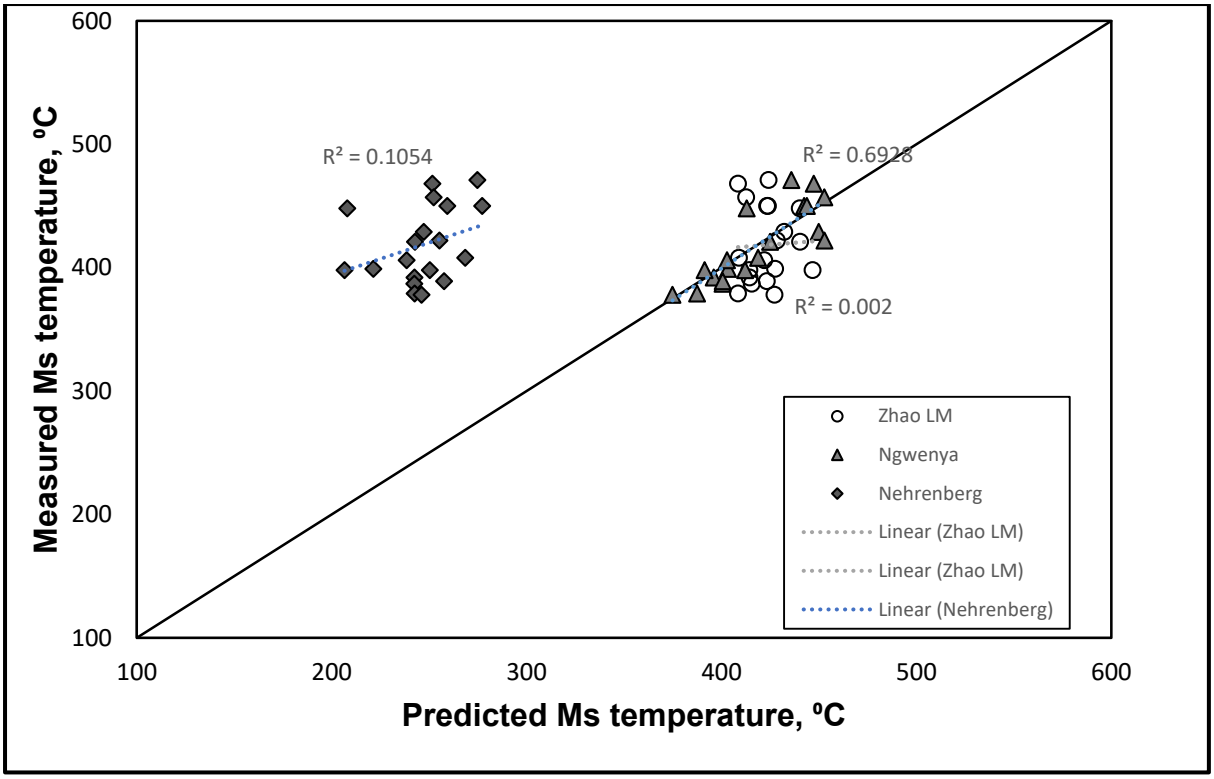

Figure 4.14: Measured against predicted M_s in P91 SMAW welds.

4.6 Effect of post weld heat treatment on P91 the weld metal

The post weld heat treatment of the weld metal is generally carried out to stabilise the microstructure, improve the toughness, reduce the hardness and relieve stresses after welding. PWHT is normally performed to minimize the hardness mismatch of the weld metal (450HV as-welded) and the base metal (220HV as-received). The PWHT process of fifteen laboratory developed electrodes, three commercial electrodes and P91 base metal were simulated in the Bähr Dil 805D and the Lenton furnace according to the AWS SFA 5.5 E9018-B9 specification. The PWHT of LAB 24 was performed in both of these equipment's to verify the process.

Samples subjected to PWHT were characterised by optical microscopy, scanning electron microscopy and Vickers hardness measurements. Figures 4.15 is the dilatometry curve for the commercial 2 weld metal simulating a post weld heat treatment according to the AWS SFA 5.5 E9018-B9 specification in the weld metal. The PWHT was performed to ascertain that no phase transformation occurs during

this process, in the weld metal. The dilatometry curves for the PWHT samples did not exhibit any phase transformation. A phase transformation was also not detected in the LAB 169 weld metal during the PWHT process as shown in Figure 4.16. A contraction was observed at approximately 730ºC to 740ºC which could be from a transition from ferromagnetic to paramagnetic properties as illustrated in Figure 4.10. The measured A_{c1} and the predicted A_1 temperatures for the LAB 169 weld metal was above the PWHT temperature (Table 4.1). The A_{c1} temperature of commercial 2 weld metal was measured above the PWHT temperature, with both the Santella and Alexandrov et al's. predictive equations giving the A_1 temperature below that of the PWHT temperature (Table 4.1). However, the Ngwenya predicted A_1 temperature was above that of the PWHT temperature. The M_s temperatures of both the LAB 169 and commercial 2 weld metals were not observed on their respective PWHT dilatometry curves.

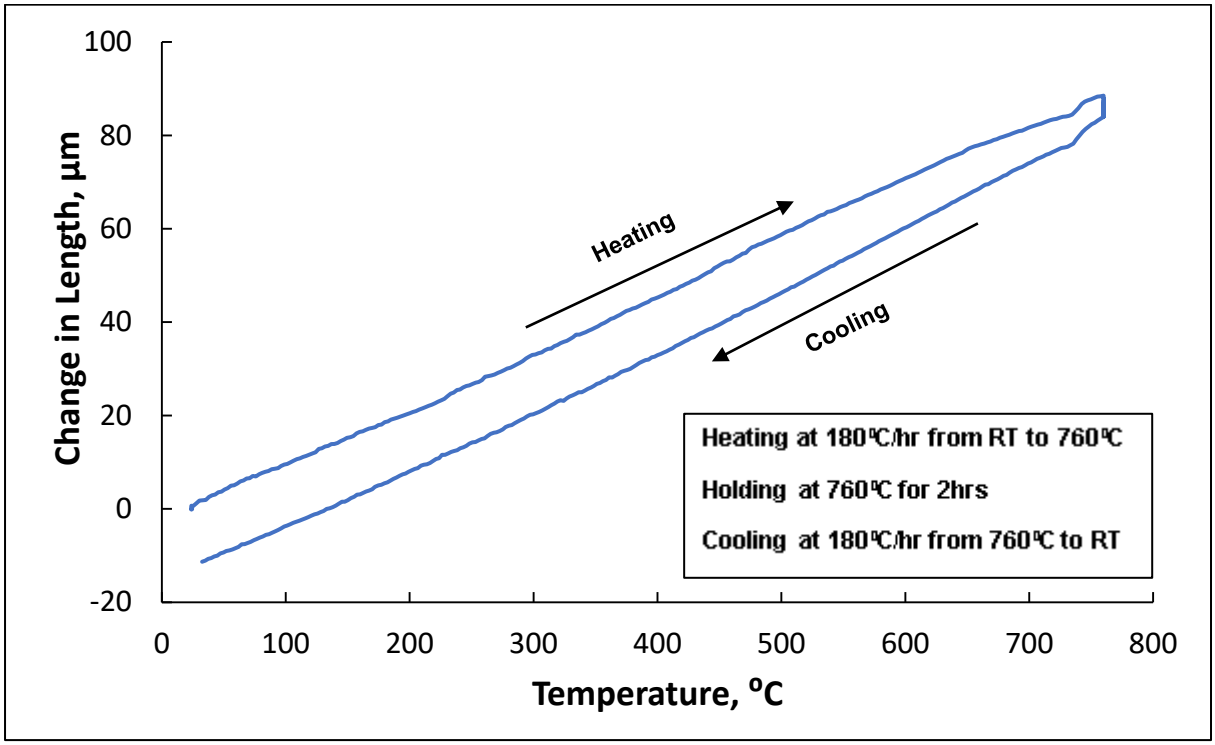

Figure 4.15: Dilatometry curve for the Commercial 2 weld metal simulating the PWHT in the weld according to AWS SFA 5.5 9018-B9.

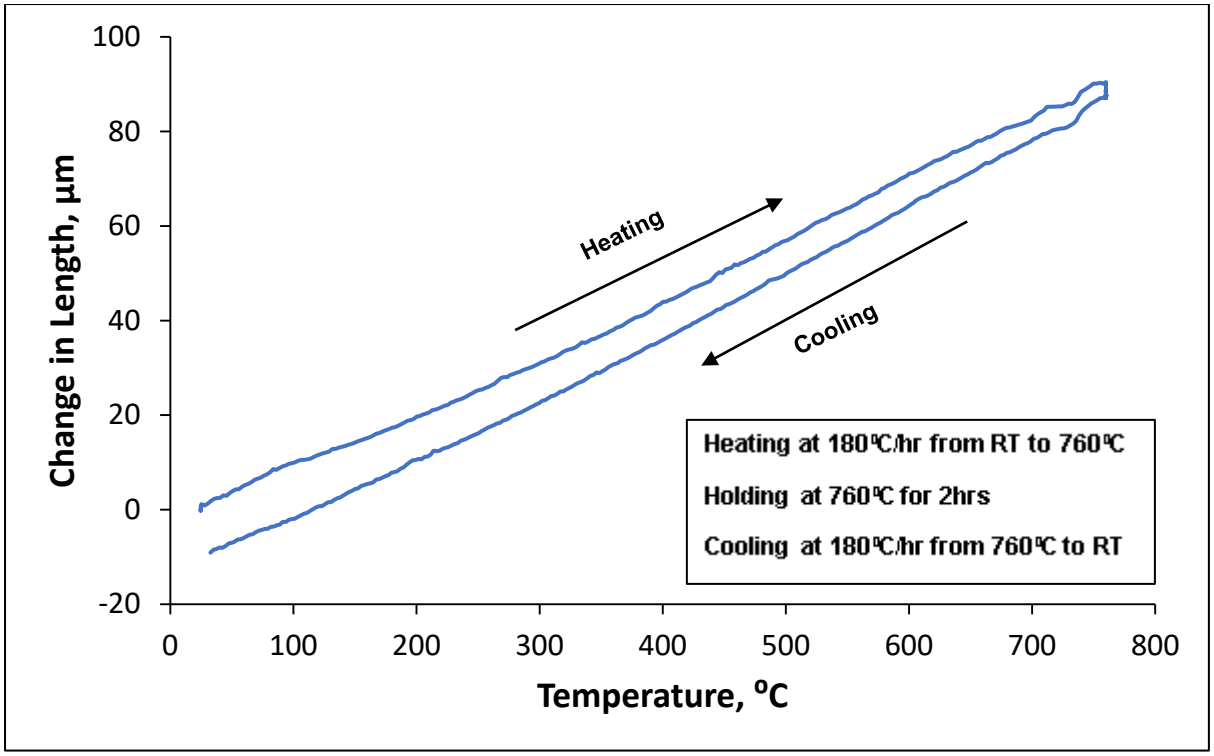

Figure 4.16: Dilatometry curve for the LAB 169 weld metal simulating the PWHT in a SMAW weld metal according to AWS SFA 5.5 9018-B9.

4.7 Microstructural analysis

4.7.1 Base metal

A typical microstructure of martensite laths was exhibited in all three conditions. Figure 4.17a is an optical micrograph after the PWHT process, showing a martensitic microstructure. A SEM micrograph revealed precipitates on and along the grain boundaries (Figure 4.17b). In the as-received condition, the base metal had a microstructure similar to the one observed above.

4.7.2 Weld metal

4.7.2.1 As-welded microstructure

Fifteen laboratory developed and three commercial electrodes were characterised in the as-welded condition in this section. The summary of the results in the as-welded condition is reported in Table 4.7. Generally, in the as-welded condition, the laboratory developed and commercial 3 electrodes exhibited a martensitic microstructure. Inclusions were observed in as polished condition on all the microstructures

characterised. Figure 4.18 (a) is an optical micrograph of the LAB 76 weld metal showing a martensitic microstructure. A SEM micrograph of the LAB 76 weld metal also revealed martensite with no precipitates, shown at this magnification (Figure 4.18b). Most of the welds showed the prominent amount of a phase or structure with a dark etching appearance that could not be identified immediately in their respective microstructures. The formation of the dark etching phase or structure could be attributed to the tempering of previously deposited run(s) in the inter-critical region.

The LAB 24 weld metal's microstructure consisted of fine martensite (light phase) with isolated areas of dark phase as shown in Figure 4.19a. Figure 4.19b is a SEM micrograph of the LAB 24 weld metal showing martensite. The commercial 1 and 2 weld metal exhibited optical microstructures of martensite (light phase), the dark etching phase with isolated areas of delta ferrite. Figures 4.20 (a) and (b) are optical and SEM micrographs of the commercial 1 weld metal showing a microstructure consisting of martensite (white) and the dark etching phase. The dark etching phase appears to form on the prior austenite grain boundaries and along martensite laths in all the characterised welds. No precipitates were observed in the as-welded condition at the magnification shown below.

4.7.2.2 Microstructure after dilatometry, using a heating rate of 28ºC/h

Most of the laboratory developed electrodes and commercial electrodes exhibited a fully martensitic microstructure after a slow heating dilatometry. A dark etching phase was also observed in most of these weld metals. Figures 4.21 (a) and (b) are optical and SEM micrographs of the LAB 169 weld metal showing martensite laths. Inclusions were observed on the SEM micrograph. The LAB 24 sample's optical micrograph showed a microstructure with predominantly the martensite (light phase) and dark etching phase (Figure 4.22a). A SEM micrograph of the LAB 24 sample showed a microstructure of martensite (white) and inclusions (Figure 4.22b). Microstructures of full martensite were observed in all three commercial electrodes and no delta ferrite was detected in the slow heating condition in these welds. An optical micrograph of the commercial 1 weld metal displaying martensite (grey phase) and the dark etching phase is shown in Figure 4.23a. Figure 4.23b is a SEM micrograph of the commercial 1 weld metal showing a fine martensite microstructure. The dark etching phase in the

slow heating condition is also associated with the prior austenite grain boundaries and along the martensite laths.

4.7.2.3 Microstructure after a PWHT at 760ºC for 2 hours

The post weld heat treatment process produced microstructures with predominately tempered martensite in the laboratory developed electrodes. However, a microstructure consisting of martensite and alpha ferrite (α-ferrite) was observed in the LAB 169 and 172 weld metal developments after the PWHT process. In the other two conditions (i.e. as-welded and slow heating), a fully martensitic microstructure was observed in these experimental electrodes. Figure 4.24a is an optical micrograph of the LAB 169 weld metal showing martensite and α-ferrite. The SEM micrograph of LAB 169 weld metal showed martensite, α-ferrite and precipitates (see, Figure 4.24b). The photomicrograph of the LAB 24 weld metal displaying a microstructure of martensite (grey) and the dark etching phase is shown in Figure 4.25a. A SEM micrograph of the LAB 24 weld metal showing the martensite and precipitates mostly on and along the grain boundaries is shown in Figure 4.25b. The commercial 2 weld metal exhibited an optical microstructure of fine martensite and delta ferrite (Figure 4.26a). Figure 4.26b is a SEM micrograph of this weld metal showing a microstructure of martensite and delta ferrite.

No delta ferrite was observed in the last weld bead of the laboratory experimental electrodes and commercial electrodes.

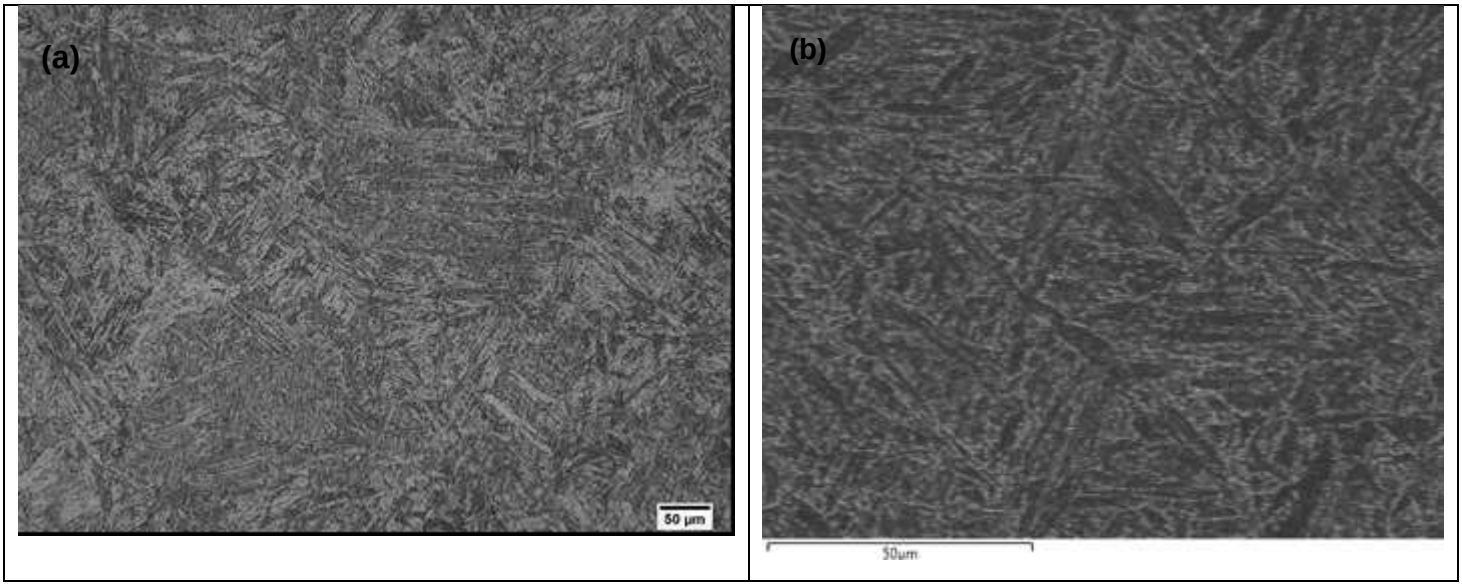

Figure 4.17: P91 base metal in the PWHT condition**,** (a) optical micrograph showing tempered martensite (b) SEM micrograph material showing martensite and precipitates.

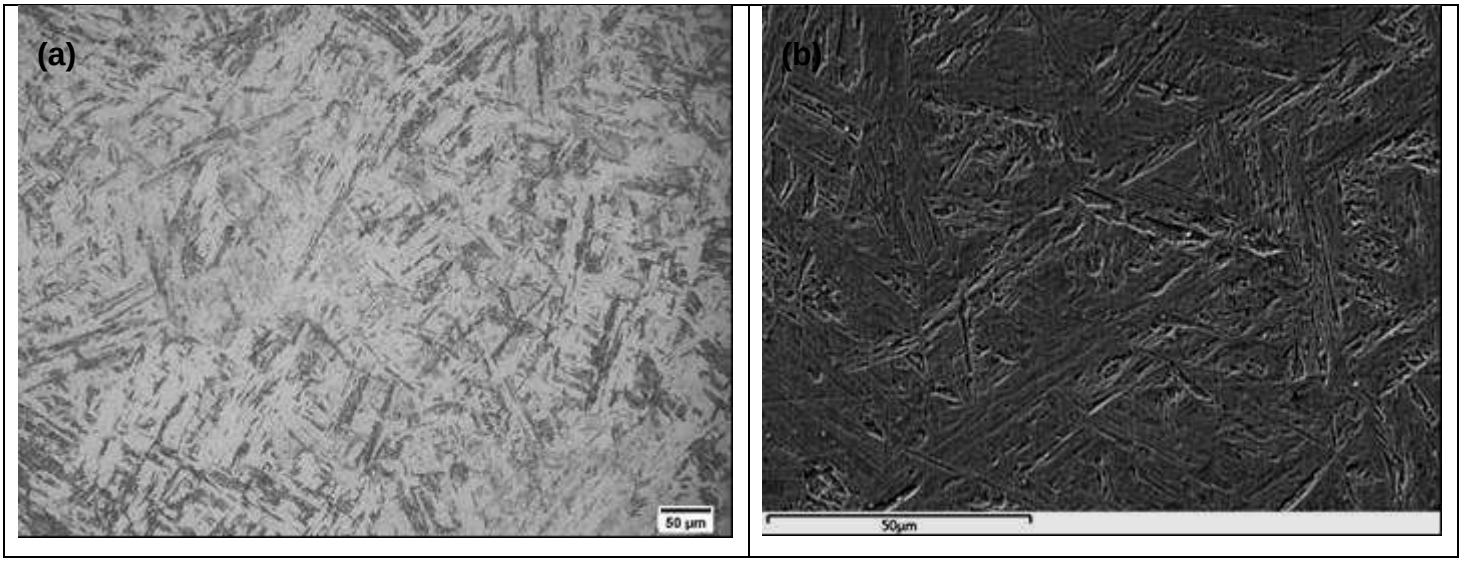

Figure 4.18: The LAB 76 sample in the as-welded condition (a) Optical and (b) SEM micrographs showing martensitic microstructure.

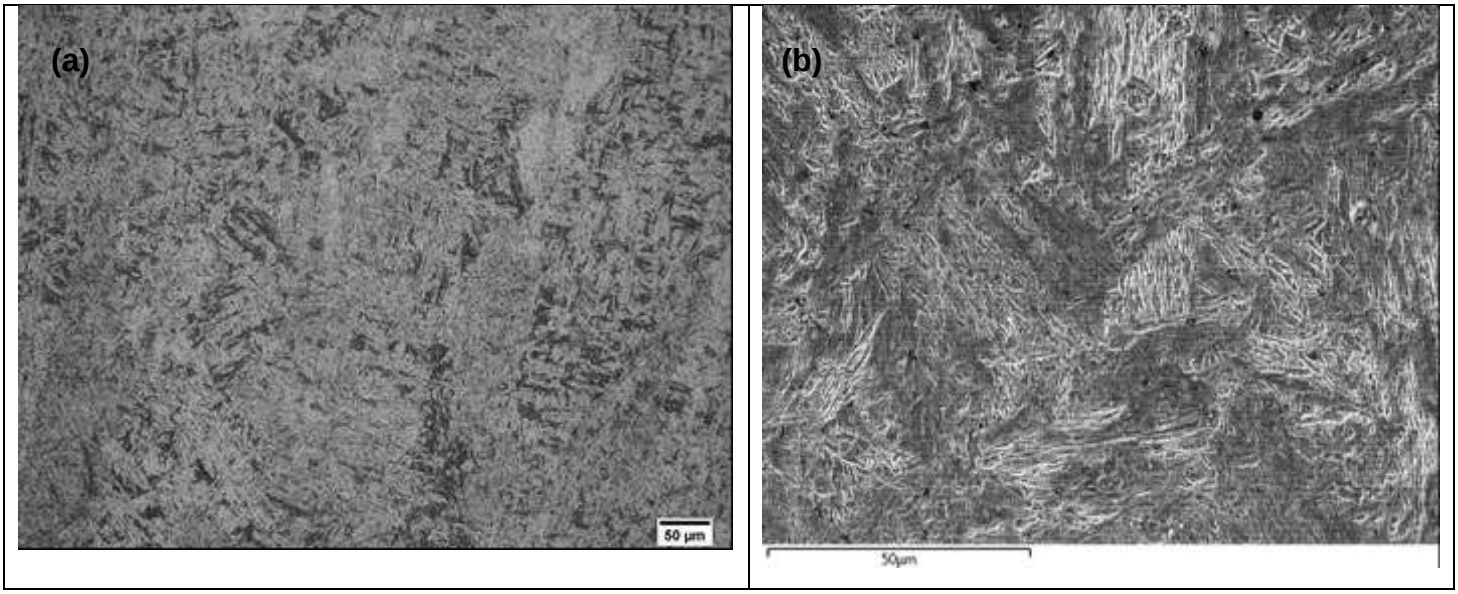

Figure 4.19: The LAB 24 as-welded sample (a) optical micrograph showing martensite (light phase) and dark etching phase and (b) SEM micrograph of martensite (x1000).

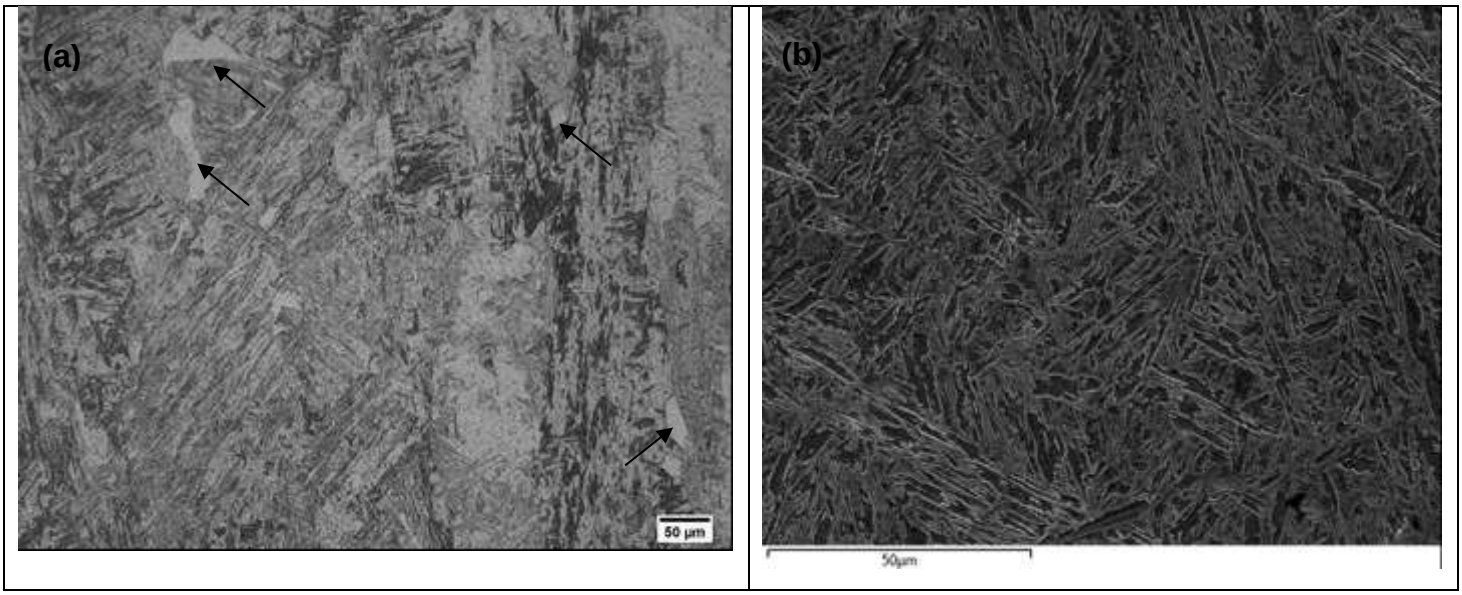

Figure 4.20: As-welded commercial 1 weld (a) optical micrograph showing martensitic light phase, dark etching phase and isolated areas of delta ferrite (indicated by arrows) and (b) SEM micrographs exhibiting a similar microstructure (X1000).

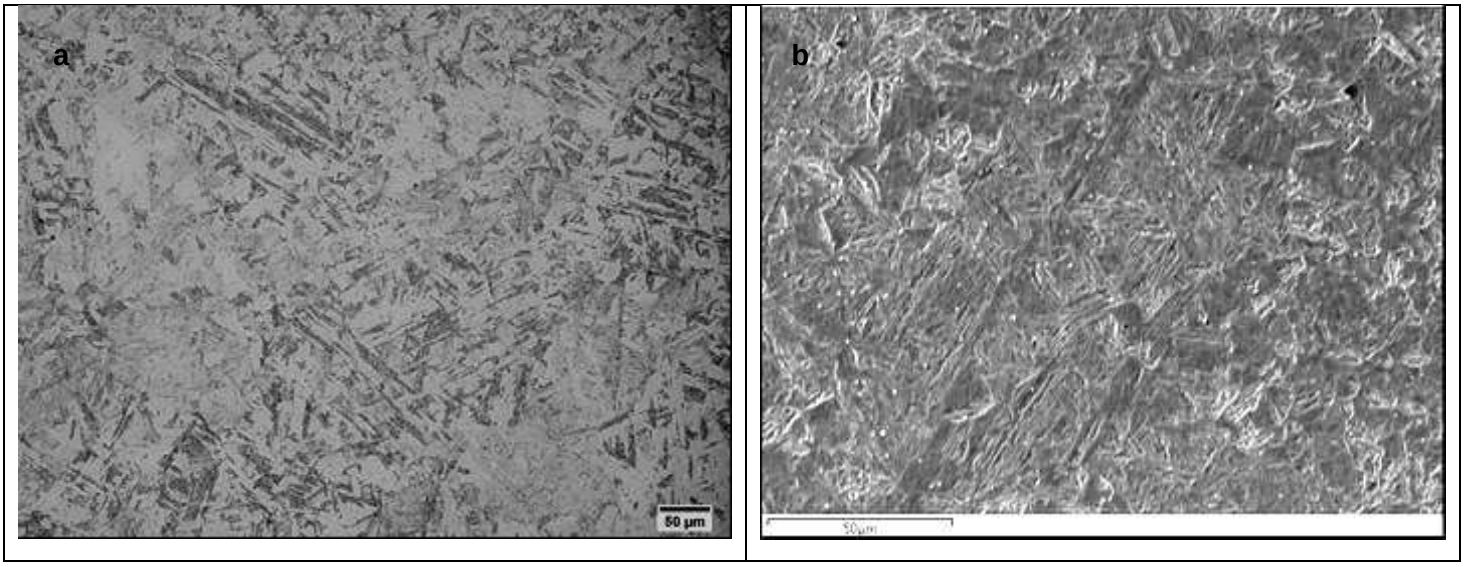

Figure 4.21: The LAB 169 sample after dilatometry in the slow heating condition (a) Optical and (b) SEM micrograph showing martensite laths. Inclusions (white) were visible on the SEM micrograph (X1000).

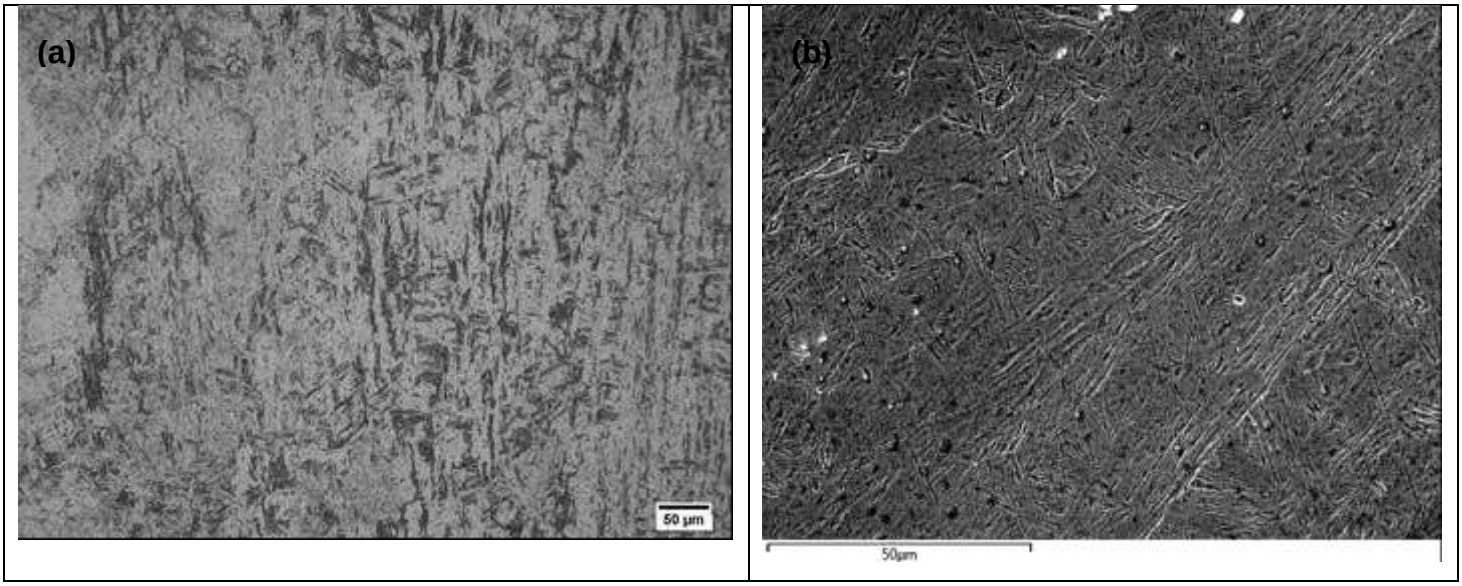

Figure 4.22: The LAB 24 sample in the dilatometry slow heating condition (a) optical micrograph showing martensite (light phase) and dark etching phase and (b) SEM micrograph showing martensite. Inclusions (white and dark) are shown on the SEM micrograph (X1000).

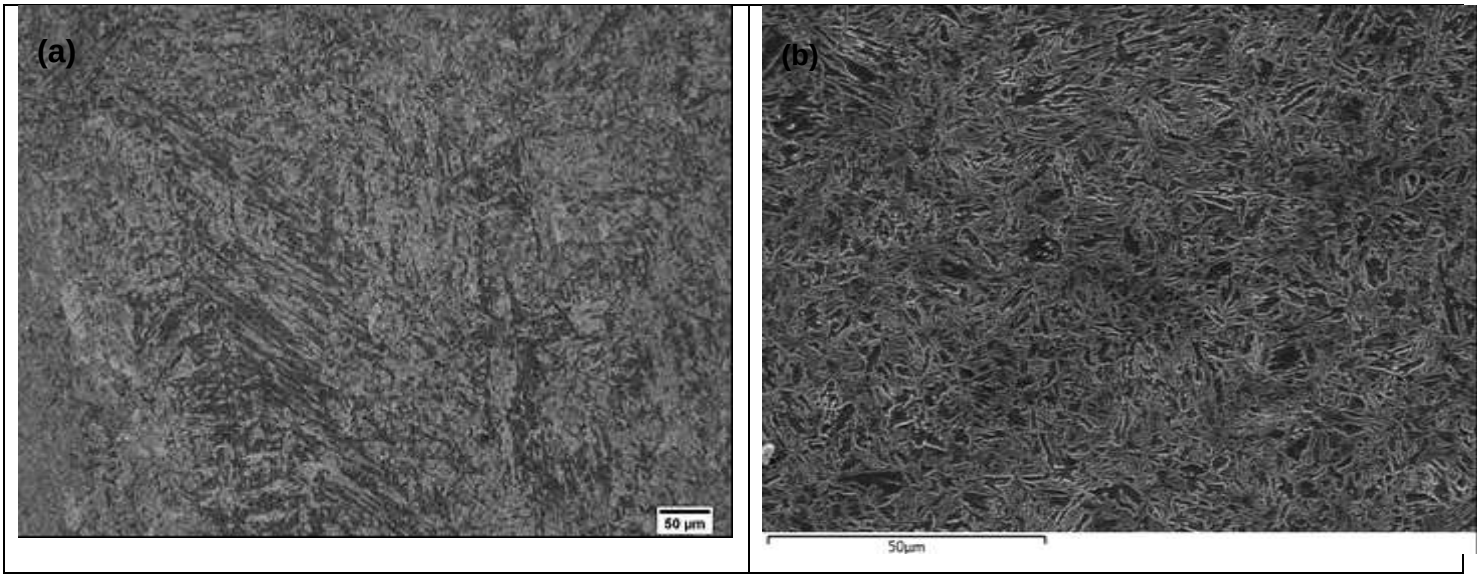

Figure 4.23: The commercial 1 weld metal in the dilatometry slow heating condition (a) optical micrograph showing martensite (grey) and dark etching phase and (b) SEM micrograph showing a martensitic microstructure (X1000).

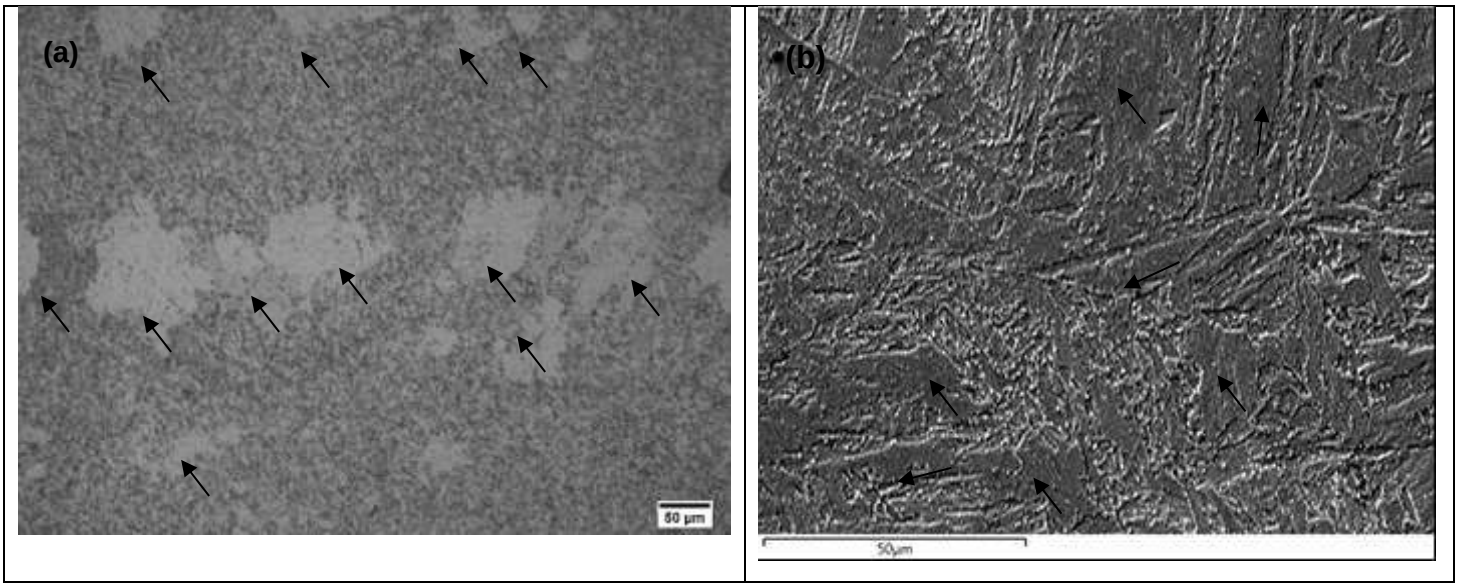

Figure 4.24: The LAB 169 sample in the PWHT condition (a) Optical micrograph showing fine martensite and α-ferrite (b) SEM micrograph showing martensite and α-ferrite (indicated by arrows) and precipitates (X1000).

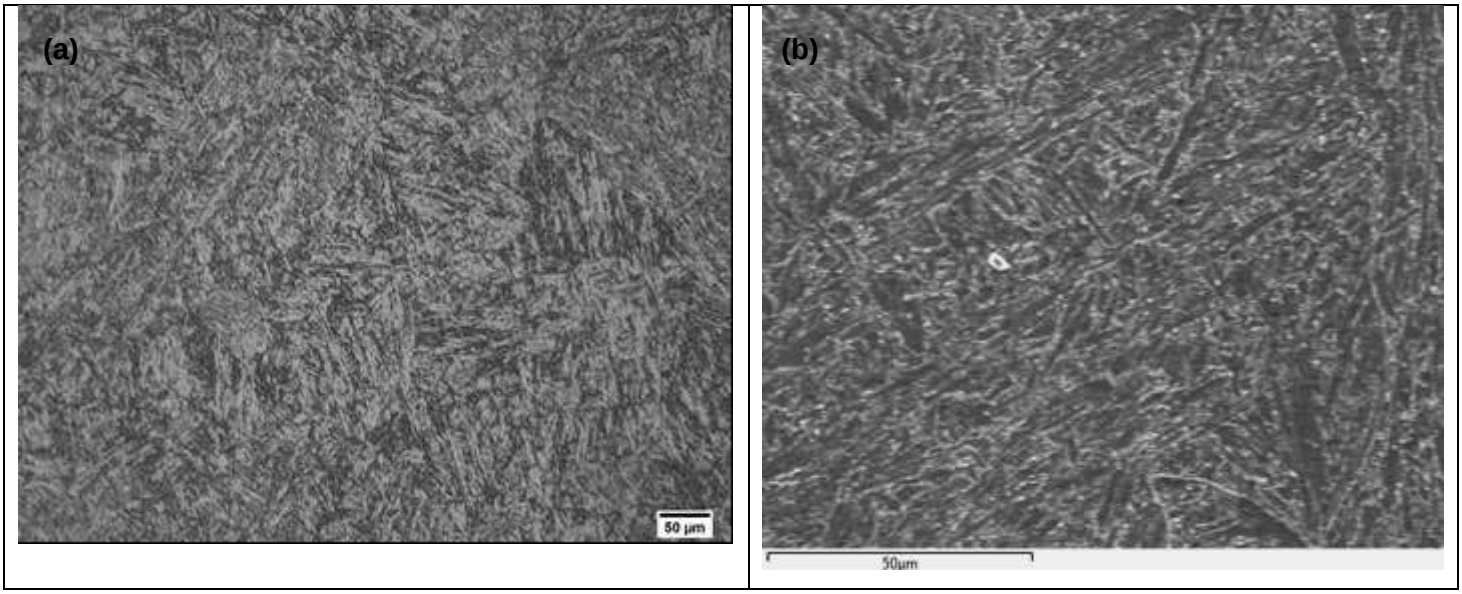

Figure 4.25: The LAB 24 sample in the PWHT condition (a) optical micrograph showing martensite and dark etching phase. SEM micrograph showing martensite and precipitates on and along the grain boundaries (X1000).

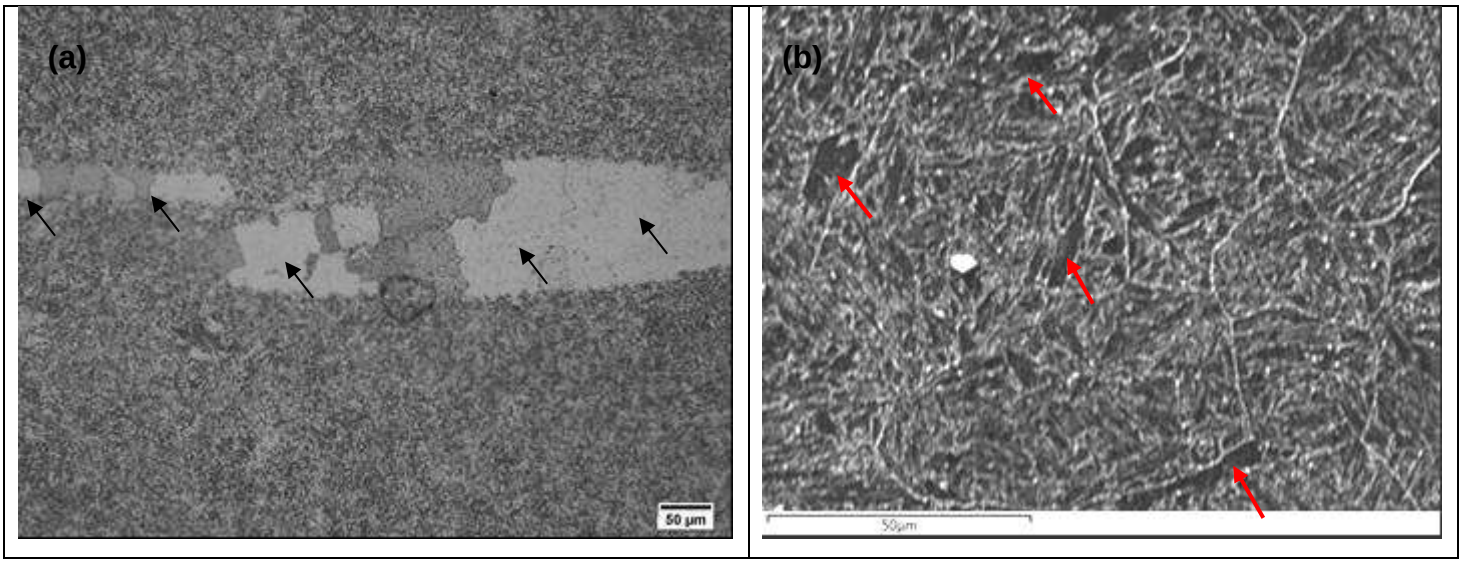

Figure 4.26: The commercial 2 sample in the PWHT condition (a) optical showing fine martensite and δ-ferrite (b) SEM micrograph showing martensite, δ-ferrite (dark) and precipitates (X1000).

Table 4.7: Summary of the optical microstructures

Sample identification	As-welded	Slow heating	PWHT
LAB 76	Martensite	Martensite	Tempered martensite
LAB 99	Martensite	Martensite	Tempered martensite
LAB 101	Martensite	Martensite	Tempered martensite
LAB 150	Martensite and dark etching phase	Martensite and dark etching phase	Tempered martensite
LAB 153	Martensite and dark etching phase	Martensite and dark etching phase	Tempered martensite
LAB 154	Martensite	Martensite	Tempered martensite
LAB 155	Martensite and dark etching phase	Martensite and dark etching phase	Tempered martensite
LAB 169	Martensite	Martensite	Tempered martensite and islands of alpha ferrite[2]
LAB 171	Martensite	Martensite	Tempered martensite
LAB 172	Martensite	Martensite	Tempered martensite and isolated alpha ferrite[2]
LAB 19	Martensite	Martensite	Tempered martensite
LAB 20	Martensite and dark phase	Martensite and dark etching phase	Tempered martensite
LAB 21	Martensite	Martensite	Tempered martensite
LAB 23	Martensite	Martensite	Tempered martensite
LAB 24	Martensite and dark etching phase	Martensite and dark etching phase	Tempered martensite and dark etching phase
Commercial 1	Martensite, dark etching phase and delta ferrite[1]	Martensite and dark etching phase	Tempered martensite
Commercial 2	Martensite, dark etching phase and delta ferrite[1]	Martensite and dark etching phase	Tempered martensite with islands of delta ferrite[1]
Commercial 3	Martensite	Martensite	Tempered martensite
P91 base material	Martensite	Martensite	Tempered martensite

Note:

[1] delta ferrite was identified (see section 5.5.2.2 for full description)

[2] alpha ferrite was identified (see section 5.5.2.3 for full description)

4.7.3 The high resolution SEM analysis

High resolution scanning electron microscopy secondary images on selected samples are presented in this section. Figure 4.27 is a high magnification SEM micrograph of the LAB 24 sample showing martensite (light phase) and a dark etching phase in the as-welded condition. Fine precipitates (white) were also observed on the SEM micrograph, mostly inside the grains and along the martensite laths. High magnification SEM secondary image of the commercial 2 sample in the as-welded condition exhibited martensite (light phase), dark etching phase and isolated areas of delta ferrite (indicated by arrows) are shown in Figure 4.28. The commercial 2 sample also showed fine precipitates (white) inside the grains but they were less prominent when compared to LAB 24 sample.

Figure 4.29 is high magnification SEM micrograph of the commercial 1 in the as-welded condition showing the delta ferrite phase surrounded by martensite (light phase).

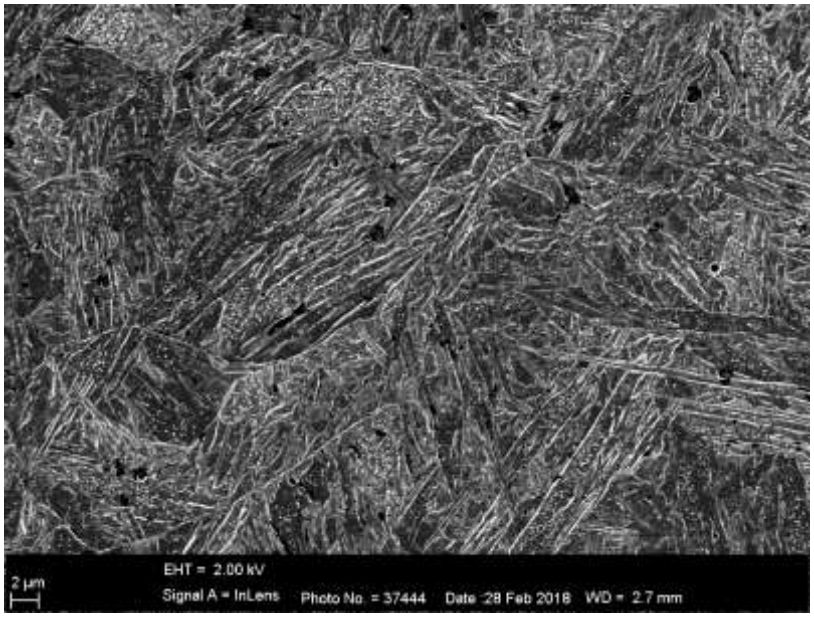

Figure 4.27: SEM micrograph of the LAB 24 weld metal showing martensite (white), dark etching phase and precipitates (white) inside and along martensite laths in the as-welded condition. Inclusions (black) were also visible (X5000).

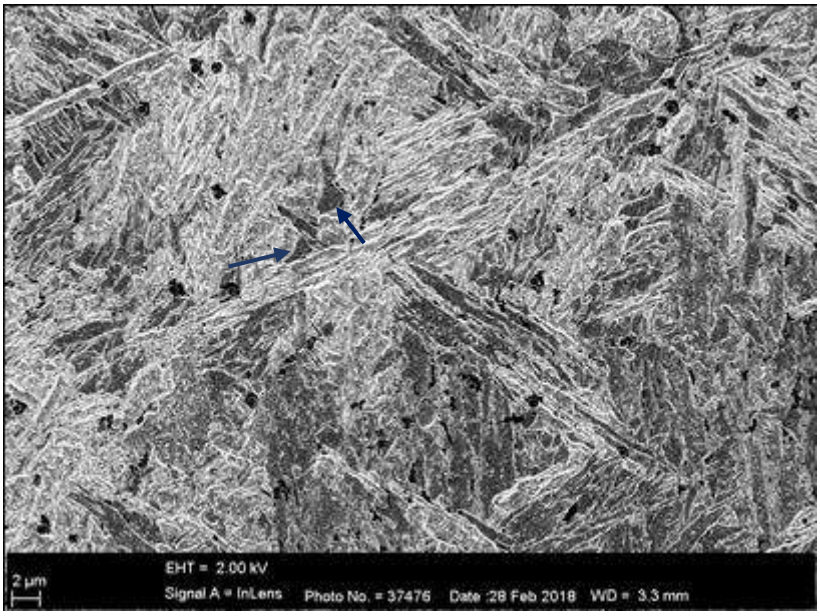

Figure 4.28: SEM micrograph of the commercial 2 weld metal showing martensite (white) and dark phase and delta ferrite (indicated by an arrow) in the as-welded condition. Inclusions were also visible (X5000).

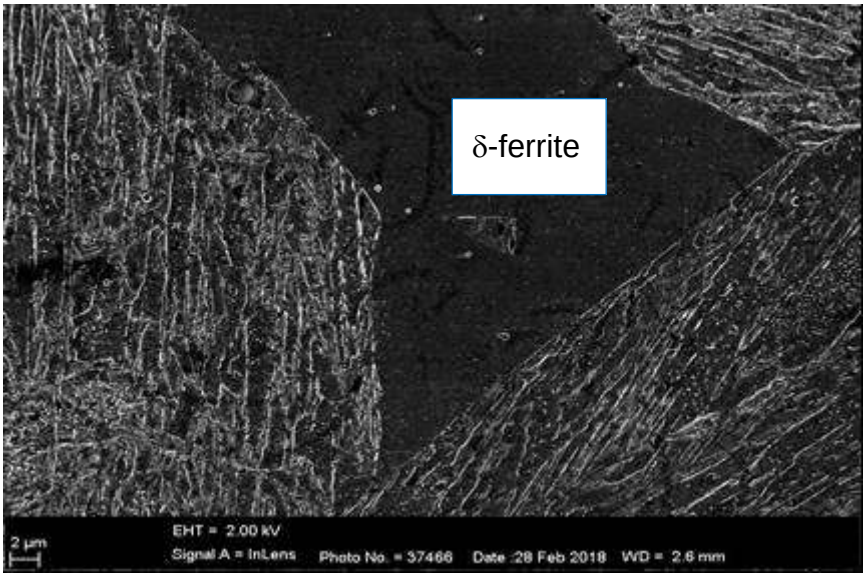

Figure 4.29: As-welded SEM photomicrograph of the commercial 1 weld metal showing δ-ferrite surrounded by martensite (X5000).

4.8 Relationship between the ferrite factor and the delta ferrite content

The ferrite factor results of the laboratory experimental electrodes and commercial electrodes calculated using chromium and nickel equivalents, are presented in Table 4.8. As shown in Table 4.8, the results were in the following range;10 to13.1 Cr_{eq}, 3.7 to 5.6 Ni_{eq} and 5.2 to 8.4 ferrite factor (FF). Figure 4.30 is a graphical presentation of the effect of the ferrite factor on the volume fraction α /δ ferrite of these electrodes. Most of the laboratory developed electrodes and commercial 3 weld metal did not exhibit delta ferrite phase in their microstructures, except for the LAB 169, LAB 172, commercial 1 and commercial 2 weld metals. The average volume fraction of ferrite phase estimated with a 95 percent confidence interval of the following weld samples; LAB 169 (PWHT), LAB 172 (PWHT), commercial 1 (AW), commercial 2 (AW and PWHT) are shown in Table 4.9. The LAB 169 (PWHT) sample had the highest (0.19) volume fraction of ferrite and the commercial 1 (AW) sample showed the lowest (0.04). The other three weld samples volume fraction of ferrite phase was between 0.07 and 0.14.

Table 4.8: Chromium-equivalent (Cr_{eq}), Nickel-equivalent (Ni_{eq}) and Ferrite factor (FF) of the weld metals.

Sample ID	Cr_{eq}	Ni_{eq}	FF
LAB 76	10,1	4,0	6,1
LAB 99	11,9	5,5	6,4
LAB 101	12,1	5,3	6,8
LAB 150	10,3	4,1	6,3
LAB 153	11,1	4,3	6,8
LAB 154	11,9	4,0	7,9
LAB 155	11,4	4,0	7,4
LAB 169	11,6	3,7	7,9
LAB 171	12,8	4,8	8,1
LAB 172	13,1	4,7	8,4
LAB 19	11,3	5,3	6,0
LAB 20	12,5	5,0	7,5
LAB 21	11,7	5,0	6,7
LAB 23	11,0	5,2	5,7

Table 4.8: Continued

Sample ID	Cr_{eq}	Ni_{eq}	FF
LAB 24	11,4	5,2	6,2
Commercial 1	11,0	4,2	6,8
Commercial 2	10,2	5,0	5,2
Commercial 3	10,9	5,6	5,3

Table 4.9: Volume fraction of ferrite phase.

Sample ID	Total no. of points counted (P_T)	No. of points in α (Pα)	Estimated volume fraction α (P_p)	Standard deviation σ(Pα)	95% confidence interval =1.96σ (P_p)
LAB 169 PWHT	100	19	0.19	0.044	0.19±0.09
LAB 172 PWHT	100	14	0.14	0.037	0.14±0.07
Commercial 1 AW	100	4	0.04	0.02	0.04±0.04
Commercial 2 AW	100	7	0.07	0.026	0.07±0.05
Commercial 2 PWHT	100	9	0.09	0.03	0.09±0.06

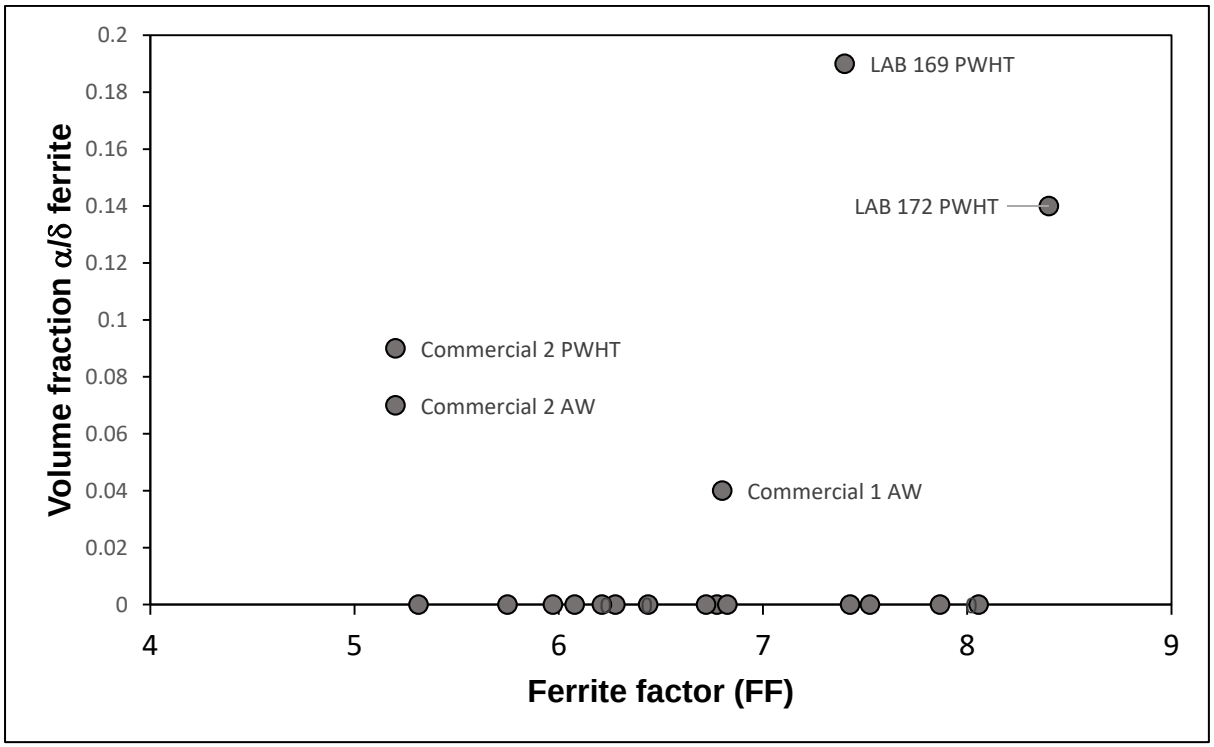

Figure 4.30: The effect of ferrite factor on the measured volume fraction of α / δ ferrite.

4.9 Vickers hardness analysis

The average Vickers hardness results of the welds and base metals in the as-welded / as-received, dilatometry slow heating, and PWHT conditions are presented in Table 4.10. In the as-welded condition, the hardness ranged between 305 to 449 HV for the experimental developed electrodes. After slow heating in the dilatometry test, the hardness ranged between 333 to 464 HV, with the minimum and the maximum values slightly higher than in the as-welded condition. All three commercial welds showed a hardness above 400 HV in both the as-welded and slow heated conditions, except for commercial 3 sample in the slow heating condition with a value of 399 HV. A post weld heat treatment of the weld metals at 760^{o}C for 2 hours reduced the hardness significantly, to within the ASME SA335 P91 specification (i.e.196-265 HV). The minimum and maximum values after post weld heat treatment were 211 and 263 HV respectively. A graphical representation of the Vickers hardness of the weld and base metals in the as-welded / as-received and dilatometry slow heating conditions is shown in Figure 4.31. The regression line shows no linear relationship (R^2= -0.464) between the hardness in as-welded / as-received and after dilatometry slow heating conditions. Three outliers were observed on the graph, namely, the LAB 150 weld metal, LAB 153 weld metal and the base metal. The two weld samples had a hardness below 400HV in the as-welded condition with a fully martensitic microstructure. With the absence of softer ferrite phase in these two weld sample's microstructures, the hardness close to 300HV could not be explained. A hardness of 228HV on the base metal can be attributed to the normalised and tempered martensitic microstructure observed in the as-received condition.

Figures 4.32 to 4.34 show optical micrographs of the LAB 169, commercial 1 and commercial 2 samples' hardness profiles of phases in their respective microstructures. Vickers hardness values below 190 HV were reported in LAB 169 and commercial 2 samples indicating the presence of delta/alpha ferrite. The hardness profile in the commercial 1 sample was above 400 HV with two values above 500 HV reported from the dark etching phase. Hardness values above 400 HV were found in both the light and dark etching phases, indicating that these phases could be similar. There were no discrepancies with hardness values obtained after PWHT for both dilatometry and

Lenton furnace samples. This was confirmed by the hardness values of 259 and 263 HV obtained in dilatometry and Lenton furnace samples for the LAB 24 sample. The base metal hardness in the as-received and after post weld heat treatment conditions were similar (Table 4.10).

Table 4.10: Average Vickers hardness (HV 300g) of welds and base metal.

Sample ID	As-welded	Slow heating	PWHT
LAB 76 *	365 ± 7	365 ± 18	231 ± 8
LAB 99*	410 ± 10	365 ± 15	243 ± 10
LAB 101*	419 ± 12	390 ± 11	249 ± 7
LAB 150	399 ± 8	333 ± 23	235 ± 7
LAB153	305 ± 7	385 ± 14	250 ± 4
LAB 154 *	401 ± 13	402 ± 7	256 ± 4
LAB 155	390 ± 12	395 ± 11	258 ± 9
LAB 169	358 ± 29	386 ± 14	211 ± 39
LAB 171*	434 ± 7	435 ± 12	260 ± 6
LAB 172*	421 ± 12	409 ± 11	256 ± 6
LAB 19 *	416 ± 12	415 ± 10	253 ± 5
LAB 20	393 ± 43	416 ± 9	243 ± 15
LAB 21*	431 ± 12	406 ± 6	256 ± 7
LAB 23 *	431 ± 9	429 ± 8	261 ± 6
LAB 24	420 ± 46	434 ± 10	263 ± 8
LAB 24*	-	-	259 ± 4
Commercial 1	449 ± 17	430 ± 12	258 ± 6
Commercial 2	437 ± 19	414 ± 16	246 ± 15
Commercial 3	418 ± 23	399 ± 13	253 ± 6
Base material	228 ± 7	464 ± 13	228 ± 8

*indicate PWHT process in the Lenton furnace

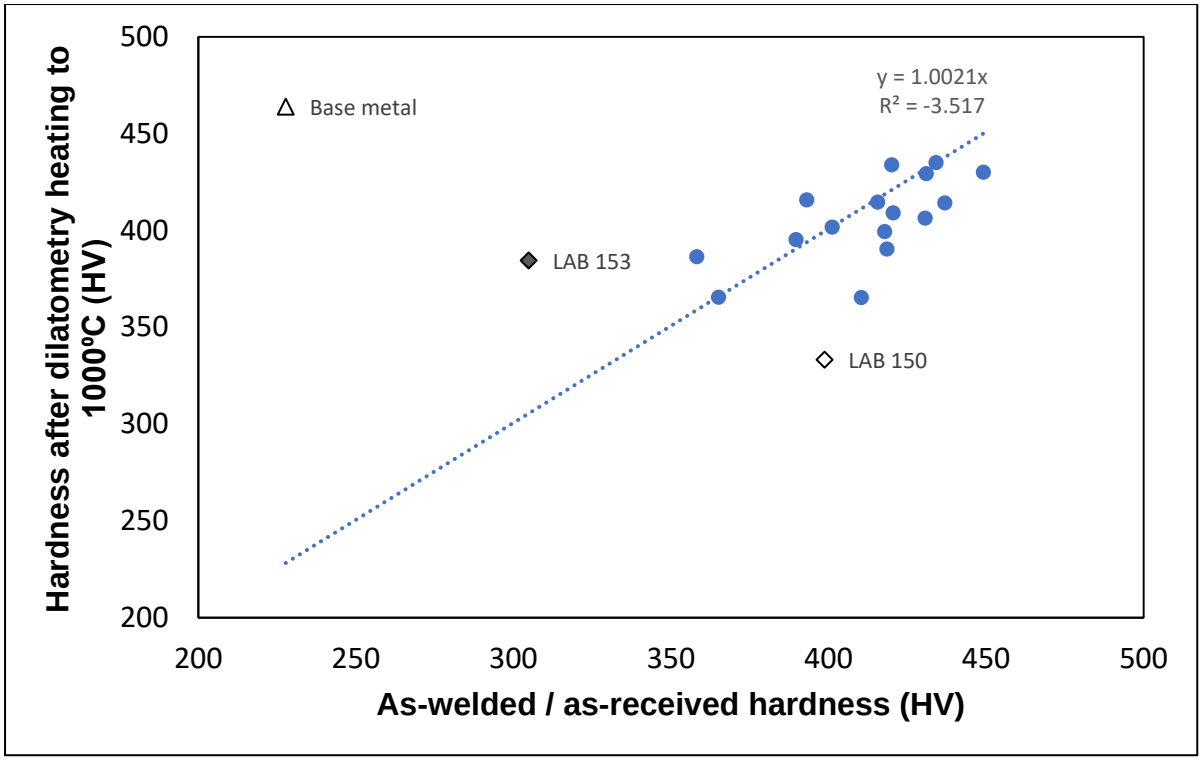

Figure 4.31: Vickers hardness in the as-welded and after dilatometry heating to 1000°C conditions.

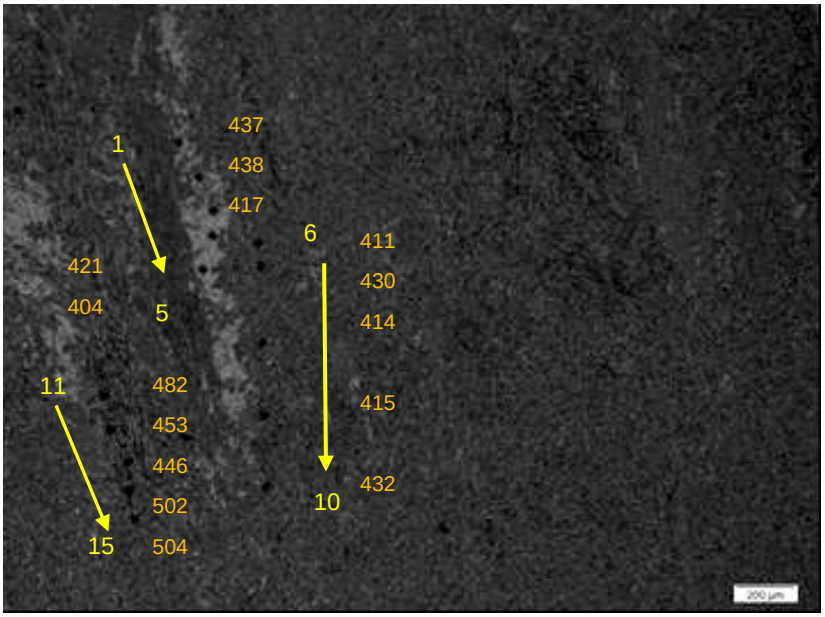

Figure 4.32: Optical micrographs showing Vickers hardness profile in the commercial 1 dilatometry sample.

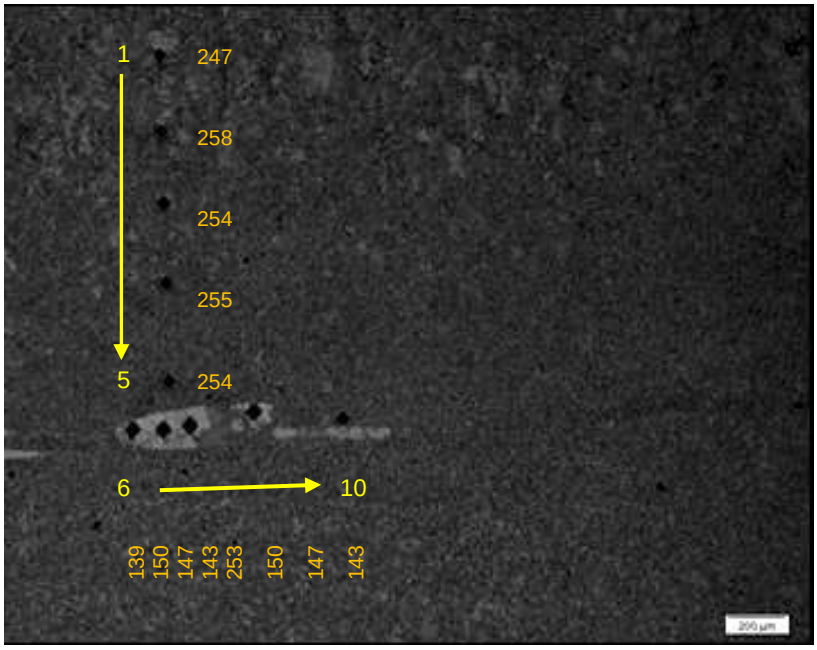

Figure 4.33: Optical micrographs showing Vickers hardness profile in the commercial 2 PWHT sample

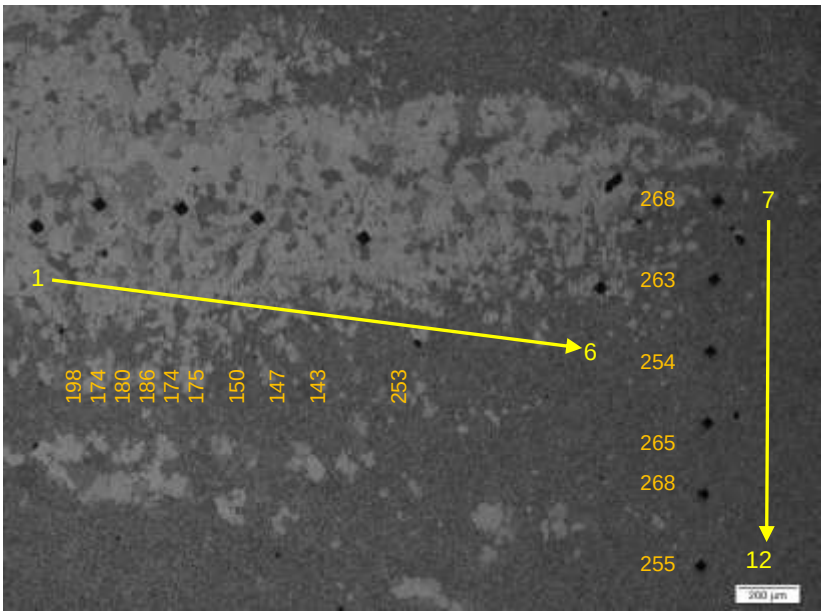

Figure 4.34: Optical micrographs showing Vickers hardness profile in the LAB 169 PWHT sample.

CHAPTER 5: DISCUSSION

5.1 Overview

This chapter discusses the following results:

- Weldability evaluation of P91 electrodes (section 5.2)
- A_{c1}, A_{c2} and A_{c3} transformation temperatures (section 5.3)
- M_s transformation temperatures (section 5.4)
- Microstructural analyses (section 5.5
- Effect of PWHT, carbon and nitrogen on the Vickers hardnesses (section 5.6)

5.2 Weldability evaluation of P91 electrodes

The weldability characteristics of some of the laboratory developed electrodes were comparable to the three commercial electrodes. Phase 5 development electrodes showed better welding characteristics than those of the other phases, notably the LAB 24 electrode (see Table A1 for a comprehensive report in Appendix A). However, the slag characteristics in the LAB 24 sample was not self-lifting when compared to the three commercial electrodes. The slag was splitting, cracking and easy to remove from the base material as shown in Figure 4.3. Some electrodes in the LAB 24 and Commercial 2 electrodes had poor eccentricity which resulted in inefficient shielding during welding, causing inclusions in the weld metal of both the developed and commercial electrodes as shown in Figures 4.28 and 4.29.

The metal transfer during welding as evaluated qualitatively by the welder was good. The chemical composition in the electrodes of the phase 5 development met requirements of the AWS SFA 5.5 9018-B9 specification (see, Appendix B). However, the phosphorus content in all of the development phase electrodes could not be reduced to the standard requirements of less than 0.01wt% and ranged from 0.018 to 0.034wt%. The commercial 2 electrode also showed the phosphorus content to be above the maximum specification (0.014wt%). The sulphur content was on the maximum side of the specification (0.01wt %). No reports on the effect of high phosphorus content on the hardness and the A_{c1} temperature of the P91 weld metal could be found. The moisture content of the experimental electrodes was less 0.4

percent (0.13 to 0.18wt %) as required by the AWS specification which is an indication of a low hydrogen content in the flux formulations.

5.3 A_{c1}, A_{c2}, and A_{c3} transformation temperatures

5.3.1 Base metal

Alexandrov et al. [36] and Nitsche & Mayr [38] (equilibrium conditions) reported the A_{c1} temperature of the P91 base metal to be above the PWHT temperature (>760ºC). These results agreed with the present study with the measured and predicted A_{c1} temperatures found to be above the A_{c1} temperature (>800ºC) as shown Tables 2.6 and 4.1. Nitsche and Mayr [38] in their study on P91 base metal also reported A_{c3} temperatures ranging from 828 to 934ºC under equilibrium conditions. The measured A_{c1} temperature in this study was found to be 876ºC and within the temperature range of Nitsche and Mayr [38] study.

5.3.2 Weld metal

The measured A_{c1} temperatures of the weld metals were found to be above the PWHT temperature. However, both Santella [37] and Alexandrov et al [36]. predicted the A_1 temperatures to be below the PWHT temperature (Table 4.1). Silwal et al. in their study found the A_{c1} temperature of 818ºC on the grade P91 weld sample (welded with GTAW and FCAW) with the heating rate (28ºC /h), which is similar to that of the present study after 700ºC [41]. The A_1 temperatures calculated by predictive equations were in the range of 757 to 791ºC for Santella [39] and 748 to 840ºC for revised Alexandrov et. al [40] equations. The A_1 temperatures given by the Santella equation were comparable to the measured A_{c1} temperatures with plus or minus 1 to 32ºC temperature differences recorded. This was supported by a regression line showing the positive linear relationship (R^2=0.53) between the measured A_{c1} and the predicted A_1 temperatures in Figure 4.11. The regression line for the Alexandrov et. al revised equation [40] showed no linear relationship between the measured A_{c1} temperature and the predicted A_1 temperature (R^2=-3.53). The temperature difference of plus or minus 6 to 66ºC between A_{c1} and A_1 temperatures were recorded. The outliers were observed in Figure 4.11, namely, in the LAB 171 and 172 samples which could be attributed to the higher chromium contents (above 10wt%).

The measured A_{c1} temperatures of the three commercial weld metals were between 774 and 807ºC with predicted A_1 temperatures in the range of 755 to 791ºC for Santella [39] and 700 to 789ºC for the Alexandrov et al. revised [40] equations. The Ngwenya predictive equation (derived in the present study) regression line equation developed in the present study showed a positive linear relationship (R^2= 0.73) between the measured A_{c1} and predicted A_1 temperatures.

Peaks that were detected between 730 to 760ºC in the dilatometry curves of the weld samples during the heating cycle were due to changes in the material's state (Figures 4.5 to 4.10). Lun Wang reported these peaks in his research work as representing changes in ferromagnetic to paramagnetic and austenite transformation temperatures as shown in Figure 2.17 [40]. According to Lun Wang, the first peak represents changes in ferromagnetic to paramagnetic transformation (Curie temperature, A_2) and the second peak is the austenitization process itself. The austenitization process is represented by the start of austenite transformation (A_1) and the end of austenite transformation (A_3). Shrestha et al. also reported a peak at 741ºC in their study as an A_2 curie temperature indicating the changes in ferromagnetic to paramagnetic properties [24]. A change from a fast heating rate to a slow heating rate and inhomogeneity of the weld metal could have also contributed to this transition.

The measured A_{c3} temperatures in this study ranged from 863 to 919ºC and were closer to the Nitsche and Mayr [38] results under similar equilibrium conditions. Silwal et al. [41] reported an A_{c3} temperature of 925ºC in their research, closer to the maximum measured A_{c3} temperature in the present study. However, Nitsche and Mayr's [38] study simulated equilibrium conditions on the base metals. A regression line exhibited a positive linear relationship (R^2=0.64) between the measured A_{c3} temperature and the A_3 temperature derived from the predictive equation (Ngwenya equation) in the present study (Figure 4.11).

5.4 M_s temperatures

The measured M_s transformation temperatures of the weld metals were in the range of 378ºC to 471ºC with an average of 421ºC. The regression lines for predictive equations from previous studies [42] showed no linear relationship between the

predictive and measured M_s temperatures (Figures 4.13 to 4.15). However, the Ngwenya predictive equation derived in the present study showed a linear relationship (R^2 =0.69) between the predictive and measured M_s temperatures. The average M_s temperature value measured and predicted by the Ngwenya equation were similar. Nitsche and Mayr [38] in their study on the base metal under similar conditions (equilibrium) to the present study, found the M_s transformation temperatures to be between 362ºC to 427ºC, with an average of 385ºC. Research work by Alexandrov et al.[36] on P91 submerged arc weld (SAW) found the M_s temperature value (470ºC) close to the maximum value in the present study [36]. Silwal et al. found the M_s temperature of 394ºC on the grade P91 weld sample which is close to the minimum measured value in the present study [41].

5.5 Microstructural analyses

5.5.1 Base metal

In as-received and after post-weld heat treatment, the base metal exhibited a similar microstructure consisting of martensite and precipitates with the hardness of 228 HV. The precipitates were observed on and along the prior austenite grain boundaries as shown on the SEM micrograph in Figure 4.17 (b). This indicates that the base material was received in a normalized and tempered condition.

5.5.2 Weld metal

In as-welded and after post-weld heat treatment, the weld metal microstructures of most of the developed experimental electrodes consisted of martensite. However, a dark etching phase, delta/alpha ferrite and precipitates were also present in some of the developed experimental and commercial electrode weld metals (see section 4.6.2). The microstructures of the LAB 169 and LAB 172 samples showed ferrite after post weld heat treatment. The ferrite was not observed in their respective microstructures in the as-welded and dilatometry slow heating conditions. The presence of ferrite in the PWHT samples could be attributed to the slow heating rate during PWHT with the cooling curve passing either through the ferrite nose or inhomogeneity in microstructure, resulting in variation in chemical composition across the microstructure [37,45].

5.5.2.1 Formation of the dark etching phase

The dark etching phase was formed inside the prior austenite grain boundaries and along the martensite. This dark etching phase was reported by Lomozik et al. [52] in P91 steel during a second thermal cycle from stress relieving of the heat affected zone (HAZ) as secondary martensite (Figure 5.1). Figure 5.2 is the LAB 20 weld metal exhibiting a similar microstructure. According to these authors, during the first thermal cycle, primary martensite partially transforms into austenite in the critical region between A_{c1} and A_{c3}. During heating below the A_{c1} critical temperature in the second thermal cycle, retained austenite enriched with carbon and alloying elements will then transform to needle-shaped fine lath martensite (secondary) after cooling. Zhou et al. also reported the formation of secondary martensite (M′) from untransformed austenite with a schematic depiction of the morphology of this phase as illustrated in Figure 5.3 [53]. The secondary martensite laths formed were found to be refined, compared to the primary martensite. As expected, the Vickers hardness of the secondary martensite was harder at 479 HV as compared to the primary martensite with the hardness of 419 HV (see, Figure 4.32a). Based on the Vickers hardness and Zhou et al. study [53], the dark etching phase was concluded to be martensite.

Figure 5.1: Microstructure of P91 (a) simulated reheated coarse grain heat affected (SRCGHAZ) zone X5000 [52].

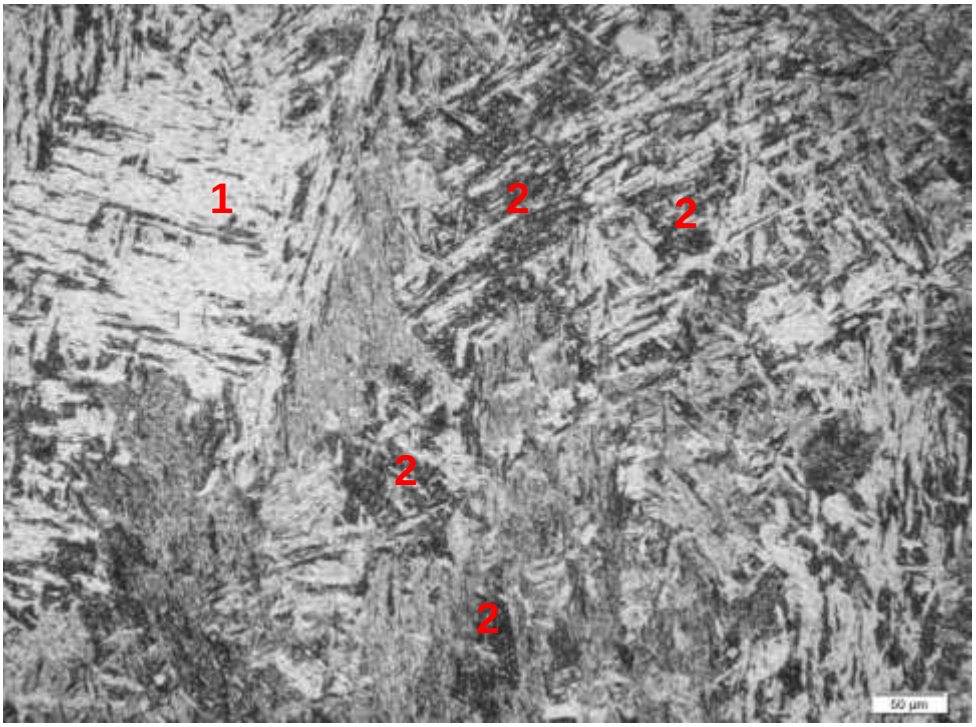

Figure 5.2: Microstructure of the LAB 20 electrode in the as-welded condition showing (1) primary martensite and (2) secondary martensite.

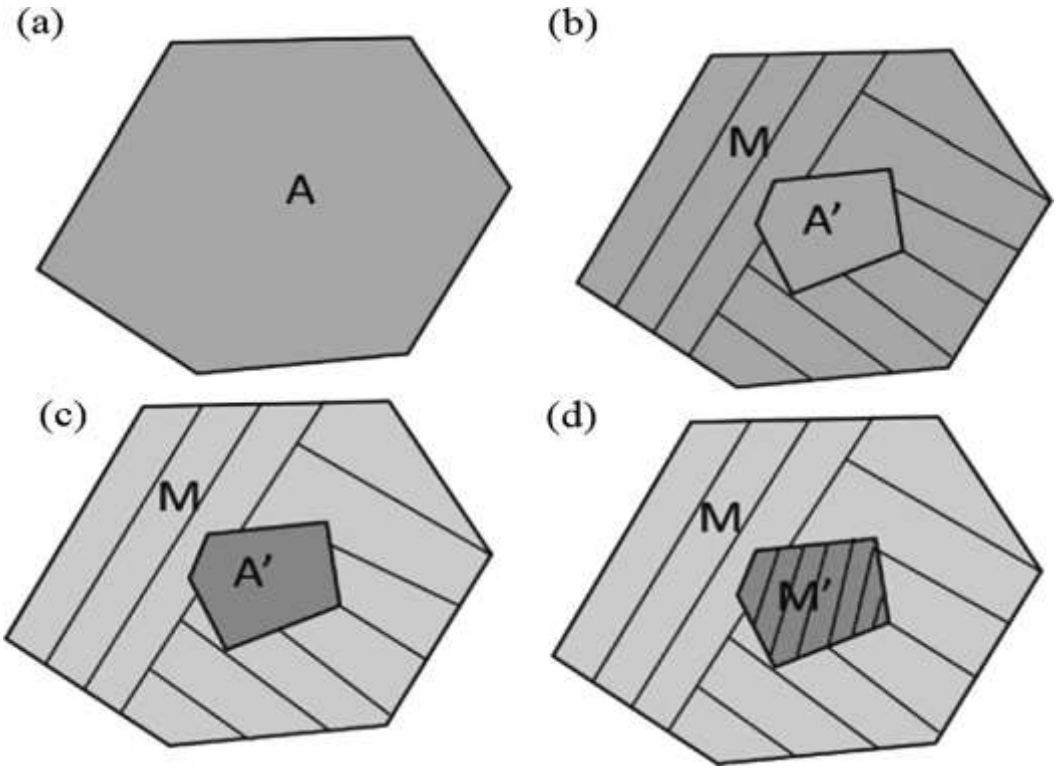

Figure 5.3: Microstructure evolution of 9Cr martensitic steel during quenching and partitioning treatment (a) austenization; (b) primary martensite formation; (c) carbon partitioning and (d) secondary martensite transformation. (A: prior austenite; A′: untransformed austenite; M: primary martensite; M′: secondary martensite) [53].

5.5.2.2 Formation of delta ferrite

Delta ferrite was observed in commercial 1 and commercial 2 electrodes in the as-welded and post-weld heat treatment conditions. In the as-welded condition, the delta ferrite was formed in selected areas of the martensitic matrix in the commercial 1 and commercial 2 microstructures (Figure 4.21). After post-weld heat treatment, the delta ferrite with a different morphology to the as-welded, was observed in the commercial 2 sample, forming islands along the martensite matrix (Figure 4.27).

Mayr in his study described how the delta ferrite phase that forms on the prior austenite grain boundaries in regions exposed to the peak temperature higher than 1200ºC restricts austenite grain growth [54]. Figure 4.29 is a SEM micrograph of the commercial 1 electrode in as-welded condition exhibiting the delta ferrite phase formed on the prior austenite grain boundary as reported above, surrounded by martensite laths. The delta ferrite phase had been formed during multi-run welding as a result of the previously deposited runs reaching peak temperatures in the delta ferrite plus austenite region ($\delta + \gamma$) above 1200ºC (Figure 5.4). The findings above were confirmed by the absence of delta ferrite on the last weld bead of the experimental and commercial electrode weld metals. Figure 5.5 is an optical micrograph of a ferritic heat resistant steel cooled from the δ-ferrite / γ-austenite region at 1ºC/s, exhibiting δ-ferrite (white) and α'-martensite (grey) phases [55]. A microstructure of δ-ferrite (white) and α'-martensite (grey) was also shown by an optical micrograph of the as-welded commercial 1 weld deposits prior to the final weld deposit (Figure 5.6).

No delta ferrite was detected after slow heating (28ºC/h) to the peak temperature of 1000ºC and fast cooling, in all the weld metals characterised. This indicates that the delta ferrite observed in as-welded commercial 1 and commercial 2 weld metals transformed completely to austenite during slow heating because the A_{c3} of these weld metals is below the peak temperature ($\delta + \gamma$ region). Since the PWHT temperature (760ºC) was below the A_{c1} critical temperatures of these weld metals, no transformation of the delta ferrite and martensite to austenite took place during the heat treatment. Based on the as-welded microstructure, after PWHT a duplex microstructure consisting of tempered martensite and δ-ferrite was expected in commercial 1 and commercial 2 weld metal. However, only the commercial 2 sample

had a duplex microstructure and the commercial 1 sample showed a fully martensitic microstructure. The reason for the inconsistent in the presence of δ-ferrite in commercial 1 and 2 could not be explained.

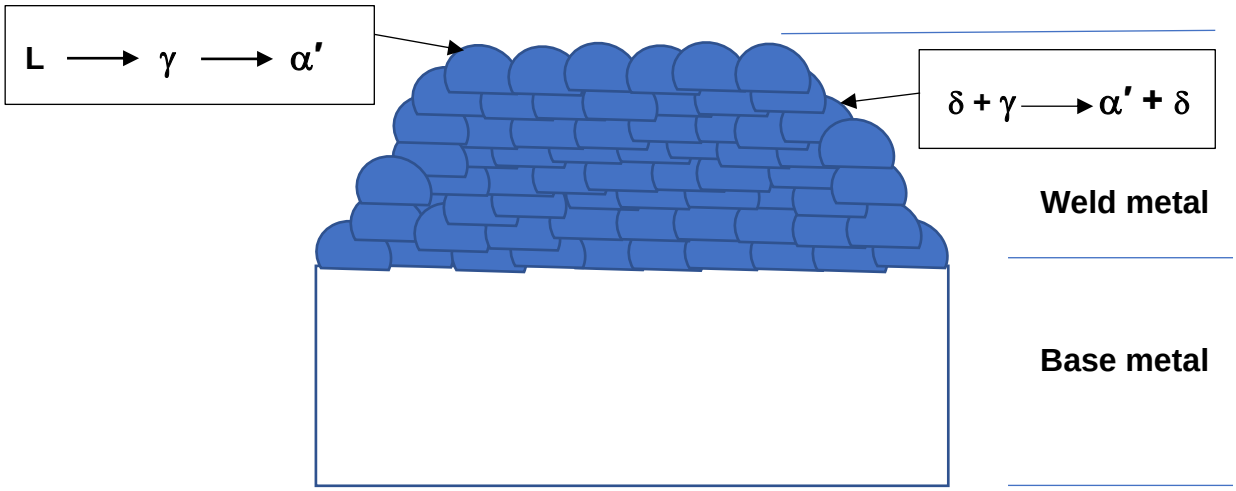

Figure 5.4: Schematic illustration of the effect of reheating of previously deposited weld run(s) and the final run during welding of P91 weld metal.

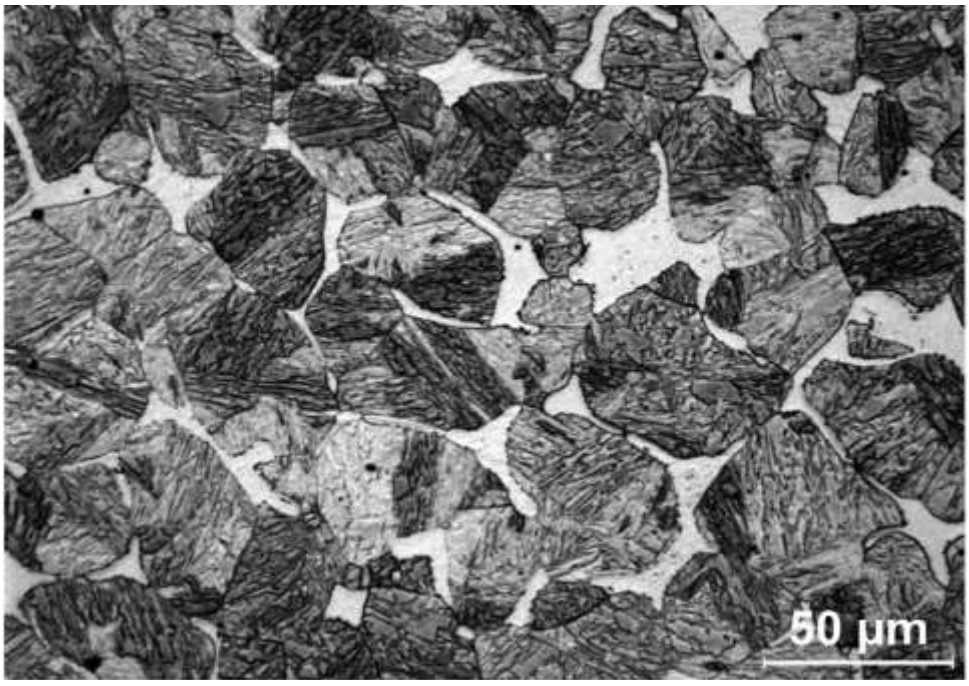

Figure 5.5: Optical microstructure of a ferritic heat resistant steel cooled from the inter-critical region (δ + γ) at 1ºC/s showing δ-ferrite (white) and martensite (grey) [55].

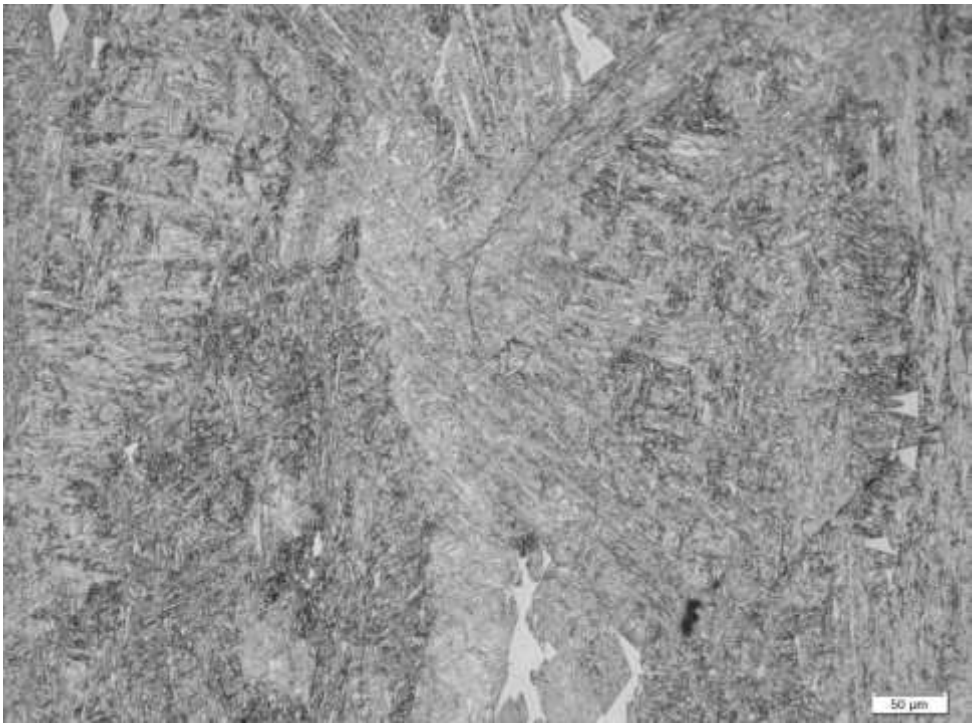

Figure 5.6: Optical micrograph of the commercial 1 sample in the as-welded condition, showing δ-ferrite (white) and martensite (grey) on the weld metal deposited prior to the final run (cooled from the inter-critical region).

5.5.2.3 Formation of alpha ferrite

Islands of the α-ferrite phase surrounded by tempered martensite were observed in LAB 169's microstructure after post-weld heat treatment. According to Peng et al. [45], the α-ferrite phase is formed when the following condition(s) are met:

- When the peak temperature exceeds the A_{c1} temperature during PWHT; and
- During slow cooling in the PWHT process, where the cooling curve could pass through the ferrite nose, the unstable austenite containing undissolved precipitates would transform to α-ferrite and not to martensite, even after the temperature reaches M_s (approximately 400ºC).

The dilatometry curve for the LAB 169 weld sample did not reveal any phase transformation during the post weld heat treatment process, indicating that the formation of the α-ferrite phase could be attributed to slow cooling (condition 2). This was supported by the measured A_{c1} and predicted A_1 temperatures above the post weld heat treatment temperature for the LAB 169 weld sample. The hardness profile

of this phase (Figure 4.34) ranged from 174 to 198 HV confirming it to be the ferrite phase.

5.5.2.4 Ferrite factor

A summarised evaluation of the microstructures based on Zhang et al. [31] (ferrite factor) and Merchant [43] (Cr_{eq} and ferrite factor) for the LAB 169, LAB 172, commercial 1 and commercial 2 samples are presented in Table 5.1. The A_{c1} temperatures of these weld metal samples are also shown in Table 5.1. Both the commercial 1 and commercial 2 weld metal samples had ferrite factors of 6.8 and 5.2 and Cr_{eq} of 11 and 10.2, meaning δ-ferrite retention was expected as observed in their respective microstructures. The ferrite factors of 7 and 8 were found in LAB 169 and LAB 172 samples respectively. Both the LAB 169 and LAB 172 compositions had a Cr_{eq} of 13.1 and 11.4 respectively for these electrodes. According to Zhang et al. [31] and Merchant [43] δ-ferrite retention was expected in the LAB 169 weld metal while a fully martensitic microstructure in LAB 172 was to be expected (Table 5.1). However, δ-ferrite was not observed in the as-welded LAB 169 microstructure indicating that this phase could have formed due to slow cooling during PWHT process [45].

Table 5.1: Predicted and final microstructures of samples with delta (δ) / (α) alpha ferrite.

Sample ID	Cr_{eq}	Ni_{eq}	FF	Measured A_{c1} (ºC)	Predicted microstructure	Final microstructure	
						As-welded	After PWHT at 760ºC
LAB 169	11.4	4.0	7.4	793	δ- ferrite retention expected in the microstructure as predicted by Zhang et al. and Merchant [1&2].	Martensite	Martensite & α-ferrite
LAB 172	13.1	4.7	8.4	771	A fully martensitic microstructure as predicted by Zhang et al and Merchant [1&2].	Martensite	Martensite & α-ferrite
Commercial 1	11.0	4.2	6.8	807	δ- ferrite retention expected in the microstructure as predicted by Zhang et al. and Merchant [1&2].	Martensite & δ-ferrite	Martensite
Commercial 2	10.2	5.0	5.2	784	A fully martensitic microstructure as predicted by Zhang et al [1]. δ- ferrite retention in the microstructure as predicted Merchant [2]	Martensite & δ-ferrite	Martensite & δ-ferrite

Note:

[1] Zhang et al. predict no delta (δ) ferrite retention in the microstructure when a ferrite factor is less than 6 percent [31].

2 Merchant predicts a fully martensitic microstructure when Cr_{eq} is greater 13 percent and Ni_{eq} less than 8 percent [43].

5.6 Effect of PWHT, carbon, and nitrogen on the Vickers hardness

Figure 2.18 shows a graphical illustration of the hardness response to post weld heat treatment for the P91 SMAW electrode weld metal [46]. After two hours of PWHT, a Vickers hardness of approximately 250 HV was obtained and compared to that of the experimental electrodes. Vickers hardness values below 190 HV were found in LAB 169 and commercial 2 weld metals after PWHT, verifying this phase as ferrite. As mention in literature [5, 31], the presence of α-ferrite or δ-ferrite phase is detrimental to the ductility and toughness of the weld metal.

The effect of carbon on the Vickers hardness is reported graphically in Figures 5.7. As shown on the graphs, a carbon increase correlates with an increase in Vickers hardness. Winchell et al [56]. reported graphically the effect of increasing the carbon content on the hardness of martensite and came to the same conclusion (Figure 5.7). An outlier (LAB 153) observed in Figure 5.5 had a fully martensitic microstructure. The reason for the hardness of 305HV could not be explained in this study. Figure 5.8 is a graphical representation of the effect of the sum of carbon + nitrogen on the Vickers hardness. An increase in C+N increases the Vickers hardness insignificantly as shown by the regression line slope (R^2=0.0439) in Figure 5.8.

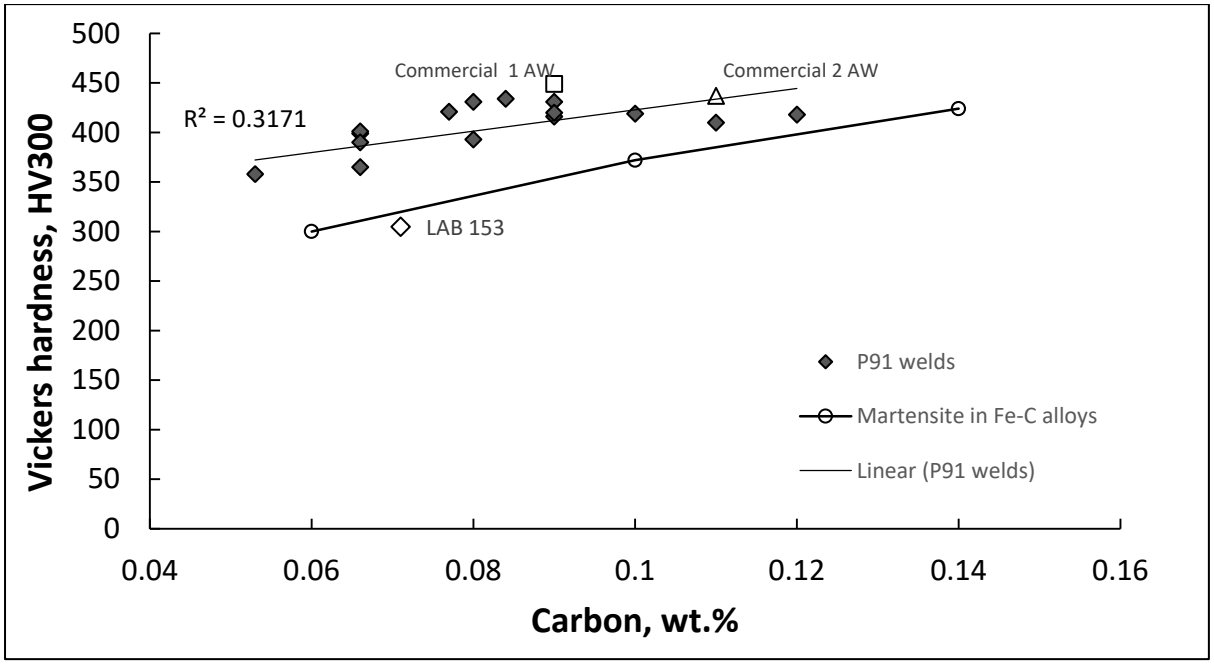

Figure 5.7: The effect of carbon on the hardness of the P91 weld metals and Fe-C alloys [56] martensite.

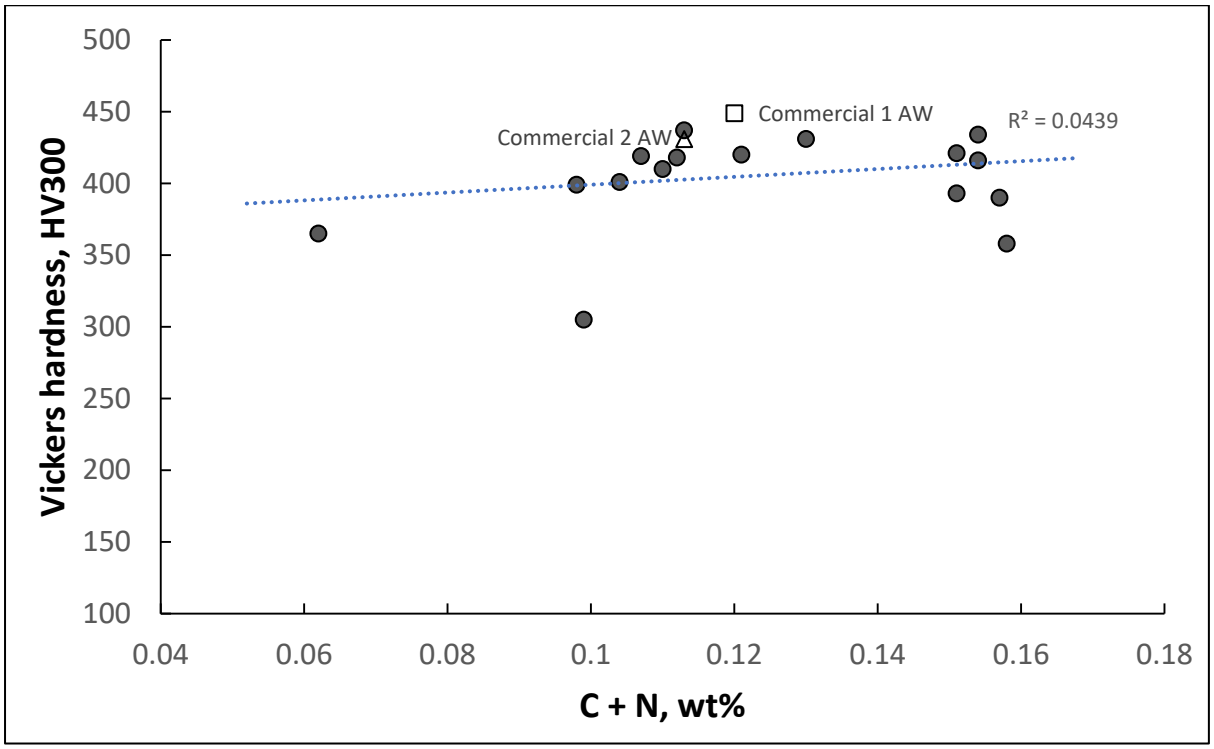

Figure 5.8: The effect of carbon + nitrogen contents on the Vickers hardness of the weld metal. Samples with delta ferrite are labelled on the graph. Dotted line interpolated between measured hardness and C + N.

CHAPTER 6: CONCLUSIONS

- Weldability of the SMAW developed experimental electrodes were comparable to that of the benchmark commercial electrodes. However, the commercial electrodes showed superior slag detachability and self-lifting characteristics. The LAB 24 electrode in phase 5 development was an outstanding experimental electrode with a good slag coverage and splitting slag which was easy to remove from the weld metal. This electrode also showed good metal transfer, low spatter volumes, low fumes, and moderate strike and re-strike characteristics.
- The SMAW laboratory experimental electrodes were developed according to the chemical composition requirements of the AWS A5.5 SFA: 9018-B9 specification. This was achieved in phase 5 development. However, the phosphorus content of the LAB developed experimental electrodes was invariably above that of the specification (0.018 to 0.034wt%).
- The lower critical temperatures (A_{c1}) of the laboratory experimental and commercial electrode's weld metal were above the PWHT temperature. However, some of the A_{c1} temperatures were below the 780°C target set for this study.
- The Santella equation [39] showed that there was a linear relationship between measured A_{c1} and predicted A_1 temperatures. No linear relationship was exhibited by Alexandrov et al's. revised equation [40] between the measured A_{c1} and predicted A_1 temperatures. Ngwenya's predicted A_1 temperature equation was developed in this study and showed a positive linear relationship (R^2=0.73) between the measured A_{c1} and predicted A_1 temperatures.

  $$\mathbf{A_1 = 847 - 341.1C - 54.8Si - 48.23Mn + 0.0424Cr - 78.5Ni + 25.94Mo + 120.24V - 12.51Nb + 155.56N}$$

  The predictive equation was based on 18 weld metals with the following range; 0.053-0.12wt% C, 0.19-0.42wt% Si, 0.42-0.83wt%Mn, 7.06-10.61wt% Cr, 0.058 - 0.74wt% Ni, 0.84-1.59wt% Mo, 0.11-0.36wt% V, 0.004-0.16wt% Nb, 0.003-0.068wt% N.

- The measured M_s temperatures of the weld metals in this study ranged from 369 to 471°C and were comparable to those of the Nitsche and Mayr [38] research work under similar equilibrium conditions. The predicted M_s temperatures

calculated from predictive equations from previous studies showed no linear relationship to the measured M_s temperatures in this study. Ngwenya's M_s temperature predictive equation developed in this study, showed a positive linear relationship (R^2=0.69) between the measured and predicted M_s temperatures.

M_s = 351.4 – 824.3C + 108.7Si + 83.7Mn + 5.88Cr + 290.1V + 67.1Ni - 44.4Mo -711.9N

- It has been shown in the present study that an increase in the sum of nickel and manganese have a strong effect in lowering the A_{c1} temperature. However, these two elements are not the only determining factor. Elements such as Cr, Mo, C, N, Si, Nb and V also have an influence on the A_{c1} temperature.
- The weld metal of the experimental laboratory electrodes and the commercial electrodes showed a microstructure which was predominantly martensitic (i.e. primary and /or secondary martensite) in the as-welded and after post weld heat treated conditions. However, δ-ferrite, α-ferrite and precipitates were observed in the as-welded and PWHT samples.
    - δ-ferrite was observed in the microstructures of commercial 1 and commercial 2 electrodes with the volume fraction as follows; 0.04 in commercial 1 (AW), 0.07 in commercial 2 (AW) and 0.09 in commercial 2 (PWHT).
    - α-ferrite was observed in the PWHT microstructures of LAB 169 and LAB 172 electrodes with the volume fraction of 0.19 and 0.14 respectively.
    - The ferrite factor is an inadequate predictor for the presence of ferrite.
- The as-welded Vickers hardness of developed experimental electrodes was in the range of 305 to 431 HV. The hardness was significantly reduced to between 211 to 263 HV after PWHT and comparable to that of the base metal and the commercial electrodes.

7. RECOMMENDATIONS FOR FUTURE WORK

- The recovery of the metal from the flux coating to the weld metal of the developed experimental electrodes may be characterised by analytical techniques (such as energy dispersive X-ray spectrometry, inductively coupled plasma, optical emission spectrometer, and atomic absorption). This will give a better understanding of the metal transfer from the flux to weld metal and metal losses to the slag.
- TEM analyses of these developed experimental electrode's weld metal for better characterisation of this material (i.e. secondary martensite, δ and α ferrite and precipitates).
- The effect of δ and α ferrite on the impact toughness of the developed experimental electrodes may be investigated.
- The effect of high phosphorus content on the mechanical properties (impact toughness) of the developed experimental electrodes may be investigated.
- The P91 welds are susceptible to cold cracking of brittle martensite phase during cooling after welding. The susceptibility of the developed experimental electrodes weld metals to cold cracking may be investigated.

8. REFERENCES

[1] Ennis P.J. and Czyrska-Filemonowicz A., *Recent advances in creep-resistant steels for power plant application*, sadhana-Academy Proceeding in Engineering Science, Vol. 28, Parts 3 & 4, 2003, p. 709-730

[2] Das C.R., Albert S.K., Laha K., Swaminathan J., Ravi S., Bhaduri A.K., Murty B.S., and Mayr P., *Influence of coincidence site lattice boundary on creep resistance P91 steel weldment, Science direct*, Procedia engineering 86, 2014, p. 80-87.

[3] Bhadeshia H.K.D.H., *Design of creep resistant welding alloys*, University of Cambridge, United Kingdom, p.795-803.

[4] Hilkes J. and Gross V., *Welding CrMo steels for power generation and petrochemical applications*, Biuletyn Instytutu Spawalnictwa, no. 2, 2013, p.11-22.

[5] Bush D.R., *An introduction to the 9Cr-1Mo-V Alloys*, Valve magazine, Winter, 2001, p.3 – 8.

[6] Messler R.W. Jr, *Principles of welding processes, Physics, Chemistry and Metallurgy*: WILEY-VCH Verlag GmbH & Co. KGaA, 2004.

[7] Lecture notes:2013, Topic: *Welding processes NWP 700*, Department of Materials Science and Metallurgical Engineering, University of Pretoria, South Africa.

[8] Prof. Dr.-Ing. U. Dilthe, Lecture notes, Topic: *Welding technology 1 (Welding and cutting technologies)*, Welding Institute, Aachen University

[9] Brown A., Lecture notes, Topic: *Electrode manufacturing techniques*, BOC Murex, Welding Research and Development laboratories.

[10] Lancaster J.F., *Welding Metallurgy*, six editions: Abington Publishing, 1999.

[11] Kin-Ling S., *Flux system design and optimization of shielded metal arc welding for high nickel*, M.S. thesis, Colorado School of Mines, Colorado, 2009.

[12] Ferrera K.P., *Investigation of MnO, SiO_2, and CaO as a welding flux*, M.S. thesis, School of Mines, Colorado, 1974.

[13] Olson D.L., Liu S., Frost R.H., Edwards G.R. and Fleming D.A., *Nature and behaviour of fluxes used for welding*, ASM Metal Handbook, Volume 6, 1993.

[14] Sham K. and Liu S., *Flux-coated development for SMAW consumable electrode of high-nickel alloys*, Welding Journal, August 2014, p. 271-281.

[15] Ngwenya P., *Investigation of low impact values in low hydrogen-controlled electrodes*, Afrox Internal document, 2007.

[16] Linnert G.E., *Fluxes, slags and gases for shielding," in Welding metallurgy*, third edition, volume 1, New York (USA): American Welding Society, 1965, p.367-407.

[17] Easterling K., *Fusion and process variables, in Introduction to Physical Metallurgy of Welding,* second edition: Butterworth, 1992, p.1-47

[18] Sithole D. and Ngwenya P., *Process Flow diagram for Low electrode manufacturing*, Afrox Internal document, 2008.

[19] Dieter G.E., *Creep and stress rupture, in Mechanical Metallurgy*, third edition, United Kingdom: McGraw-Hill Book Company Limited, 1988, p.432-470.

[20] Francis J.A., Mazur W. and Bhadeshia H.K.D.H., *Type IV cracking in ferritic power plant steels*, Material Science and Technology, Vol. no. 22, 2006, p.1387-1395.

[21] Viswanathan R. and Bakker W.T., *Material for ultra-supercritical fossil power plants*, Electric Power Research Institute (EPRI), California, Technical report no. 114750, March 2000.

[22] ABE F., *Strengthening mechanisms in steel for creep and creep rupture*, National Institute for Materials Science (NIMS), Japan, 2008, p. 279-301

[23] Maruyama K., Sawada K. and Koike J., *Strengthening mechanism of creep tempered martensitic steel*, ISIJ International, vol. 41, No. 6, 2001, p.641-653.

[24] Shrestha T., Alsagabi S.F., Charit I., Potirninche G.P. and Glazoff M.V., *Effect of heat treatment on microstructure and hardness of grade 91 stee*l, Metals, vol. 5, 2015, p.131-149.

[25] Zheng-Fei Hu, *Microstructure evolution and life assessment in power plants*, in Heat-resistance steels, School of Materials Science and Engineering, Tongji University, Shangai, China, 2012.

[26] Abe F., *Precipitate design for creep strengthening of 9%Cr tempered martensitic steel for ultra-supercritical power plants*, Science and technology of advanced materials 9, 2008, p.1-15

[27] Basirat M., Shrestha T., Barannyk L.L., Potirninche G.P and Charit I., *A study of creep damage model for high-temperature deformation and failure of modified 9Cr-Mo steel weldments*, Metals, 2015, 5, p.1487-1506.

[28] Shrestha T., Basirat M., Charit I., Potirninche G.P. and Rink K.K., *Creep rupture behaviour of grade 91 steel*, Material Science & Engineering, A 669, 2016, p. 75-86.

[29] Golanski G. and Kepa J., *The effect of ageing temperature on the microstructure and mechanical properties of GX12CrMoVNbN9-1 (GP 91) cast stee*l, Archives of metallurgy and material, vol. 57, Issue 2, 2012, p.576-582.

[30] Jablonski P., Alman D., Dogan O., Holcomb G. and Cowen C., *9Cr-1Mo steel material for high temperature application*, U.S. Patent 8,317,944 B1, 27 Nov.,2012.

[31] Zhang Z., Farrar J.C.M., and Barnes A.M, *Weld Metals for P91*, Metrode products limited, p. 1-18.

[32] ASME Boiler and Pressure Vessel Code: ASME II-part A: 2010. *Ferrous material specifications*. USA, New York: ASME international, 2010.

[33] Tamura M., Kumagai T., Miura N., Kondo Y., Shinozuka K., and Esaka H., *Effect of martensitizing temperature on creep strength of modified 9Cr steel*, Material Transaction, vol. 52, No. 4, 2011, p. 691-698.

[34] Alexandrov B.T. and Lippold J.C., *Method and devise for investigating phase transformation in metals and alloys*, US Patent no. 7,909,505, 2011 and 7,473028, 2009.

[35] ASTM international standard: ASTM A1033-04:2004. *Standard practice for quantitative measurement and reporting of hypoeutectoid carbon and low-alloy steel phase transformations*, ASTM international, March 2004.

[36] Alexandrov B., Wang L., Siefert J., Tatman J., and Lippold J., *Phase transformation in creep strength enhance ferritic steel welds*, Scientific proceedings VIII international congress, Technologies, Materials, vol. 2, 2011, p.13-16.

[37] Santella M.L., Swindeman, R.W., Reed R.W., and Tanzosh J.M., *Martensite formation in 9Cr-1Mo steel weld metal and its effect on creep behaviour*, USA, Office of the Fossil Energy, Advance research material program.

[38] Nitsche A. and Mayr A., "*Round robin test on measurement of phase transformation in 9Cr-1Mo Steel*, International Institute of Welding, 2016.

[39] Santella M.L., *Influence of chemical compositions on lower ferrite-austenite transformation temperature in 9%Cr steels*, Journal of Pressure Vessel Technology, vol. 134, April 2012.

[40] Lung Wang B.S., *Development of predictive formulae for the A_1 temperature creep strength enhanced ferritic steels*, M.S. thesis, Ohio State University, 2010.

[41] Silwal B., LI L., Deceuster A. and Griffiths B., *Effect of PWHT on the toughness of heat-affected zone for grade 91 steel*, Welding Journal, vol. 92, March 2013, p.80 – 86.

[42] Cheng L., Zhenbo Z., Derek O.N. and Yunxu L., *A new empirical formula for the calculation M_s temperatures in pure iron and super-low carbon alloys steels*, Journal of material processing technology, vol. 113, 2001, p. 556-562.

[43] Merchant S.Y., *A review of effect of welding and post weld heat treatment on microstructure and mechanical properties of grade 91 Steel*, International journal of research in engineering and technology, vol. 4, 2015 p.574-580.

[44] Rossini N.S., Dassistia N., Benyounis Y.K. and Olabi A.G., *Methods of measuring residual stresses in components*, Elsevier, Metarials & Design, 35, 2012, p.572-588.

[45] Peng N.P., Ahmad B., Muhamad M.R. and Ahandlin M., *Phase transformation of P91 steels upon cooling after short term overheating above A_{c1} and A_{c3} temperatures*, Advance material research, Trans Tech publication, 2013.

[46] Dr. Herbert Heuser, Welding of P91, Bohler Welding Group, 2011.

[47] ASME Boiler and Pressure Vessel Code: ASME II-part C SFA-5.5, 2010. *Specification for Low-Alloy Steel Electrodes for Shielding Metal Arc Welding*, ASME international, 2010.

[48] Afrox procurement standard: Raw materials and suppliers procurement standard, Afrox internal document.

[49] Davies A.C., *The science and practice of welding*, tenth edition, vol. 2: United Kingdom, The Press Syndicate of University of Cambridge, 1993, p.7.

[50] Vander Voort G.F., *Metallography principles and practice*, New York: McGraw-Hill series, 1994.

[51] Underwood E., *Quantitative Stereology*, Massachusetts: Addison-Wesley Publishing Company, 1970, p1-18.

[52] Lomozik M. and Zielinska-Lipiec A., *Microscopic analysis of the Influence of multiple thermal cycles on simulated HAZ toughness of P91 steel*, Archive of Metallurgy and Materials, vol. 53 (2008) – p. 1026 - 1034

[53] Zhou X., Liu C., Yu L, Liu Y., and Li H., *Phase transformation behavior and microstructural control of high-Cr martensitic / ferritic heat-resistant steels for power and nuclear plants*, Journal of materials science & technology 31, 2015, p. 235-242.

[54] Mayr P., *Evolution of microstructure and mechanical properties of heat affected zone in B-Containing 9% chromium stee*l, D.S thesis, Graz University of Technology, Austria, 2007.

[55] Xiaosheng Z., Yongchang L., Zhixia Q., Qianying G., Chenxi L., Liming Yu and Huijun Li, *Effects of cooling rates on δ-ferrite/γ-austenite formation and martensitic transformation in modified heat resistant steel*, Fusing Engineering and Design 125, 2017, p. 354-360.

[56] Winchell and Cohen, *The effect of carbon on the hardness of martensite and austenite*, Trans. Met. Soc. AIME 224, 1962, p638.

Appendix A: Weldability report

Table A1: Weldability evaluation report for laboratory developed and commercial electrodes

Electrode identification	Electrode strike & re-striking	Arc stability	Metal transfer	Spatter volume	Wetting action	Metal flow	Weld pool explosion	Bead appearance	Slag flow /coverage /removal	Welding fumes	Welding defects	Electrode overheating
Phase 1												
LAB 74	3	3	3	2	3	3	3	3	1	3	3	3
LAB 75	3	4	4	3	4	4	4	3	3	3	4	3
LAB 76	3	3	3	3	3	3	3	3	2	3	4	3
LAB 77	3	3	3	3	3	3	3	3	2	3	4	3
LAB 78	3	3	3	3	3	3	3	3	2	3	4	3
LAB 79	3	3	3	3	3	3	3	3	2	3	4	3
Phase 2												
LAB 99	3	3	3	3	4	4	4	3	3	3	4	3
LAB 100	3	3	3	3	4	4	4	3	3	3	4	3
LAB101	3	3	3	3	4	4	4	3	3	3	4	3
LAB102	3	3	3	3	4	4	4	3	3	3	4	3
LAB103	3	3	3	3	3	3	3	2	2	3	3	3
LAB104	3	3	3	3	3	3	3	2	2	3	3	3
Phase 3												
LAB 150	3	3	3	3	4	4	4	3	3	3	4	3
LAB 151	3	3	3	3	4	4	4	3	3	3	4	3
LAB 152	3	3	3	3	4	4	4	3	1	3	4	3
LAB 153	3	3	3	3	4	4	4	3	2	3	4	3
LAB 154	3	3	3	3	4	4	4	3	2	3	3	3
LAB 155	3	3	3	3	4	4	4	3	2	3	3	3

Table A1: Continued

Electrode identification	Electrode strike & re-striking	Arc stability	Metal transfer	Spatter volume	Wetting action	Metal flow	Weld pool explosion	Bead appearance	Slag flow /coverage /removal	Welding fumes	Welding defects	Electrode overheating
Phase 4												
LAB 168	3	3	3	3	4	4	3	3	3	3	3	3
LAB 169	3	4	4	3	4	4	3	3	2	3	4	3
LAB 170	3	3	3	2	3	4	2	3	2	3	3	3
LAB 171	3	3	3	3	4	4	3	3	3	3	4	3
LAB 172	3	3	3	3	3	3	3	3	2	3	3	3
LAB 173	3	3	3	3	3	3	3	3	2	3	3	3
Phase 5												
LAB 19	3	3	3	3	4	4	4	3	3	3	4	3
LAB 20	3	3	3	3	4	4	4	3	3	3	4	3
LAB 21	3	3	3	3	4	4	4	3	3	3	4	3
LAB 22	3	3	3	3	4	4	4	3	3	3	4	3
LAB 23	3	3	3	3	3	3	3	3	3	3	4	3
LAB 24	3	4	4	4	4	4	4	4	3	4	4	4
Commercial 1	4	4	4	4	4	4	4	4	5	3	4	4
Commercial 2	4	4	4	4	4	4	4	4	5	3	4	4
Commercial 3	4	4	4	4	4	4	4	4	5	3	4	4

Appendix B: Chemical composition

Table B1: Chemical composition of the laboratory developed electrodes, commercial electrodes, and P91 header material.

Element (wt.%)	C	Si	Mn	P	S	Cr	Ni	Mo	Al	Cu	V	Nb	N
AWS SFA 5.5 E9018-B9	**0.08-0.13**	**0.30**	**1.20**	**0.01**	**0.01**	**8.0-10.5**	**0.80**	**0.85-1.20**	**0.04**	**0.25**	**0.15-0.30**	**0.02-0.10**	**0.02-0.07**
Phase 1													
LAB 74	0,059	0,358	0,60	0,031	0,0062	7,57	0,71	0,97	0,0071	0,021	0,19	0,01	0,003
LAB 75	0,07	0,351	0,63	0,027	0,0062	7,45	0,70	0,98	0,0032	0,021	0,12	0,01	0,04
LAB 76	0,066	0,358	0,58	0,029	0,0062	7,29	0,70	0,98	0,0032	0,021	0,12	0,004	0,04
LAB 77	0,059	0,358	0,60	0,031	0,0062	7,57	0,71	0,97	0,0033	0,021	0,12	0,01	0,04
LAB 78	0,06	0,361	0,61	0,028	0,0058	7,25	0,71	1,14	0,0032	0,021	0,11	0,01	0,04
LAB 79	0,069	0,391	0,65	0,028	0,0056	7,49	0,74	1,12	0,0035	0,022	0,13	0,01	0,04
Phase 2													
LAB 99	0,11	0,31	0,64	0,03	0,011	7.64	0,65	1,16	0,000	0,020	0,35	0,08	0,05
LAB 100	0,11	0,35	0,67	0,031	0,011	7,91	0,66	1,13	0,000	0,020	0,35	0,10	0,05
LAB 101	0,10	0,33	0,62	0,032	0,011	7,82	0,63	1,07	0,000	0,020	0,35	0,12	0,05
LAB 102	0,10	0,35	0,68	0,03	0,011	7,91	0,64	1,14	0,000	0,020	0,35	0,13	0,05
LAB 103	0,10	0,34	0,63	0,034	0,011	7,73	0,64	1,08	0,000	0,020	0,35	0,16	0,05
LAB 104	0,10	0,33	0,59	0,033	0,011	7,7	0,64	1,07	0,000	0,020	0,36	0,15	0,05
Phase 3													
LAB 150	0,066	0,35	0,60	0,02	0,010	7,2	0,61	1,02	0,0018	0,017	0,18	<0,004	0,05
LAB 151	0,07	0,41	0,60	0,019	0,010	7,72	0,6	0,99	0,0023	0,018	0,17	<0,004	0,06
LAB 152	0,069	0,38	0,59	0,018	0,010	7,6	0,61	0,99	0,0022	0,015	0,18	<0,004	0,05
LAB 153	0,071	0,40	0,61	0,02	0,010	7,94	0,59	0,99	0,0023	0.016	0,17	<0,004	0,05
LAB 154	0,066	0,40	0,58	0,021	0,010	8,55	0,59	1,09	0,0019	0,015	0,18	<0,004	0,05
LAB 155	0,066	0,42	0,59	0,019	0,010	8,21	0,58	1,00	0,0022	0,015	0,18	<0,004	0,05

Table B1: Continued

Element (wt.%)	C	Si	Mn	P	S	Cr	Ni	Mo	Al	Cu	V	Nb	N
Phase 4													
LAB 168	0,062	0,25	0,49	0,025	0,01	8,83	0,69	0,88	0,006	0,020	0,14	0,018	0,049
LAB 169	0,053	0,21	0,42	0,023	0,01	9,22	0,63	0,86	0,006	0,020	0,13	0,01	0,052
LAB 170	0,072	0.23	0,47	0,027	0,01	9,6	0,66	0,85	0,006	0,020	0,14	0,017	0,05
LAB 171	0,084	0,22	0,48	0,028	0,01	10,38	0,67	0,87	0,006	0,020	0,13	0,018	0,053
LAB 172	0,077	0,19	0,42	0,026	0,01	10,61	0,69	0,9	0,006	0,020	0,15	0,011	0,059
LAB 173	0,078	0,22	0,45	0,026	0,01	10,12	0,62	0,84	0,006	0,020	0,13	0,013	0,049
Phase 5													
LAB 19	0,09	0,22	0,57	0,019	0,01	8,62	0,64	0,87	0,005	0,030	0,16	0,08	0,068
LAB 20	0,08	0,25	0,50	0,027	0,018	9,67	0,61	0,91	0,005	0,030	0,16	0,09	0,068
LAB 21	0,08	0,21	0,54	0,023	0,014	8,99	0,59	0,86	0,005	0,030	0,17	0,08	0,068
LAB 22	0,09	0,25	0,55	0,020	0,013	8,33	0,52	1,59	0,007	0,030	0,14	0,09	0,065
LAB 23	0,09	0,27	0,56	0,025	0,011	8,33	0,57	0,82	0,005	0,030	0,14	0,09	0,066
LAB 24	0,09	0,31	0,58	0,023	0,011	8,62	0,58	0,85	0,005	0,030	0,15	0,1	0,066
Commercial 1	0,093	0,26	0,83	0,010	0,005	7,82	0,058	1.07	0,0094	0,015	0,19	0,059	>0,036
Commercial 2	0,106	0,21	0,66	0,014	0,003	7,06	0,61	0,99	0,0087	0,015	0,24	0,059	>0,036
Commercial 3	0,124	0,18	0,58	0,010	0,006	8,04	0,70	1,05	0,0095	0,020	0,18	0,041	>0,036
ASME SA335 P91	**0,08-0,12**	**0,30-0,60**	**0,20-0,50**	**0.01**	**0,02**	**8,0-9,5**	**0,40**	**0,85-1,05**	**0,02**	**-**	**0,18-0,25**	**0,06-0,10**	**0,03-0,07**
Base material	0,11	0,32	0,45	0,014	0,0010	8,60	0,21	0,94	0,010	0,092	0,21	0,08	0,051